U.PORTO
FEUP FACULDADE DE ENGENHARIA
UNIVERSIDADE DO PORTO

Mechanical Design and Structural Analysis of a Deployable Synthetic Aperture Radar Antenna for In-Orbit Demonstration

Nuno Alexandre Moura Costa

Thesis submitted to Universidade do Porto – Faculdade de Engenharia
in partial fulfillment of the requirements for the degree of
Master in Mechanical Engineering

Supervisors

Hamed Akhavan (FEUP)

Diogo Monteiro (Tekever)

Mestrado Integrado em Engenharia Mecânica (MIEM)
Departamento de Engenharia Mecânica (DEMec)
Faculdade de Engenharia (FEUP)
Universidade do Porto (UP)

Abstract

In the context of a master thesis in the specialization of aeronautical structures, a concept of a deployable mechanism for the opening of SAR (synthetic aperture radar) antennae panels was designed and studied. The design of such a mechanism was encouraged by a Portuguese Aerospace company named Tekever searching to develop the Portuguese space sector. The work performed during the applicant's time at the company is thus described in this document. In the first stage, an introduction to SAR technology and the space sector is presented, followed by an extensive literature review on topics that were relevant to the project. First, the main characteristics of the low-earth-orbit environment are explored along with its impact on the structure. Following this point, a thorough review of mechanisms used for deployment is also presented. Finally, the theoretical background, needed to understand the finite element analysis that was performed, plus an exposition of the flight load environment to the structure is discussed. Following the literature review, a preliminary design of two proposed mechanisms was conceived. All the main characteristics and insights behind the two are explained, to then follow the choice of one of them. The described characteristics include materials used, method of deployment, method of stowage, synchronization principle, and main elements. In the end, some design iterations were performed and for this, static, sine sweep, and random analysis were continuously performed until achieving a satisfactory design. The margins of safety were then calculated to show the ability of the structural mechanism to sustain loads. To finish, some conclusions were drawn explaining the key findings of the investigation and future works still to be done in order to improve the design.

Resumo

No âmbito desta tese de mestrado da especialidade de estruturas aeronáuticas, foi projetado e estudado o conceito de um mecanismo de abertura de painéis de antenas SAR (radar de abertura sintética). A conceção de tal mecanismo foi incentivada pela empresa aeroespacial portuguesa Tekever, que procura desenvolver o sector espacial português. O trabalho realizado durante o período em que o candidato esteve na empresa é assim descrito neste documento. Numa primeira fase, é apresentada uma introdução à tecnologia SAR e ao sector espacial, seguida de uma extensa revisão bibliográfica sobre tópicos relevantes para o projeto. Para começar, são exploradas as principais características do ambiente da órbita terrestre baixa e o seu impacto na estrutura. A seguir, é também apresentada uma revisão exaustiva dos mecanismos utilizados na indústria. Finalmente, são discutidos os antecedentes teóricos necessários para compreender as análises de elementos finitos efectuadas, bem como uma exposição do ambiente de carga durante o voo que afeta a estrutura. Após a revisão bibliográfica, foi concebido um desenho preliminar de dois mecanismos propostos. São explicadas todas as principais características e ideias subjacentes aos dois mecanismos, para depois se proceder à escolha de um deles. As características descritas incluem os materiais utilizados, o método de acionamento, o método de arrumação, o princípio de sincronização e os seus principais elementos. No final, foram efectuadas algumas iterações de conceção e, para tal, foram realizadas continuamente análises estáticas, de sine sweep e random até se obter um configuração satisfatória. As margens de segurança foram então calculadas para mostrar a capacidade do mecanismo suportar as cargas. Para finalizar, foram tiradas algumas conclusões que explicam os principais resultados da investigação e os trabalhos futuros ainda por fazer para melhorar o projeto.

Acknowledgements

This work would not be possible without the help of very important people from my close circle, from the university, and from the company.

First I would like to acknowledge my family, especially my parents and my friends and girlfriend for the unconditional support that was always present throughout these past months and for the care and patience that had towards me.

Secondly, I want to thank Tekever and all the great people there, for the opportunity of being in such an interesting and challenging field, for all the lessons learned, for giving me all the tools I needed to perform this work, and for the great environment created at the office which made this whole process a lot easier.

From the company's side, I would like to highlight the good welcome, the help, the care, and the knowledge transmitted throughout the time there from Marta Silva of the HR team, professor Sérgio Reis Cunha, and from the mechanical team, João Silva, Diogo Morgado and last but most importantly Diogo Monteiro, my company's supervisor who's help and support made this become reality.

Finally, I cannot forget the incredible support throughout this whole time from Hamed Ackhavan, my main supervisor from the university who was always ready to help and give the best of advice, making the experience much easier.

Contents

List of Figures

List of Figures

List of Tables

Abbreviations

AA	Aluminum Alloy
ATOX	Atomic Oxygen
CFRP	Carbon Fiber Reinforced polymers
CCL	Close Cable Loop
COG	Center of gravity
DUL	Design yield load
DYL	Design yield load
DOF	Degree of Freedom
FEA	Finite Element Analysis
FR	Frequency response
ISS	International Space Station
LEO	Low Earth Orbit
LV	Launch Vehicle
PSD	Power Spectral Density
QS/QSL	Quasi-static/Loads
RBM	Rigid Body Mode
SAR	Synthetic Aperture Radar
SC	Spacecraft
STEM	Storable tubular deployable members
UAV	Unmanned Aerial Vehicle
UV	Ultraviolet

Chapter 1

Introduction

The project of building a mechanism for space application, capable of opening such sensible parts as a synthetic aperture radar is indeed a challenging task. A lot of considerations must be present and a whole set of problems has to be tackled. The space environment makes the job more challenging, its harsh conditions and the rocket loads are very hard on structures. Therefore the job of the mechanical design engineer in this field must be coupled with experience and expertise in a variety of subjects to minimize as much as possible the probability of failure of a component. The same task is thus present in this work, which will try to cover the main steps of the design process.

The project and its steps are described in further chapters but prior to that, it is important to understand the background behind this work, the motivation that lead the company to bet and work on such a project, the space sector and its growth and impact on the technological development of the country and the world in general, the radar technology and finally, the objectives and methodologies of the work performed.

1.1 Motivation

The motivations for this work involve two parts, one is the company's side the other a personal side. The former strives/is interested in demonstrating its synthetic aperture radar (SAR) technology in space environment. Tekever has a long SAR flight heritage aboard their UAVs granting them experience in the field, an experience which leads to improvements in their technology, that now they want to take to space. With this feat, the company will gain further insights into the implications that come with the technology's use in orbit and also gain space heritage, which could benefit them in the future. Therefore, an in-orbit demonstrator is a

perfect project to gain knowledge in this field and get actual experience for future developments. From a personal perspective, it was an honor to be part of such a project with the potential of helping the Portuguese industry to be more present in such a technological, prestigious, and advanced sector. Besides, the contact gained with the industry's environment helped the applicant to better understand the space sector, and be part of a motivated, curious, and talented team of engineers.

1.2 The space sector

The space sector is a growing part of the world's economy, being worth around 500 billion dollars [1]. Space exploration started in the last century with the two main competitors being the USA and Russia, but has now turned into a global pursuit. Its impact on the world is often overlooked, the observation satellites launched into orbit give insights into matters like global warming, food production worldwide and how it is being impacted by droughts and insect invasions, and national security while communications satellites are a basis of everyone's lives and fuel today's rapid economy [2].

A change in investment sources is taking place in the sector. Although public investment is still a major part of the sector's capital sources, private companies are gaining interest and investing more than ever before. This change which topped 10 billion dollars in investment, is motivated by the decreasing cost of space activities. It is this decrease in prices and increases in opportunities that led many countries to bet on the sector [2]. Advancements in materials science and 3D printing have significantly decreased launch costs impacting the industry and allowing more parts to be present in the sector. Small satellites are increasing in popularity to save on launch costs, while still providing competitive features due to advances in material science and technology. New companies like SpaceX, OneWeb, Telesat Canada, Samsung, and Boeing are taking a shot at small satellite constellations [3]

The Portuguese presence in space is less than two decades old and started when it joined the European Space Agency (ESA). It is from 2012 that it gains more pace, particularly in the telecommunications industry. Space economy potential growth is enormous and it would be a great opportunity for the country's growth and development. Possible businesses could come from agriculture and surveillance of crops from space, territory monitoring, and defense recognition [4].

Tekever, which had placed itself as a big name in the UAV industry, decided to invest in the space sector and is now growing in the medium. Its presence in projects of the ESA marks its involvement in the area, having taken part in the development of critical software and hardware in missions like HERA and Proba-3.

The company was also present and took the lead in some Portuguese consortiums, to highlight the Infante project reaching the TRL-8 stage of development (one prior to launch).

1.3 Synthetic aperture radar

Synthetic aperture radar, as the name indicates is a technology that enables a smaller aperture radar to have the same resolution as a big aperture one by creating a bigger aperture synthetically by moving through space. It has a variety of applications among which are environmental monitoring, planetary science, and navigation [5]. SAR antennas are usually made from planar microwave radiators with slotted waveguides included [6].

Radar technology proved its value as a defensive tool in world war II detecting enemies in all weather conditions and in the cold war enabled surveillance of enemy's actions, so it was thought to be the game changer in reconnaissance. It had an issue though, an antenna of the size of a football field would be needed for the kind of resolution intended. In 1951, Carl Wiley developed a method, based on the Doppler effect or a speed shift between the reflected signal relative to the antenna that enabled detection with 1/100th of the needed surface and so, the SAR was born. The technology continued to develop, continuously increasing resolution [7]. In June 1978, the first civilian application of the technology, the Seasat was launched for studying the earth which can be seen in Figure 1.1. Prior to it, image acquisition was made through the capturing of visible light with much less resolution [8].

Figure 1.1: Seasat satellite - first SAR civil use. Taken from [9]

Synthetic Aperture Radar (SAR) sets itself apart from regular radars due to its ability to create high-resolution images of the Earth's surface by combining data from different positions. The movement of the radar through space effectively creates a larger antenna aperture virtually, a synthetic aperture. By measuring the timing and strength of radio wave echoes reflected from the ground and objects, SAR systems collect data while moving, which is processed to generate detailed images that reveal terrain, vegetation, buildings, water bodies, and even moving objects.

1.4 Project objectives and methodology

This project's main objective is to conceive a mechanism for the deployment of SAR antennae plates that will be coupled to a satellite for in-orbit demonstration. Under this main objective, the milestones are to produce a preliminary CAD design of the concept of the mechanism with some detail, followed by some first structural analysis iterations to produce a better product capable of handling launch loads. The final product does not have to be a ready-to-manufacture concept but rather a study of different possibilities and mechanisms, along with structural studies that will further help to define its future configuration. That said the process starts by recognizing possible deployment options and doing some preliminary designs either by hand or, in a later stage, in Solidworks 2022. Then one of the designs is chosen and transported to ANSYS to perform Quasi-static, Sine equivalent, and Random Vibration analysis.

Chapter 2

State-of-art and literature review

In the present chapter, a compilation of important subjects and information was produced to aid the investigation and help the reader understand all of the concepts presented in this text. As is known, space presents harsh conditions, and difficulties in design, and is not the familiar environment technical people are used to working in. This ultimately leads to a lack of experience in the area from people outside the sector, therefor a strong basis should be acquired prior to starting working on a related project. Besides, for someone willing to develop some structure that should orbit the Earth, the load environment experienced during the travel to space should be something to be concerned with, guaranteeing that the structure is strong enough to survive to launch and still remains light as possible. This later point brings with it a solid analysis background to perform the job well. Having this said the chapter is organized in a way to expose relevant information in a sectioned way. Starting with Section 2.1, the space environment, its environmental conditions, and subsequent impact on structures are exposed. Following is Section 2.2, where history and state-of-art on space mechanisms can be followed to understand the mechanical principles and configurations mostly used, serving as inspiration for design purposes as well. Section 2.3 then goes through the mathematical background that will be needed when performing structural analyses, which are detailed in Section 2.4, overviewing important concepts and main structural analyses performed in the sector. Finally, Section 2.6 is dedicated to materials typically used in the field, their impact on design, and the materials used in the analyses.

2.1 The space environment

When launching a spacecraft into space, one of the most important aspects to consider when designing it is the environment it will be subjected to. Mechanical engineering in general is used to work with structures near the earth's surface and under the atmosphere whose effects are well understood by an engineer. When traveling to the upper regions of the atmosphere, environmental effects can be harsh on the structure. In the case of the present work, the mission will be considered in low earth orbit (LEO) encompassing the region between around 160 km and 1000 km of altitude [10]. In this region, such environmental agents include atomic oxygen, radiation, plasma belts, thermal cycling, and high vacuum. The ones with a higher impact on the mechanical design will be described along with their implications on the design and material choice, finally, other types of environmental agents not so relevant will be briefly referred to.

2.1.1 Atomic oxygen

Although with a scarce atmosphere, the low orbit region can be harsh on materials, corrosion being present even in these environments. The main protagonist of such events is atomic oxygen (ATOX). It is the prevalent chemical species in LEO and it is formed by bond breakage of O_2 molecules at the absorption of a photon below a wavelength of 0.234 µm (UV spectrum) [11]. Its abrasive nature comes not only from its chemical activity but also from its impact energy when hitting the spacecraft at around 8 km/s [12] from the relative velocity between the two. Concerning its activity, the atom reacts strongly with materials containing carbon, nitrogen, sulfur, and hydrogen bonds, thus polymers and their molecular bonds will be particularly sensitive to this environment. Even with the use of special protective coatings, undercutting erosion can develop in defect sites [13]. The impact component is characterized by 4.5 eV of collision energy [11] and nominal flows of 10^{14} - 10^{15} atoms/(cm^{2}s) can be expected, with the latter varying with altitude, orbital inclination, solar activity, and time of the day [14]. Consequences of such impact are erosion, fragmentation of high molecular chains that lead to the formation of volatile condensable material, a possible contaminant for nearby surfaces, formation of stable oxides, scattering, and chemiluminescent glow. The former degrade material properties irreversibly and is something to take into account in the coatings, structural materials, thermal blankets, solar panels, optical components, and material choice in general. ATOX erosion is measured by volume loss per incident atom and erosion yield values for typical polymers used in space applications can be seen in the Table below. Also, stable oxide formation can change the properties of the material. When oxidized, a common lubricant, molybdenum disulfide turns into an

abrasive oxide [12]. Also, oxidation leading to erosion and mass loss was observed in some shuttle missions [11]. Finally, when taking a closer look at its consequences on polymers that, as spoken before are particularly susceptible to this phenomena, one can notice changes in optical properties, chemical composition, surface morphology, and formation of volatile contaminants [14]. Atomic oxygen attack in metals may be neglected as these resist well to the agent. Macroscopic effects are not present with the exception of Silver and Osmium. Aluminum alloys have good resistance in general except for the AA 2090, an Aluminum-Lithium alloy that displayed greater than expected mass loss during experiments, particularly lithium loss. Copper also has a good reaction to the agent [15]. Values of material loss and rating of polymeric materials in relation to mass loss are presented in Tables B.1 and B.2 of Appendix B.1 for informative purposes. An example of the effects of atomic oxygen attack on space structure is shown in Figure 2.1, where its effect on the solar blankets structure on the ISS is pronounced.

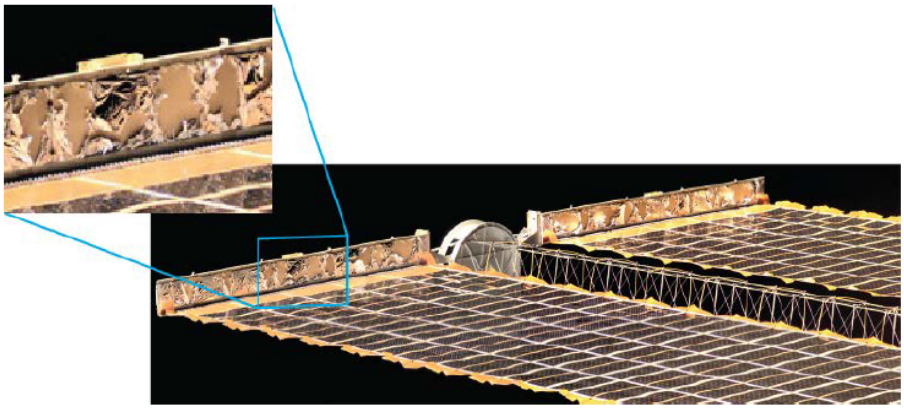

Figure 2.1: Atomic oxygen attack on ISS solar blanket structure. Taken from [13]

2.1.2 Radiation

The Sun is the main source of radiation reaching Earth and its orbits. It is the basis of life and its energy powers the planet's atmosphere giving us the radiation to see the world around us. Although visible light is an indisputably important part of our life it accounts for only a small portion of the Sun's spectrum, ranging from ultraviolet to infrared, in general, and being very close to that of a black body at 5800K [16]. Higher energy radiation results from scarce events or contributes to insignificant portions of the spectrum. The energy provided by the sun in the 0.115 – 50 µm range is denominated the solar constant and equates to 1366 W/m2 with slight variations depending on altitude and solar activity. UV radiation, with a range from 0.1 to 0.4 µm corresponds to only 8% of the solar constant but has enough energy to cause breakage of organic bonds. Solar radiation below 0.2 µm, is less than 0.001% of the solar constant but may promote dissociation of C=C and C=O bonds

(stronger covalent bonds) and functional groups, so once again polymeric materials will suffer the major impact. Crosslinking causing embrittlement of polymer surfaces and cracking, and degradation of mechanical properties are common problems. The co-presence of oxygen atoms and UVs can result in the coupled phenomena of photo-oxidation where the results of the reaction from the two environmental agents may bond together, leading to discoloration, loss of transparency, and an impact on the electrical properties by the formation of polar groups [11, 14]. UV can also impact the transmittance of thermal control coatings resulting in decreased efficiency of thermal control. In contrast to atomic oxygen which tends to bleach materials in space UV darkens materials as depicted in the figure below.

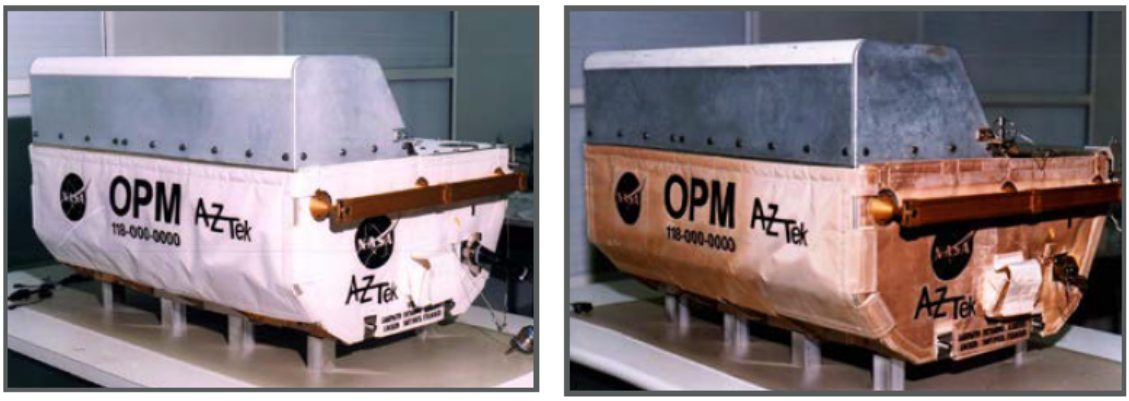

Figure 2.2: Visible effect of UV radiation on an Optical Properties Monitor after nine months of exposure on the Mir Space Station. Taken from [13]

Other types of radiation as ionizing radiation, radiation belts, cosmic rays, and solar particle events are also present at satellite altitudes and although very energetic and potentially harmful for the structure, they are very residual or do not often occur. Thus their effect is normally small and out shadowed by the atomic oxygen and UV ones with their consequences being very similar to those of UVs. Its biggest impact is felt on the avionics with the so-called single events [13]. The latter may induce a logical error in the equipment leading to a false order which can be easily solved by implementing redundancy making a comparison with two other similar orders, being the different one excluded. Further implications can also be found in metals where a displacement of atoms from the crystal lattice, together with an ionizing track caused by penetrating radiation leads to the formation of whiskers [12].

2.1.3 Outgassing

The high altitudes where spacecraft orbit are characterized by a scarce atmosphere, and therefore a very low ambient pressure. At such altitudes high vacuums

on the order of 10^{-6} - 10^{-9} Torr can be found, at which some materials and volatile specimens, reaching their evaporation pressure, start to sublimate [13]. Any material in a vacuum will lose mass, the material on the surface will evaporate, and molecules adsorbed will desorb [17]. This phenomenon, commonly known as outgas, leads to the formation of volatiles whose molecules can deposit on line-of-sight surfaces with a special tendency to lay on cold ones. These can affect optical properties, payload surfaces, and spacecraft performance. A way to reduce or mitigate such phenomenon comes from, vacuum baking above the temperatures encountered in orbit [13]. In terms of material implications, material strength and fatigue life are affected by high vacuum environments, with fatigue life normally having an increase. There are two main hypotheses for this, one is that gases absorbed into surface cracks can aid or hinder crack propagation. In the second one, oxidation and gas diffusion absorbed into the material influence its bulk properties [12].

Once again, polymers will describe well the typical effects of such environmental agents as they are the main materials affected. Its characteristic volatile components are low-molecular-weight fragments, additives (like plasticizers), and absorbed gases [14]. The values of pressure found in LEO lead to their outgassing, resulting in mass loss and the formation of volatile contaminants that affect the structure surrounding it. In figure 2.3 the deposition of brown-colored volatiles into an aluminum surface is well visible.

Figure 2.3: Brown-colored volatile contamination on aluminum. Taken from [17]

The previously discussed implications on spacecraft missions and instruments are well represented by the outgassing of vulcanized silicone rubber in the sealed motor switch aboard the Apollo 14 mission. The result (figure 2.4) was a motor failure and severe flare experienced by the narrow viewing angle camera on the Cassini spacecraft caused by contamination of the optical instrument from outgas volatiles [17].

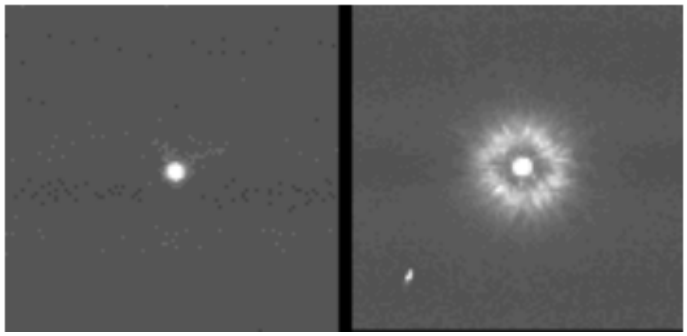

Figure 2.4: Cassini camera flare due to contamination. Taken from [17]

While polymers dissolve high quantities of molecules, particularly water, metals are limited in that regard except for hydrogen atoms. The huge quantity of dissolved gases plus the relative ease in moving through the polymeric chains lead to polymers having a higher outgassing rate. To do the comparison, in a metal, the average distance traveled by a hydrogen atom in the lattice in a day is 4 μm while an oxygen atom does that same distance in 1000 years. In a high-performance polymer as in the case of PEEK the distance is 20 μm for oxygen [18]. Values for outgassing of several materials can be found in [19]. Below one can see different outgassing values for metals and polymers represented in mbar/(s$\cdot$ cm^2) which translates to the pressure increase rate in a controlled outgassing test by the dispersion of gases from the test material to the chamber.

Table 2.1: Typical metals' outgas properties. Taken from [18]

Materials	Bakeout T[°C] x 24 h	q [mbar l s^{-1} cm^{-2}]
Austenitic st. steel	150	3 10^{-12}
Austenitic st. steel	200	2 10^{-12}
Austenitic st. steel	300	5 10^{-13}
Copper Silver added (OFS)	150	3 10^{-12}
Copper Silver added (OFS)	200	≈ 10^{-14}
Beryllium after brazing	150	< 10^{-14}
Al alloys	150	< 10^{-13}

Table 2.2: Typical polymers' outgas properties. Taken from [18]

Polymer	Unbaked, 1 h pumping	Baked, ultimate
Fluoroelastomer	4×10^{-7}–2×10^{-5}	3×10^{-11}–2×10^{-9}
Buna-N	2×10^{-7}–3×10^{-6}	—
Neoprene	5×10^{-5}–3×10^{-4}	—
Butyl	2×10^{-6}–1×10^{-5}	—
Polyurethane	5×10^{-7}	—
Silicone	3×10^{-6}–2×10^{-5}	—
Perfluoroelastomer	3×10^{-9}	3×10^{-11}–3×10^{-10}
Teflon	2×10^{-8}–4×10^{-6}	—
KEL-F	4×10^{-8}	3.5×10^{-10}
Polyimide	8×10^{-7}	3×10^{-11}

2.1.4 Other environmental agents

The main environmental hazards for space structures in low earth orbit were described above but they are not the whole picture. Problems like space debris and micrometeoroid impacts, plasma interaction, and thermal cycling are very real concerns in spacecraft design as well and can affect the operation lifespan of satellites and structures.

Micrometeoroids are present in LEO and can impact the structure leading to damage and degradation of surface thermal properties, but impact-prone material can also have a human origin. The latter, mainly constituted of aluminum oxide dust with an average velocity of around 11 km/s relative to the spacecraft, can erode surfaces and penetrate protective coatings [12].

A variety of charged particles, mainly electrons and protons are present on the Earth's magnetosphere. The ionosphere goes up to 1000 km in altitude, characterized by a cold plasma in the 1 eV energy range and consists of neutral and ionic components and a density of 10^6 of these elements per cm^3 [20]. In LEO, the plasma environment around a spacecraft is composed of positively charged oxygen ions and free electrons. When traveling, the spacecraft will be hit by the ions only in the ram direction (surface facing the direction of the velocity vector) while the rest of the spacecraft is impacted by the free electrons. There may be then a negative charging by the spacecraft which leads to problems such as ion sputtering, arcing, parasitic currents in solar arrays, and re-attraction of contamination [13].

Finally, thermal cycling is of utmost importance in design. In the absence of air to exchange heat from the structure to the exterior, it is limited to radiation exchange and conduction through the satellite, cooling systems can also be incorporated in the satellite. Therefore the temperature is highly related to the surface thermo-optical properties particularly, absorptance and emittance. Other factors that influence the spacecraft's temperature are its inclination towards the Sun and the Earth, the

projection of surfaces to these bodies or other spacecraft surfaces, sunlight, and shadow exposure duration, its thermal inertia, and equipment/components' heat loads. As was detailed, several factors can change the temperature but as a rule of thumb, ± 120 °C are to be expected. In perspective, the ISS undergoes 16 thermal cycles a day. An interesting consequence of thermal cycling is that using different materials joined together, having different thermal expansion coefficients may result in crack formation on one material. For example, in ATOX protective coating, the oxygen can then enter and affect the underlying material [13].

2.2 Spacecraft mechanisms

In this section, a thorough literature review is done exploring the different deployment mechanisms that have been used or proposed for space applications. Following this, some important components of such mechanisms are highlighted finishing with a brief coverage of lubrication.

2.2.1 Mechanisms

Deployable mechanisms have a close relation with space. From the moment humans started launching satellites and vehicles into space, functions like energy harnessing, using antennas for communications, or even interaction with other space vehicles as in the case of the ISS, have to be guaranteed for the success of the mission. In space, construction in low/zero gravity is hard, for this reason, some structures are intended to be deployed, as these can be stowed in small spaces to then be extended to a bigger volume [21]. The main design criteria for these elements according to Kiper (latest reference author) are stowed compactness, dimensional tolerance, the rigidity of deployed configuration, ease of deployment, durability, reliability, and cost. The author further distinguished the assemblies into flexible and rigid. The latter is composed of rigid elements connected by rigid joints, offering good shape control with the complexity of parts, weight, and friction being the main disadvantages. The former is characterized by flexible elements and can have some rigid parts. These include cable strut assemblies, tensegrity structures, and inflatables. Their advantages are of course the opposite of the rigid structure disadvantages and can be very tightly packed. Inflatable systems particularly are very cheap, and offer good damping, and good thermal properties, but have very low reliability. A solution to this will come from rigidizible inflatables.

In terms of their operation spacecraft mechanisms can be subdivided into one-shot devices and continuous operations devices. The former includes hold-down and release mechanisms and deployment devices. Continuous operation device examples are SADMs (Solar Array Drive Mechanisms) to rotate the solar arrays towards the

sun, pointing mechanisms, scanner mechanisms, and momentum and reaction wheels [22].

This section is inspired by [12]. The disposition of sections and base information follow the book. It is from the base given by the reference that further research was conducted to further elaborate on each part an produce more through knowledge on the subjects.

Spacecraft structures take advantage of a variety of mechanisms to assure compactness when stowed to then extend into larger elements. Springs are one of the most used methods for the deployment of space structures, normally accompanied by dampers to control the movement until latching. The Intelsat V, an old communication satellite, is a representative spacecraft of the principle of deploying panels through the use of torsional springs. The springs are the motor behind the movement, with the torque coming from the stored elastic energy. The panels open in a harmonica-like way, resorting to a closed cable loop (CCL) system that synchronizes the angles between the panels when opening by transferring torque between the hinges [23–25]. The CCL is an important idea that was used in this work for the synchronization of movement and is depicted in Figure 2.5. An important characteristic of the cables is the presence of springs to compensate for temperature expansion, which could lead to loose or over-tensioned cables [26, 27].

The state of the art in commercial satellites recurs to sandwich panels multi-joint PV cells of high efficiency employing similar mechanisms to the one described. The Dawn spacecraft, developed to explore the 2 biggest asteroids in the asteroid belt, Ceres and Vesta [28], and the Boing 702 are examples of the use of these mechanisms in commercial satellites [29]. Other approaches to the deployment of solar arrays include also flexible rolled-up blankets and semi-rigid concertina folds. Rigid supporting structures are commonly used to attain the expected rigidity and have good reliability, as examples one can use a foldable truss structure [30], simple rigid bars attached to the panels that lock when deployed [31] or pantograph mechanisms as the one employed in the Scarlet I project from NASA. The latter relied on the PUMA (Pantographic Unfolding Modular Array) which consists of a two cross bars scissor-like mechanism repeated along its intended length, as shown in Figure 2.6. This approach guarantees, intrinsic deployment synchronization, high specific power, high reliability, small, stowed volume, lightweight, structural strength, and stiffness. It was found that not fully extending the pantograph and leaving a small angle, 5° in the given case, lead to a 7.5× increase in first natural frequency having almost no impact on PV efficiency.

An alternative stored elastic energy hinge is the tape spring, a self-locking mechanism, although not as restraining as the hinge with latching type. Figure 2.7 presents

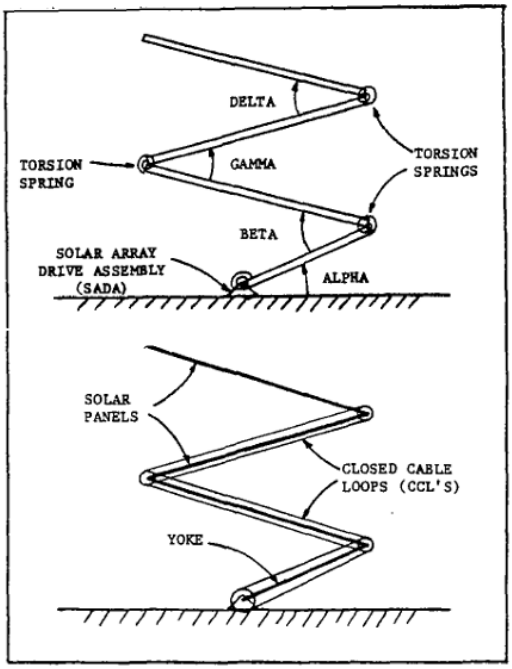

Figure 2.5: Closed cable loop mechanism. Taken from [27]

the concept. A hinge is created by connecting two parts with strips of carpenter-like metallic tape. It presents high repeatability, pointing accuracy, and is self-locking. Still, mechanical shock is present at the end of the movement. A real-world application was its use on the MARSIS antennas and, following the same architecture and concept, composite deployable booms, that can be cut on the sides to create local hinges, were first proposed by ESA in 2016. The major confronting requirements that make the design of such structures difficult are the need for flexibility to make it compact and rigidity for vibration response purposes [33].

When long structures need to be deployed from a side of the spacecraft, one can take advantage of telescopic booms. They can extend relatively far and are very reliable, also displaying good deployed natural frequency, but on the other side, they take a significant amount of stowed volume and can be heavy. An example is the ISIS (inflatable sun-shield in space) telescopic boom with a deployed first natural frequency of 1.7 Hz but weighing 50 kg and extending to a maximum of 6-7 meters [35]. Deployment booms have the advantage of being highly compact, thus solving the packaging problem, therefore having small, stowed volumes, that deploy into a long structure. Examples of such configurations are STEM and BiSTEM (Storable Tubular Extendable Member). Their working principle is similar to that of carpenter tape and a depiction of them is shown in Figure 2.8. The boom is made with metal or composite thin shells that are elastically flattened and rolled on a reel. They are then unrolled, resulting in a compactable, long, slender element. These represent the older boom technologies, later, booms composed of two flattened

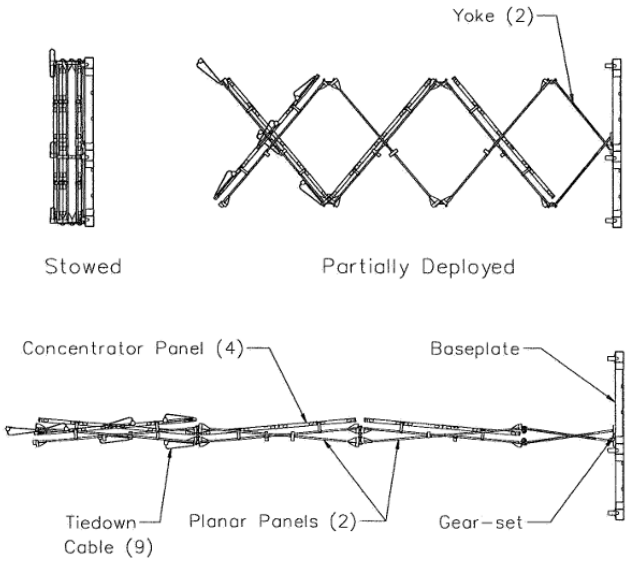

Figure 2.6: Pantographic mechanism. Taken from [32]

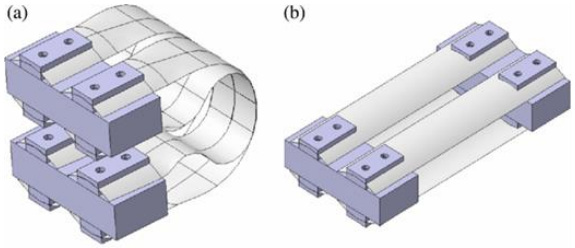

Figure 2.7: Tape spring. Taken from [34]

and welded/bonded on the sides flat springs were constructed. By playing with the boom's crosssection, good structural properties like bending stiffness can be achieved. Typical problems are thermal bending if one side faces the sun, and the other doesn't, and shear stress accumulation on the welded/bonded zones. The latter may be solved by other designs which unfortunately may lower structural properties or involve more complex mechanisms [12, 16]. At the German Aerospace Centre or DLR, ultralight and stiff CFRP deployable STEM booms were developed, for the deployment of a large SAR flexible membrane, composed of 4 triangular parts with 87 m^2 each. Booms consist of two omega-shaped Kapton-coated composite shells bonded in the flat section, that can be rolled and then controlled and deployed with the aid of brakes and actuators, moved by their stored elastic energy. This approach significantly reduces the SAR satellite mass and stored volume [6].

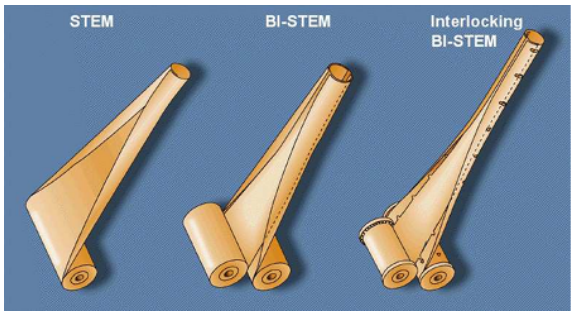

Figure 2.8: STEM deployable boom. Taken from [36]

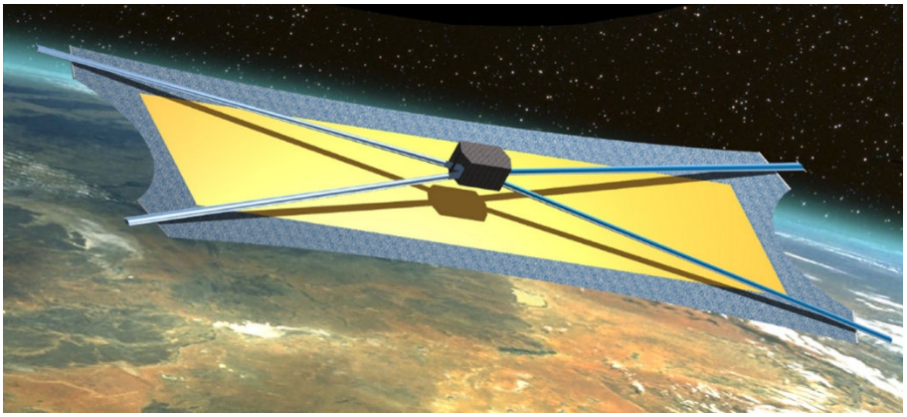

Figure 2.9: Large SAR membrane deployed and reinforced by STEM CFRP booms concept. Taken from [6]

The Stacer boom is a similar concept but, in this case, a coiled flat spring at an angle α, when released opens vertically [16]. More than 700 Stacers have been used in space missions as they display a reliable and efficient deployment playing an important role in EM field monitoring and solar sail deployment [37]. Finally, there is also the possibility to use rigid elements, with motors on their joints for deployment and controllability, as in the Canadarm2 on ISS [35].

Other examples of long pre-deformed structures are deployable truss structures and deployable lattice masts. The former includes tensegrity structures, which are truss structures that use cables instead of rigid bars when under tension. The ADAM (Able Deployable Articulated Mast) illustrates well this concept (figure 2.13), having already been used in space missions. Similar to the previous example is the CoilABLE boom which, in essence, are structures that use coiled longerons that store elastic energy and move the deployment as depicted in figure 2.13. It is more compact than the previous one while less precise and stable but can be used in solar arrays [35]. A good example is the AEC-ABLE CoilABLE mast used on the imager for the MARS Pathfinder.

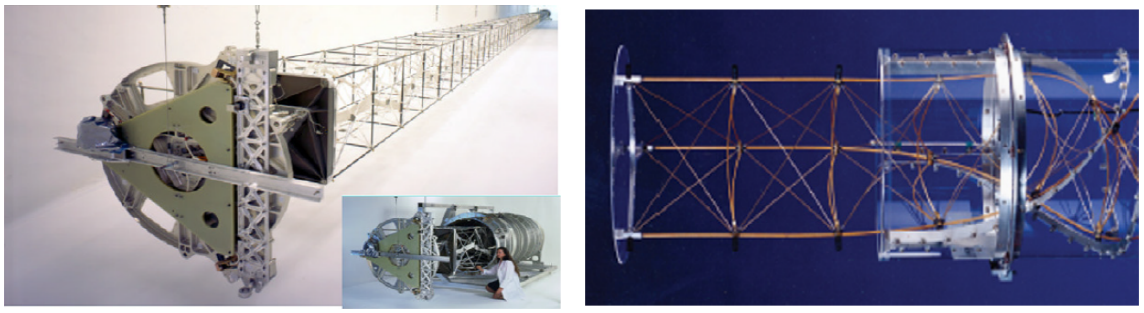

Figure 2.10: ADAM (left), CoilABLE (right). Taken from [35]

Still, within the boom concept, inflatable booms have also been employed in space applications and will also serve to introduce the concept of inflatable structures. These booms present low deployment accuracy and post-deployment stability, their advantage comes from being ultra-lightweight and having a big packaging ratio, where they can be flattened and rolled, these being the main advantages of inflatables in general as they can open into very big surfaces [35]. Another disadvantage, which will be referred to again a little later comes from the need for constant inflation pressure and the fact that space debris might compromise these spacecraft elements by rupturing them, having therefore low reliability.

The spacecraft community has in general classified large space structures into mechanical and inflatables. A new category is that of rigidizible inflatable structures. These have been recognized by NASA and DARPA as enabling technology for space applications and obtaining large structures where compactness is key. Benefits common to inflatable structures are a high compaction ratio, increased design flexibility, and reduced complexity. It overcomes some difficulties of its contestants like high coefficients of thermal expansion, and a need for constant gas input to maintain inflation, plus it displays higher stiffness and accuracy. Many types of mechanisms exist to give rigidity to the structures, the main principle is to inflate the structure and then through heat, radiation or vacuum turn the structure rigid. This approach will result in the possibility of different packing configurations and have a more continuous structure with fewer parts [38]. In their work, Lin et al. use composites with shape memory properties. The shape is established at the beginning of the curing cycle, when cured, it is heated to the folding temperature, packed, cooled, and reheated when the unfolded shape is needed.

An interesting concept that might bring new possibilities to the design of deployable structures is the Japanese art of origami. It recently gained worldwide recognition and started entering the engineering world, applying to new structures and mechanisms. There are several circumstances that motivate its use, one of them being the stowage of a large flat structure in a tiny space that can then be

unfolded [39]. The space industry revealed its interest in this topic as they always run on space constraints and increasingly bigger energy requirements. Origami-inspired deployable systems enable compact stowed volume that results in a wide area structure when deployed. Panel thickness and rigidity are the main challenges of origami-inspired designs. Tachi achieved foldability alternating the position of the rotation axis on the upper and lower surface between the panels. The first leads to the so-called "mountain folds" and the latter, valley folds as depicted in the Figure below [40].

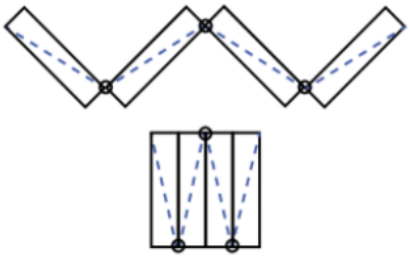

Figure 2.11: Folding of thick panels [40]

The Miura-Ori fold is space employed origami pattern. It resembles a map fold as can be seen below. Increasing the angle of the creases in the folding pattern results in a more synchronous x and y unfolding. Invented by the Japanese astrophysicist Koryo Miura to be used on solar arrays, which was unfolded in 1995 on the Japanese satellite, the Space Flyer Unit and it can be opened by just pulling one corner [40, 41].

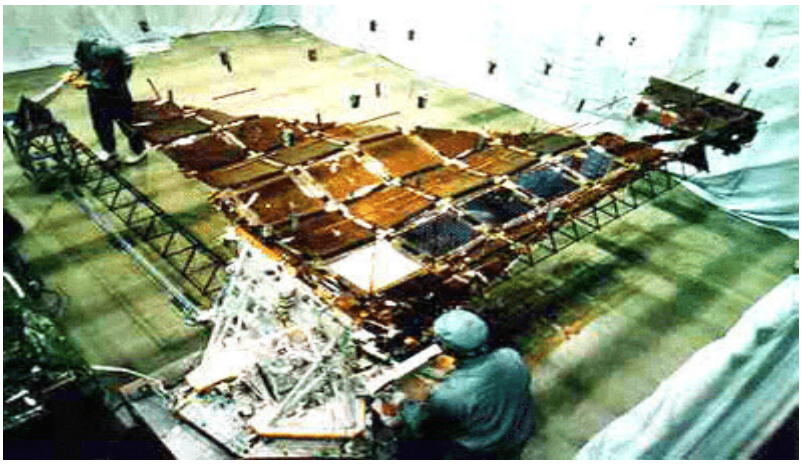

Figure 2.12: Miura-Ori pattern foldable solar array aboard the Japanese Space Flyer Unit. Taken from [29]

In 2014, NASA also developed a prototype of an origami-inspired solar array [42].

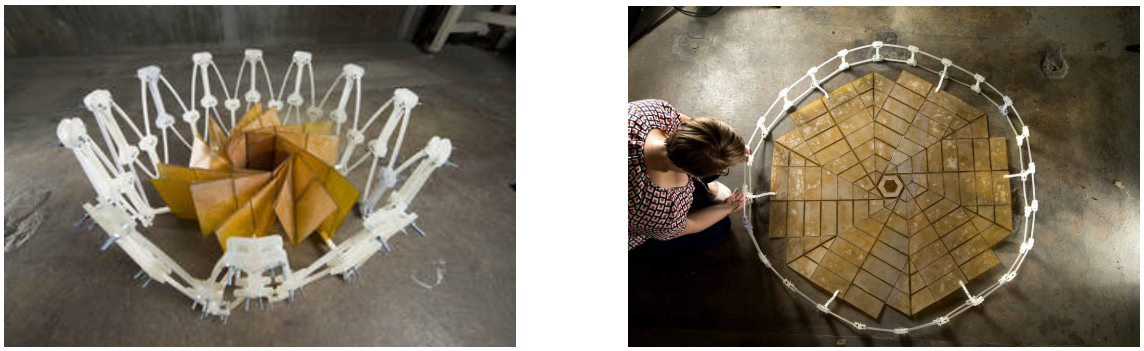

Figure 2.13: NASA's origami folding pattern deployable solar array prototype. Taken from [42]

2.2.2 Components

In this section, the major parts of deployable architecture are highlighted and briefly described as these will be important for design.

2.2.2.1 Pulleys

Pulleys and cable systems, play a significant role in the opening of large space structures and the synchronization of deployment previously talked about. The CCL system has been employed in numerous satellite technologies, other applications can be seen in guiding the movement of deployable truss structures or opening of large ring structures that support flexible blankets of antennas [12, 23–25].

2.2.2.2 Dampers

When deploying something by stored elastic energy, the movement can speed up enough to be dangerous for the structure itself at the moment of locking in place. A great shock can propagate through the structure and damage itself. Dampers are usually used for the dissipation of this kinetic energy and to assure a smooth deployment and latching. Another application of these components is for vibration suppression.

In viscous/fluid dampers the fluid dissipates the energy due to pressure loss and shear action of the oil. A particular example is linear viscous dampers where, the mechanism of damping consists of a housing, a piston, a rod, and a sealant element. When the piston moves, pushes fluid through the tight gaps between itself and the chamber, leading to a great increase in velocity that in turn results in big pressure losses due to the shear action of the silicon oil against inner walls, therefore dissipating energy. These types of dampers have the advantage of being wear-free [43]. Rotary viscous dampers operate in a similar manner and are composed of a

rotator, a stator, and a thin film of oil between the two, the shear force from the oil will slow the movement.

Eddy current dampers have the advantages of no contact, no leakage, and easy implementation. The principles of this type of damper set foot on the principle of repulsive electromotive force when there is a variation in the magnetic field. The usage of such dampers appeared in the cryogenic system of the space shuttle [44]. A good review on the application of eddy current dumpers can be found in [45]. Employing the same principle, in [46] the author used a brushed DC motor as a rotational speed damper. It is coupled to a small gearbox to enhance the change in the magnetic field. The motor is mounted on a closed circuit with a variable resistor element that allows for a change in the damping coefficient related to the change in resistivity. These dampers offer in the end a good and reliable solution as they do not need maintenance and don't have contacting parts, being thus wear-free. On the other hand, liquid-based viscous dampers have a temperature-sensitive damping coefficient, can suffer from liquid outgassing, and need precise fabrication to avoid bubbles. Mechanical breaks show low reliability and induced vibrations.

2.2.2.3 Electric motors

Electric motors are good sources of power for the movement of structures as in the previously referred ISS Canadarm 2. They can be used to open and close panel arrays or truss structures and to control the deployment either driving it or acting as an eddy current damper. The three main types used in space are brushed motors, brushless motors, and stepper motors. Brushed motors are inexpensive and easy to find, but have drawbacks such as brush dust, low efficiency, short lifespan, limited speed, and poor thermal characteristics in vacuum. On the other hand, brushless motors offer higher efficiency and no brush debris, but are more expensive and have higher motor drive complexity. Stepper motors do not require commutation feedback but can face issues under high inertia loading [31].

2.2.2.4 Gears

The design and use of gearboxes and gear assemblies in space differ from those in industrial applications due to reduced allowable tooth loading and limitations in the choice of lubricants and material pairing. The toothed module, which is chosen based on the tooth load present, the accuracy of transmission, and the gear ratio, is the most important parameter in defining the gearing. Two stresses, the Hertzian or contact, and the bending root stresses must be considered, with a general rule of thumb of a maximum of 10 N per mm of tooth width for metal gears and one-tenth of this value for plastic gears. Materials used include metals such as carbon, stainless and maraging steels, cast iron, bronze, aluminum, and titanium,

with suitable surface treatments, and plastics such as polyimide and polyacetal, often loaded with molybdenum disulfide or carbon fiber. Lubrication in space is challenging, as most lubricants are not suitable. For highly loaded plastic gears, solid lubricants such as polytetrafluoroethylene (PTFE) or molybdenum disulfide are used, while thin metal films or molybdenum disulfide are used for metal gears under higher loads. Redundancy may be achieved by the use of differential gears, but this is not commonly used due to the rarity of situations that require it [47].

2.2.2.5 Restrain/Release elements

Besides guaranteeing the motion of a certain structure there is also a need to restrain it well enough to handle the harsh launcher environment, prevent it to open when not wanted, and to release it at will. Release mechanisms will be described but it is to be noted that some work as restrain mechanisms also or refer to them. The main release agents for space mechanism rely on pyrotechnics, as they present very good energy efficiency, are very reliable, and operate very quickly. Although not obvious, redundancy can be achieved in these types of devices from more than one ignition initiator and redundant firing circuits. The main applications include pin pullers/pushers, cable/bolt cutters, and valve actuators. Another common mechanism used since the early space exploration days is the Marmon clampband-like mechanism, which relies on two cylindrical parts secured by a circumferential belt held by bolts. At deployment, bolts are cut and the belt is removed with the aid of torsional springs. Linear springs pre-compressed help with the separation. They are commonly used for connecting different sections of the launch vehicle that will need to be separated. The main drawbacks of these are the explosion-induced shock on the structure. A shockless alternative is the use of memory metal alloys, composed mainly of nickel and titanium, that are deformed, passing through a phase transformation between austenitic and martensitic states, and can return to their original shape above the transformation temperature. An interesting application of the latter idea is the frangibolt where the return to the original shape leads to an increase in tension of a pretensioned bolt with a circumferential notch resulting in the breaking of the screw.

Other examples include paraffin actuators, solenoid pin pullers, and the burn wire technique. Paraffin actuators are characterized by an assembly of a movable pin, a housing, and a zone filled with paraffin wax. When heated the wax can expand by 25% and create an increase in pressure inside that drives the pin. Solenoid-actuated pins move by the magnetic field generated and they are simple, compact, and do not require any lubrication. The Wire principle is simple, a Nichrome wire, burns another wire, usually made of Kevlar/Vectran, where it may be rolled around, that is securing de deployable. When electrical current is passed through the burn wire,

it gets hotter by the joule effect and melts the holding wire, releasing what is needed. The tensile strength of the wire influences the current needed, increasing it, therefore, this type of approach is best suited for small devices [16], Below, one can see a Table from the book with a good comparison between some of these elements.

Mechanism	Force	Size	Weight	Power	Cost
Explosive Bolt	Large	Relatively Small	Low	Moderate Pulse	Moderate
Explosive Bolt-Wire Cutters	Large	Relatively Small	Low	Large Pulse	Low
Solenoid Pin Pullers	Moderate	Medium	Medium	Large	Low
Paraffin Pin Pushers	Medium	Relatively Small	Medium	Moderate	Moderate
Motorized Cams	Large	Medium-Large	Large	Low	High
Fluid Dampers	Large	Medium	Medium	High	High
Magnetic Dampers	Medium	Medium	Medium	High	High
Governors	Medium	Medium	Large	None	High

Figure 2.14: Restrain/Release mechanisms pros and cons. Taken from [16]

2.2.3 Tribology

Tribology being the study of wear, friction, and interacting surfaces, faces a particular challenge in space but its design can dictate the success of space missions and the reliability of spacecraft mechanisms if well applied. The tribological components and lubrications must be robust enough to handle launch loads and survive the space environment. The loads and fretting at the mechanical interfaces can deform them plastically and/or cold weld in the absence of proper precaution. The main complications in these environments are the high space vacuum, temperature extremes and radiation, with the latter being less important as the surrounding metal normally shields these components from the radiation. Normally used lubricants cannot handle such temperature extremes where an increase in viscosity above feasible levels at low temperatures and thermal breakdown at higher temperatures are a reality. Space vacuum makes low volatility oils like perfluoropolyether (PFPEs), multiply alkylated cyclopentanes (MACs) and polyalphaolefins (PAOs) evaporate, the temperature increasing the rate. These aspects make the use of fluid lubricant impractical below -40 °C and above 100 °C. The two most commonly used space oils are the Fomblin Z25 (a PFPE) and the Nye 2001a (a type of MAC). Labyrinth seals can be used to greatly impede oil evaporation. Another mechanism of oil loss is surface migration, for this, creep barriers may be used which stop oil spread due to its low surface energy.

Other types of space lubrication include greases and solid lubricants. The former is usually used in gears and occasionally on ball bearings, since at the operation

speeds of these latter elements greases would display higher torque loads than the oils. The most used grease types are based on the most used oils PFPEs and MACs. Solid lubricants are used in areas that will experience temperature and contamination issues that would appear if liquid lubricants were used. They are low-shear materials with graphite being one of the most well-known, although its lubricant effect is in part due to the presence of water vapor which is not present in space and therefore tends to wear rapidly. Their uses follow one of two routes: the application of thin coatings or the use of self-lubricating materials. In the former, thin ($< 1\mu m$) coatings are physical vapor deposited (PVD), examples are sputtering and ion-plating, of these two techniques come the two most used space lubricants, sputtered molybdenum disulfide (MoS2) and ion platted/sputtered lead (Pb). Molybdenum disulfide is composed of trilayers of S–Mo–S connected by Van der Waals forces on the Sulphur atoms interface allowing for sliding between the layers. On the other hand, the lead low friction comes from the high density of dislocations in the lattice. Care must be taken with MoS2 since in the atmosphere, the presence of water increases the friction of the material thus, the pre-launching environment should be controlled. The upper limit temperature of lead lubricant operation limits its applications. These two are used mainly in precision bearings, gears, and screws. Self-lubricating materials rub against sliding surfaces wearing out and releasing lubricant particles to the counter surface, resulting in discontinuous film, poor adherence, and frictional noise. The most used materials are polyimides and PTFEs. Their higher thermal expansivity needs to be considered in the design and it has a propensity to shrink under thermal cycling. Leaded bronze is also used as a self-lubricating material. The following section was based on [22] as it presents a very good summary of the tribological elements of space applications.

2.3 Dynamics background

Before over-viewing the types of analysis described hereafter, it is important to expose some concepts for a better understanding of what will be discussed. In this section, some mechanical vibration concepts will be reviewed along with the concepts of natural frequency, differential equations of motion for the single degree of freedom (SDOF) system with and without base movement, and the extrapolation to the multi-degree of freedom to then explore the eigenvalue problem for the determination of the natural frequencies and modes of the system. Afterward, the frequency domain in vibration analysis will be introduced along with the concepts of frequency response functions, effective parameters, and the formulation of the equations of motion in the frequency domain and the mode superposition principle. Then, a brief coverage of damping will be held for a posterior understanding of concepts. Finally, the finite element method will be quickly reviewed.

2.3.1 Mechanical Vibrations - 1 DOF system

The following simple system is the common SDOF used to initiate the study of mechanical vibrations. It is composed of 3 elements, a mass or inertial element, a spring or elastic element, and a dashpot or damper.

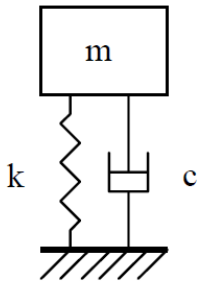

Figure 2.15: Single degree of freedom damped system. Taken from [48]

Employing Newton's second law, Lagrange mechanics, or Hamiltonian mechanics one can arrive at the second-order differential equation of motion of the system for the free (not forced) configuration Eq. (2.1). The below formulations are taken from [49], the x coordinate of motion was replaced by u for consistency with other references.

$$m\ddot{u} + c\dot{u} + ku = 0 \tag{2.1}$$

The motion of the mass is then defined by the above equation and the below initial state of the body:

$$\begin{aligned} \dot{u}(t=0) &= \dot{u}_0 \\ u(t=0) &= u_0 \end{aligned} \tag{2.2}$$

The solution to the homogeneous second order differential equation 2.1 takes the form (along with its derivatives):

$$\begin{aligned} u(t) &= Ce^{st} \\ \dot{u}(t) &= sCe^{st} \\ \ddot{u}(t) &= s^2Ce^{st} \end{aligned} \tag{2.3}$$

from which the equation of motion can be written as:

$$(ms^2 + cs + k)Ce^{st} = 0 \tag{2.4}$$

with solutions:

$$s_{1,2} = \frac{-c}{2m} \pm \sqrt{\left(\frac{c}{2m}\right)^2 - \frac{k}{m}} \tag{2.5}$$

Taking the term inside of the square root as zero and solving for c one arrives at the so-called critical damping:

$$c_c = 2\sqrt{mk} = 2m\omega_n \tag{2.6}$$

where ω_n is the natural frequency of the system,

$$\omega_n = \sqrt{\frac{k}{m}}. \tag{2.7}$$

The above parameter is one of the most important to characterize any vibrating system as it is the frequency at which, in the absence of damping, the system vibrates naturally. Another important parameter is the damping ratio, defined as the ratio between the damping of the system c and its critical damping c_c,

$$\xi = \frac{c}{c_c} \tag{2.8}$$

from where, substituting c_c as in (2.6) one obtains the well know expression of Eq. (2.9)

$$\xi = \frac{c}{2m\omega_n}. \tag{2.9}$$

For the case of a forced response, the right end term of Eq. (2.1) takes the form,

$$m\ddot{u} + c\dot{u} + ku = f(t) \tag{2.10}$$

where $f(t)$ is a general excitation. For the case where F can be expressed as a harmonic excitation

$$f(t) = Fcos(\omega t) \tag{2.11}$$

the steady state solution $u(t)$ will follow the same frequency ω and is of the form:

$$u(t) = \frac{U_s}{\sqrt{(1-\beta^2)^2 + (2\xi\beta)^2}} cos(\omega t - \phi) \tag{2.12}$$

where U_s is the static displacement F/k, β is the ratio between the the frequency ω and the natural frequency of the system ω_n

$$\beta = \frac{\omega}{\omega_n}. \tag{2.13}$$

The amplitude and the phase are defined by,

$$\begin{aligned} U(\omega) &= \frac{U_s}{\sqrt{(1-\beta^2)^2 + (2\xi\beta)^2}} \\ \phi &= tan^{-1}\frac{2\xi\beta}{(1-\beta^2)} \end{aligned} \tag{2.14}$$

With these values, it is possible to define the amplification factor which is the ratio between the dynamic and static amplitude of the system,

$$\mu = \frac{U(\omega)}{U_s} = \frac{1}{\sqrt{(1-\beta^2)^2 + (2\xi\beta)^2}} \tag{2.15}$$

and it is worth noting that when $\beta = 1$ and $\xi = 0$, the value tends to infinity, one obtaining the theoretical maximum amplification. The frequency at which β is the maximum is called resonant frequency (ω_r) and is given by:

$$\omega_r = \omega_n \sqrt{1 - 2\xi^2}. \tag{2.16}$$

For low values of ξ, the resonant frequency is very close to the natural frequency of the system.

2.3.2 Mechanical Vibrations - n DOFs system

The behavior of a system with n DOFs is now discussed. Taking figure 2.16 as a schematic of a system of this kind, one can employ Newton's second law to each body and obtain an equation of motion for each one.

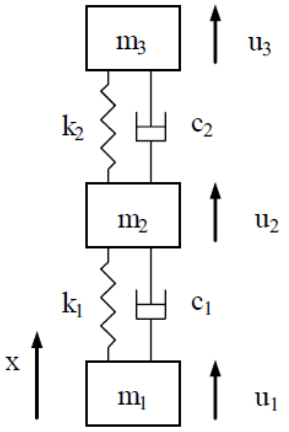

Figure 2.16: Multi DOFs system. Taken from [48]

It is then possible to assemble those equations since all DOFs are connected to each other by springs or dampers, the usual way is to express the equations of motion in matrix form:

$$[\mathrm{M}]\{\ddot{u}(t)\} + [\mathrm{C}]\{\dot{u}(t)\} + [\mathrm{K}]\{u(t)\} = \mathrm{F}(t) \tag{2.17}$$

where [M] is the mass matrix of the system, [C] is the damping matrix, and [K] is the stiffness matrix. F(t) is a given excitation that can be zero for the free regime or take any function of time. Now considering the above system of equations in the free configuration, including the damping term, and letting $u(t) = cos(\omega t - \phi)$ one arrives to:

$$[\mathrm{M}] - \omega^2[\mathrm{K}]]\{u\}cos(\omega t - \phi) = 0 \tag{2.18}$$

where the nontrivial solutions of the system are found taking the determinant of the matrix $|[\mathrm{M}][\mathrm{K}]^{-1} - \omega^2[\mathrm{I}]| = 0$ whose solutions ω_i^2 are the eigenvalues of the system.

By solving the eigenvalue problem of Equation(2.18) one finds eigenvectors or mode shapes of the system of equations $[\phi]_i$.

The above considerations are the foundations of the dynamics of a system. With the natural frequencies, the majority of the following analyses are possible as they rely on mode superposition. The system can be represented by a set of modes within the wanted frequency range instead of solving the equations of motion for all degrees of freedom saving substantial computational power as will be detailed later. Another substantial utility of obtaining the modes of the structure is for solving the system of equations in generalized coordinates.

The displacement vector can be represented by the matrix of mode shapes multiplied by a set of generalized coordinates $\{\eta(t)\}$,

$$\{u(t)\} = [\Phi]\{\eta(t)\}. \tag{2.19}$$

The resultant system of equations for the general case, by general case, meaning that $f(t)$ can be zero or any other function, after pre-multiplication by $[\Phi]^{\mathrm{T}}$ is:

$$[\Phi]^T[\mathrm{M}][\Phi] + [\Phi]^T[\mathrm{K}][\Phi] = [\Phi]^T\{\mathrm{f}(t)\}. \tag{2.20}$$

Taking advantage of the orthogonality properties of the modal vectors and mass and stiffness matrix relationship, a decoupling of the system of equations is attained. The mass matrix turns into an identity matrix and the stiffness matrix transforms into a diagonal matrix of eigenvalues:

$$[I]\{\ddot{\eta}(t)\} + [\Omega^2]\{\eta(t)\} = [\Phi]^T\{\mathrm{f}(t)\} \tag{2.21}$$

2.3.3 Dynamics in the frequency domain

After going through some basic concepts on vibrations, one should notice that the majority of it is formulated in the time domain. From what was found in the reference documents [48, 50] the generality of the analyses are performed in the frequency domain to sweep over a frequency range and see its influence, and also to save on computational cost as the analyses in the time domain are more challenging computational-wise to perform. It will be now introduced the frequency domain aspects to take into account for further understanding of the next subjects, following [48].

In the time domain, a given excitation $x(\mathrm{t})$ taking any form can be divided into small subdomains. If one takes the width of the subdomain to the limit, it becomes an impulse or a Dirac function. It is then possible to state that, by knowing the response to a unit impulse, it is straightforward to know the response to the

whole excitation, simply summing the contribution of each impulse and arriving at a convolution or Duhamel's integral,

$$y(t) = \int_{-\infty}^{t} x(t) h_{yx}(t-\tau) d\tau \tag{2.22}$$

where $y(t)$ is the response, $x(t)$ the excitation, τ the moment of the impulse and h_{yx} the response of the structure to a unit impulse.

In the frequency domain, the above relationship is expressed by a product rather than an integral.

$$Y(\omega) = \mathrm{H}_{yx} X(\omega). \tag{2.23}$$

The capital letter denotes that each variable is in the frequency domain. To do the transition one recurs to a Fourier transform, thus H_{yx} is the Fourier transform of the unit impulse response.

$$\mathrm{H}(\omega) = \int_{-\infty}^{+\infty} \mathrm{h}(t) e^{-i\omega t} dt \tag{2.24}$$

Complex functions representing the ratio between an excitation and a response in the frequency domain (be it displacements, velocities, acceleration, or forces) are usually called frequency response functions (FRF). For the general case of several excitations and responses the vectors $\mathbf{X}_x(\omega)$ and $\mathbf{Y}_y(\omega)$ can be respectively defined for the whole set of DOFs in the structure, with the matrix of FRFs $\mathbf{H}_{yx}(\omega)$ relating the two

$$\mathbf{Y}_y(\omega) = \mathbf{H}_{yx}(\omega) \mathbf{X}_x(\omega) \tag{2.25}$$

Now, the formulation to obtain the responses starting from the excitations in the frequency domain will be shown for the three types of motion discussed in this document.

- For sine motion with the excitation defined as:

$$x(t) = X(\omega) e^{i\omega t}, \tag{2.26}$$

  the amplitude $X(\omega)$ is multiplied by the FRF as in (2.23) and the phase of the excitation is summed with the FRF one. The result is:

$$y(t) = Y(\omega) e^{i\omega t} = \left(H_{yx}(\omega) \cdot X(\omega) \right) e^{i\omega t} \tag{2.27}$$

- For transient motion the excitation is transformed to the frequency domain, multiplied by the FRF, and transformed back again to the time domain.

$$x(t) \xrightarrow{\text{FT}} X(\omega) \xrightarrow{Y(\omega) = H_{yx}(\omega) X(\omega)} Y(\omega) \xrightarrow{\text{FT}} y(t) \tag{2.28}$$

- For random motion the relation between the excitation and response PSDs is defined as:

$$S_{yy}(\omega) = |H_{yx}(\omega)|^2 S_{xx}(\omega) \tag{2.29}$$

It is now important to make a distinction between the DOFs of the system. It is usual to separate them in the junction (boundary) and internal (remaining) DOFS as depicted in the picture below.

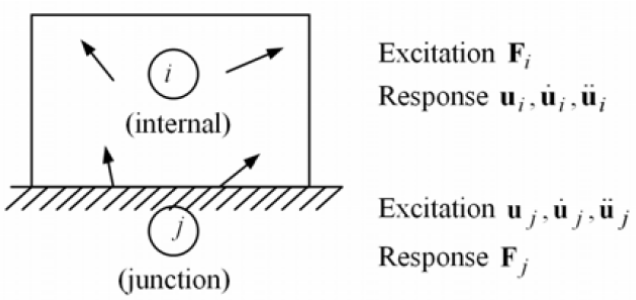

Figure 2.17: DOF distinction. Taken from [48]

In the presented notation, an excitation is defined as a base movement u_j and its derivatives $\dot{u}_j$, $\ddot{u}_j$, or a force applied to the internal degrees of freedom F_i. These excitations will generate two types of responses, a movement (and its derivatives) of the internal degrees of freedom $u_i, \dot{u}_i, \ddot{u}_i$ and a reaction force at the boundary F_j. Having these in mind the relations between excitation and a response can be defined which are nothing more than the frequency response functions of the mentioned excitations and responses. Below one can find a table with the FRFs and their relations to excitations and responses.

Table 2.3: Frequency response functions. Taken from [48]

Excitations / Responses	$\mathbf{F}_i$	$\mathbf{u}_j$	$\dot{\mathbf{u}}_j = i\omega\,\mathbf{u}_j$	$\ddot{\mathbf{u}}_j = -\omega^2\mathbf{u}_j$
$\mathbf{F}_j$	Transmissibilities (-) $\mathbf{T}_{ji}$ *	Stiffnesses (2) $\mathbf{K}_{jj}$	Impedances $\mathbf{Z}_{jj} = \mathbf{K}_{jj}/i\omega$	Masses (5) $\mathbf{M}_{jj} = \mathbf{K}_{jj}/(-\omega^2)$
$\mathbf{u}_i$	Flexibilities (1) $\mathbf{G}_{ii}$	Transmissibilities $\mathbf{T}_{ij}$	$\mathbf{T}_{ij}/i\omega$	$\mathbf{T}_{ij}/(-\omega^2)$
$\dot{\mathbf{u}}_i = i\omega\,\mathbf{u}_i$	Admittances (3) $\mathbf{Y}_{ii} = i\omega\,\mathbf{G}_{ii}$	$i\omega\mathbf{T}_{ij}$	Transmissibilities $\mathbf{T}_{ij}$	$\mathbf{T}_{ij}/i\omega$
$\ddot{\mathbf{u}}_i = -\omega^2\mathbf{u}_i$	Accelerances (4) $\mathbf{A}_{ii} = -\omega^2\mathbf{G}_{ii}$	$-\omega^2\mathbf{T}_{ij}$	$i\omega\,\mathbf{T}_{ij}$	Transmissibilities $\mathbf{T}_{ij}$

* Sign (-), the considered responses being the reaction forces, opposed to the transmitted forces

Other names:
(1) compliances, receptances
(2) rigidities
(3) mobilities
(4) inertances (ambiguous term, to be avoided)
(5) apparent masses

Having this said if one wants to define the relation between displacements and forces in the frequency domain, it is just a matter of employing the right FRFs in matrix form in the general case. An example is given:

$$\begin{bmatrix} u_i(\omega) \\ F_j(\omega) \end{bmatrix} = \begin{bmatrix} G_{ii}(\omega) & T_{ij}(\omega) \\ -T_{ji}(\omega) & K_{jj}(\omega) \end{bmatrix} \begin{bmatrix} F_i(\omega) \\ u_j(\omega) \end{bmatrix} \tag{2.30}$$

In this case, the relation between displacements is established. $u_i(\omega)$ is the sum of two components, a force multiplied by the compliance or flexibility and a base displacement multiplied by the transmissibility, or amplification (not to be confused with the terms discussed onwards of dynamic amplification, here the purpose was to show that the FRF in question amplifies the base displacement). The inverse happens for the force on the junction nodes.

The above FRFs can, in fact, be obtained by the product of a frequency-independent term and a frequency-dependent term. The latter is composed of two possible functions, the dynamic amplification $H_k(\omega)$ or the dynamic transmissibility $T_k(\omega)$, where these functions are given in Equation (2.31).

$$H_k(\omega) = \frac{1}{1 - \left(\frac{\omega}{\omega_k}\right)^2 + i2\xi_k\left(\frac{\omega}{\omega_k}\right)}$$
$$T_k(\omega) = \frac{1 + i2\xi_k\left(\frac{\omega}{\omega_k}\right)}{1 - \left(\frac{\omega}{\omega_k}\right)^2 + i2\xi_k\left(\frac{\omega}{\omega_k}\right)} \tag{2.31}$$

Here ω_k is the natural frequency of the system since the presented information is related to a single DOF system. Frequency-independent terms sets the relation between the two previous FRFs to the rest. For example:

$$G_{ii}(\omega) = \frac{1}{k}H_k(\omega).K_{jj}(\omega) \quad = (-\omega^2 m)H_k(\omega). \tag{2.32}$$

Where $1/k$ can be interpreted as the static flexibility and m the static mass of the system. The remaining ones can be found in [48] or be obtained by starting from the equations of motion, assuming $u = Ue^{i\omega t}$, introducing the parameters ω_k and ξ_k, and comparing the equations obtained with (2.30).

Finally, the equations of motion can be written in the frequency domain for the general case of multiple DOFs, using the indexes previously presented. Their matrix form is presented here:

$$\begin{bmatrix} \mathbf{M}_{ii} & \mathbf{M}_{ij} \\ \mathbf{M}_{ji} & \mathbf{M}_{jj} \end{bmatrix} \begin{bmatrix} \ddot{\mathbf{u}}_i \\ \ddot{\mathbf{u}}_j \end{bmatrix} + \begin{bmatrix} \mathbf{C}_{ii} & \mathbf{C}_{ij} \\ \mathbf{C}_{ji} & \mathbf{C}_{jj} \end{bmatrix} \begin{bmatrix} \dot{\mathbf{u}}_i \\ \dot{\mathbf{u}}_j \end{bmatrix} + \begin{bmatrix} \mathbf{K}_{ii} & \mathbf{K}_{ij} \\ \mathbf{K}_{ji} & \mathbf{K}_{jj} \end{bmatrix} \begin{bmatrix} \mathbf{u}_i \\ \mathbf{u}_j \end{bmatrix} = \begin{bmatrix} \mathbf{F}_i \\ \mathbf{F}_j \end{bmatrix} \tag{2.33}$$

In here, components of displacement and its derivative are replaced by vectors and matrix components by matrices, considering every junction and internal DOF. Solving the eigenvalue problem for a k number of DOFs will lead to k natural frequencies. These represent the easiest ways for the system to vibrate in a frequency range and will be a base for the modal approach and modal superposition methods along with the eigenvectors.

2.3.4 The modal approach

The modal approach is a method of solving the equations of motion as in 2.33 by summing the contribution of each mode. It takes two steps: the first is the solution of the equations of motion considering no excitations ($F_i = 0$ and $u_j = 0$), resulting in an eigenvalue problem from where the normal modes are obtained. The next step is to perform the mode superposition.

In the first step, taking F_i and u_j to be zero, one ends up with two sets of second-order differential equations. Their solutions are known, but there are two ways of

solving them. Either by eliminating the damping term and introducing it later or solving it with the damping term, leading to complex modes which are more difficult to deal with and computationally expensive. The first approach is the one used in the FEA solver an is detailed hereafter.

By solving the eigenvalue problem the natural frequencies ω_k and mode shapes ϕ_{ik} are retrieved. These parameters are of the utmost importance for mode superposition as it can be understood to be a "projection of all the physical properties of the structure onto a base of modes ϕ_{ik}"[48]. The next step is to transform the displacements into a base formed by normal modes $\Phi_{(i+j)k}$ and junctions or static modes $\Psi_{(i+j)j}$ by:

$$\begin{bmatrix} \mathbf{u}_i \\ \mathbf{u}_j \end{bmatrix} = \begin{bmatrix} \mathbf{\Phi}_{ik} & \mathbf{\Psi}_{ij} \\ \mathbf{0}_{jk} & \mathbf{I}_{jj} \end{bmatrix} \begin{bmatrix} \mathbf{q}_k \\ \mathbf{u}_j \end{bmatrix} \tag{2.34}$$

where q_k are the modal displacements correspondent to the internal relative displacements $u_i - \Psi_{ij}u_j$. By then applying the transformation to the equations of motions(pre- and post-multiplication), they transform to:

$$\begin{bmatrix} \mathbf{m}_{\mathrm{kk}} & \mathbf{L}_{\mathrm{kj}} \\ \mathbf{L}_{\mathrm{jk}} & \overline{\mathbf{M}}_{\mathrm{jj}} \end{bmatrix} \begin{bmatrix} \ddot{\mathbf{q}}_{\mathrm{k}} \\ \ddot{\mathbf{u}}_{\mathrm{j}} \end{bmatrix} + \begin{bmatrix} \mathbf{c}_{\mathrm{kk}} & \mathbf{0}_{\mathrm{kj}} \\ \mathbf{0}_{\mathrm{jk}} & \mathbf{0}_{\mathrm{jj}} \end{bmatrix} \begin{bmatrix} \dot{\mathbf{q}}_{\mathrm{k}} \\ \dot{\mathbf{u}}_{\mathrm{j}} \end{bmatrix} + \begin{bmatrix} \mathbf{k}_{\mathrm{kk}} & \mathbf{0}_{\mathrm{kj}} \\ \mathbf{0}_{\mathrm{jk}} & \overline{\mathbf{K}}_{\mathrm{jj}} \end{bmatrix} \begin{bmatrix} \mathbf{q}_{\mathrm{k}} \\ \mathbf{u}_{\mathrm{j}} \end{bmatrix} = \begin{bmatrix} \mathbf{\Phi}_{\mathrm{ki}}\mathbf{F}_{\mathrm{i}} \\ \mathbf{\Psi}_{\mathrm{ji}}\mathbf{F}_{\mathrm{i}} + \mathbf{F}_{\mathrm{j}} \end{bmatrix} \tag{2.35}$$

from where two equations can be retrieved:

$$\begin{aligned} &\mathbf{m}_{\mathrm{kk}}\ddot{\mathbf{q}}_{\mathrm{k}} + \mathbf{c}_{\mathrm{kk}}\dot{\mathbf{q}}_{\mathrm{k}} + \mathbf{k}_{\mathrm{kk}}\mathbf{q}_{\mathrm{k}} = \mathbf{\Phi}_{\mathrm{ki}}\mathbf{F}_{\mathrm{i}} - \mathbf{L}_{\mathrm{kj}}\ddot{\mathbf{u}}_{\mathrm{j}} \\ &\mathbf{F}_{\mathrm{j}} = -\mathbf{\Psi}_{\mathrm{ji}}\mathbf{F}_{\mathrm{i}} + \mathbf{L}_{\mathrm{jk}}\ddot{\mathbf{q}}_{\mathrm{k}} + \overline{\mathbf{M}}_{\mathrm{jj}}\ddot{\mathbf{u}}_{\mathrm{j}} + \overline{\mathbf{K}}_{\mathrm{jj}}\mathbf{u}_{\mathrm{j}}. \end{aligned} \tag{2.36}$$

where $\mathbf{m}$, $\mathbf{c}$ and $\mathbf{k}$, with their respective indices, are, respectively, the generalized masses, damping, and stiffnesses of the system, $\mathbf{L}$ are the matrices of participation factors and $\overline{\mathbf{M}}$ and $\overline{\mathbf{K}}$ are the condensed mass and stiffness matrices. The development of all these equations and components can be found in [48]. The above equation allows to solve for $\mathbf{q}_k$ and from this $\mathbf{F}_j$ can also be obtained.

The solution in the frequency domain comes from making the same assumption for q as in u such that it can be represented by $\mathrm{q}(\omega) = \mathrm{q}e^{i\omega t}$, from which results,

$$(-\omega^2 m_k + i\omega c_k + k_k)q_k = \mathbf{\Phi}_{ki}\mathbf{F}_i + \omega^2 \mathbf{L}_{kj}u_j \tag{2.37}$$

where the solution (recalling the expression of the dynamic amplification (2.31)) is:

$$q_k = H_k(\omega)\frac{1}{k_k}(\mathbf{\Phi}_{ki}\mathbf{F}_i + \omega^2 \mathbf{L}_{kj}u_j). \tag{2.38}$$

The sum $\sum \Phi_{ik}q_k$ represents the principle of superposition, as it is the sum of the contribution of each mode to the deformation relative to the junction for a given frequency in the spectrum.

Finally one just needs to do the inverse operation and transform $\mathbf{q}$ back to $\mathbf{u}_i - \mathbf{\Psi_{ij}}\mathbf{u}_j$ and obtain the FRFs from (2.30) and (2.36) transformed back to displacements. The following equations are the modes superposition definition of the FRFs presented before.

$$\mathbf{G}_{\mathrm{ii}}(\omega) = \sum_{\underline{\mathrm{k}}=1}^{\mathrm{N}} \mathrm{H}_{\underline{\mathrm{k}}}(\omega) \frac{\mathbf{\Phi}_{\mathrm{ik}} \mathbf{\Phi}_{\underline{\mathrm{k}}\mathrm{i}}}{\omega_{\underline{\mathrm{k}}}^2 \, \mathrm{m}_{\underline{\mathrm{k}}}} \tag{2.39}$$

$$\mathbf{T}_{\mathrm{ij}}(\omega) = \sum_{\underline{\mathbf{k}}=1}^{\mathrm{N}} \mathrm{T}_{\underline{\mathbf{k}}}(\omega) \frac{\mathbf{\Phi}_{\mathrm{ik}} \mathbf{L}_{\underline{kj}}}{\mathrm{m}_{\underline{\mathbf{k}}}} - \mathbf{M}_{\mathrm{ii}}^{-1} \mathbf{M}_{\mathrm{ij}} \tag{2.40}$$

$$\mathbf{M}_{\mathrm{jj}}(\omega) = \sum_{\underline{\mathbf{k}}=1}^{\mathrm{N}} \mathrm{T}_{\underline{\mathbf{k}}}(\omega) \frac{\mathbf{L}_{\mathrm{j}\underline{\mathbf{k}}} \mathbf{L}_{\underline{kj}}}{\mathrm{m}_{\underline{\mathbf{k}}}} + \mathbf{M}_{\mathrm{jj}} - \mathbf{M}_{\mathrm{ji}} \mathbf{M}_{\mathrm{ii}}^{-1} \mathbf{M}_{\mathrm{ij}} + \frac{\overline{\mathbf{K}}_{\mathrm{jj}}}{-\omega^2} \tag{2.41}$$

2.3.5 Finite element method

The finite element method has been used in the industry worldwide and is particularly efficient in solving problems involving complex physics, geometry, and boundary conditions. The main idea, put in simple terms is to take a complex problem over a domain, discretize (subdivide) that domain and solve simpler problems in the smaller domains. Its advantage over other methods comes from first representing a complex geometrical domain into a series of simpler subdomains, the so-called "finite elements", secondly from solving algebraic equations instead of complicated differential equations over the elements, and third from performing the assembly of all the local solutions to obtain a global one. The basic idea is that any continuous function can be represented by a linear combination of functions ϕ_i and a set of unknown coefficients c_i, from which the set of unknowns u can be approximated in this way where $u \approx \sum c_i \phi_i$ [51].

Starting from a single-element perspective, the displacements u within an element of k nodes may be approximated by the sum of the product of a displacement function (shape function) now represented as $\mathbf{N}$ with the nodal displacements $\mathbf{a}^e$, in vector form:

$$\mathbf{u} \approx \sum_k \mathbf{N}_k \mathbf{a}_k^e = [\mathbf{N}_i, \mathbf{N}_j, \ldots] \begin{Bmatrix} \mathbf{a}_i \\ \mathbf{a}_j \\ \vdots \end{Bmatrix}^e = \mathbf{N}\mathbf{a}^e. \tag{2.42}$$

The strains can then be obtained through the use of a linear differential operator $\mathbf{S}$ so that $\varepsilon \approx \mathbf{S}\mathbf{u}$, which employing the previous equation can be written as:

$$\varepsilon \approx \mathbf{B}\mathbf{a} \tag{2.43}$$

where $\mathbf{B}$ is just the product of S by the shape function vector. With the strains, the stresses can be retrieved employing generalized Hook's law through the matrix

D.

$$\sigma = \mathbf{D}\varepsilon \tag{2.44}$$

and important note is that the stress on a given element may be separated into a product of the **D** matrix with the difference of the current strain value and an initial residual strain and a component of residual stresses, due to manufacturing processes or thermal effects for example. The below Equation represents this relation.

$$\sigma = \mathbf{D}(\varepsilon - \varepsilon_0) + \sigma_0 \tag{2.45}$$

.

Abandoning now the element region and transitioning to the global domain, **u** can be represented by (2.42), but now the shape functions taking only non-zero values if a given node i belongs to the element of concern e. Then employing a variational principle, in this case, the principle of virtual work is used, the sum of the internal and external work may be written, in a general manner, for any virtual displacement δa:

$$-\delta\mathbf{a}^{\mathrm{T}}\mathbf{r} = \int_V \delta\mathbf{u}^{\mathrm{T}}\mathbf{b}\mathrm{d}V + \int_A \delta\mathbf{u}^{\mathrm{T}}\bar{\mathbf{t}}\mathrm{d}A - \int_V \delta\boldsymbol{\varepsilon}^{\mathrm{T}}\boldsymbol{\sigma}\mathrm{d}V \tag{2.46}$$

where, **b** represents the vector of body forces, **t** is the vector of traction forces along the surface and **r** is the vector of external nodal forces. It is possible to write the previous equation in the form:

$$\mathbf{K}\mathbf{a} + \mathbf{f} = \mathbf{r} \tag{2.47}$$

where the stiffness matrix **K**,

$$\mathbf{K} = \int_V \mathbf{B}^{\mathrm{T}}\mathbf{D}\mathbf{B}dV \tag{2.48}$$

and the vector of internal forces

$$\mathbf{f} = -\int_V \mathbf{N}^{\mathrm{T}}\mathbf{b}dV - \int_V \mathbf{N}^{\mathrm{T}}\bar{\mathbf{t}}dA - \int_V \mathbf{B}^{\mathrm{T}}\mathbf{D}\boldsymbol{\varepsilon}_0 dV + \int_V \mathbf{B}^{\mathrm{T}}\boldsymbol{\sigma}_0 dV, \tag{2.49}$$

employing here the separation of stresses in (2.45).

2.3.6 Damping

Damping accounts for dissipative losses on a system and is usually represented by the damping ratio ξ. In a structure composed of multiple DOFs, as seen previously, damping appear in the equations of motion as matrix C and generated the so-called imaginary modes. Another characteristic that difficults their solution is the fact that the eigenvectors do not diagonalize the C matrix, therefore do not uncouple the equations of motion. There are then three hypotheses to apply damping to the

structure, either define a global damping ratio, a Rayleigh type damping of the form $\alpha M_{ii} + \beta K_{ii}$ which uncouples the equations of motion, or define a modal damping ratio ξ_k. In the absence of such information, in an attempt to simplify the analysis and follow the usual procedure a structural damping ratio was defined.

The defined damping can be represented by the damping ratio ξ or the Quality Factor $Q = 1/(2\xi)$. For new structures, the damping ratio is unknown and should therefore be estimated. A lot of factors can influence these values, examples are materials, joints, equipment, and excitation levels. A damping value of 2% was chosen and used in these analyses, this value was recommended by the company's supervisors and represents low-medium damping for conservative purposes [50].

2.4 Structural analysis

Spacecraft and its appendages, like any other structure must handle the loads they are subjected to in a safe manner to guarantee the proper operation of the mission, thus failure is to be avoided at all costs as the price to launch these into space is extremely high. Speaking of launch, it is in this stage of the spacecraft's life that the major and most critical loads are encountered, the rocket is a vibration and acceleration source and these need to be considered in the design. According to [12], the load types to consider in the analysis are quasi-static, more related to the changes in acceleration experienced by the structure, sine or harmonic vibrations, random and acoustic, the focus respectively on the low frequency and high frequency of the spectrum of vibrations encountered, and shock loads from the hard decoupling of rocket parts. On-orbit loads are much smaller and may only be critical to optical equipment, within which micro-vibrations are encountered, usually from thrust firings and momentum wheel bearing rumble. Nevertheless, the structural member should also have enough stiffness, therefore a high enough natural frequency when stowed, to not couple with the rocket's/satellite's natural frequencies and when deployed to avoid attitude control instability and have good optical precision.

In this section, the main phases of a typical spacecraft structural analysis procedure, the requirements set by ESA, and the choice of uncertainty factors will be detailed. A brief explanation of the launch environment encountered after lift-off is presented, highlighting the load types found during that phase to then go through each of the load types, for which an analysis will be performed, explaining their main characteristics and cares to have in each one. The fundamentals of the information presented hereafter are based on ESA's Spacecraft Mechanical Loads Analysis Handbook [50].

2.4.1 The Launch environment

The launch environment i.e. the loads felt by the spacecraft (SC) when inside the launch vehicle (LV) can be harsh on its structure if not well taken into account. The rocket movement through the air generates fluid-structure interaction loads, mechanical loads with its source on the propulsion system and acoustic waves propagate through the structure impacting the SC. In fact, one can divide the load paths into structural and acoustic when vibrations are transmitted through the air for the latter one. Besides quasi-static loads, the majority of the loading has a vibration nature, from which 3 regimes can be identified: A harmonic regime where the excitation is periodic and well defined by a sine with a given frequency and phase, generating a response with the same frequency (higher harmonics can also be excited is they are multiples of the system's natural frequency) and a phase lag. These types of events are rare as the nature of the loads in this context is transient, but when present they can couple to the structure modes and lead to high responses which can be critical for the structure. It is important to emphasize that, although harmonic loads seldom appear, a sine equivalent analysis is very common to be performed, which takes into account low-frequency transients in an equivalent way. Secondly, a transient regime encompassing all the load's experience in real-world rocket flight but ESA restricts this notion to relatively short excitation as in pyrotechnic events lasting milliseconds up to transient thrust loads of tenth of seconds durations. Thirdly, a random regime, where deterministic analysis does not apply, an example being a car going through a given road with natural defects and bumps leading to a random motion of the car's suspension. These types of analysis, as will be explained later recur to statistics to get a probability of encountering a given response at a point.

In order to guarantee proper operation when in orbit, the satellite and its appendages must survive the journey into LEO. The LV trip into orbit can be divided into different phases and each phase poses different load inputs to its structure and its payload. Figure 2.18 greatly illustrates the loads found throughout the flight and will help in their differentiation.

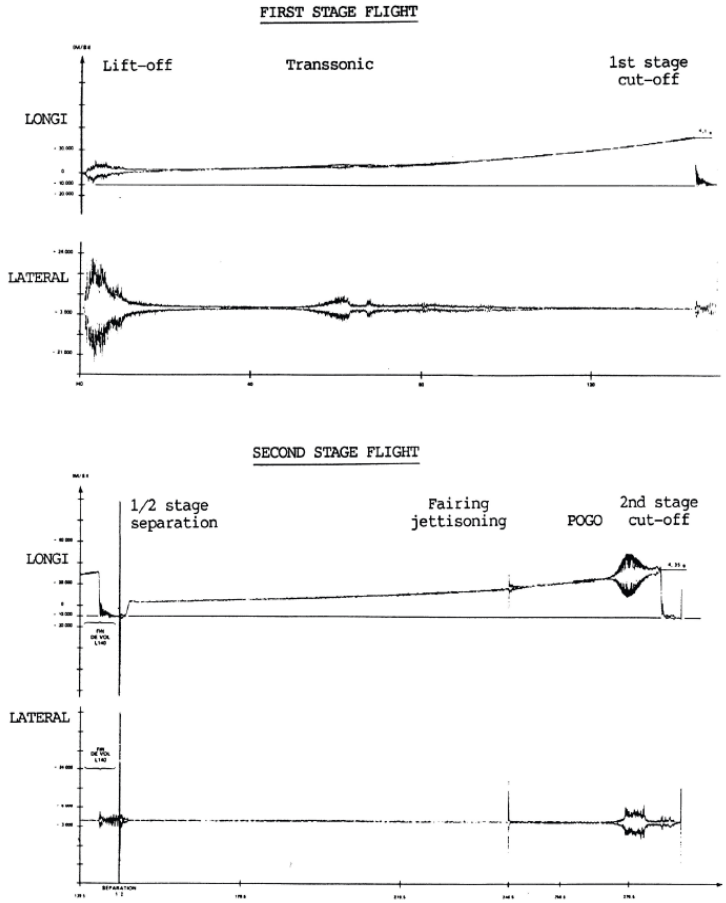

Figure 2.18: Ariane 5 flight load spectrum. Taken from [50]

In this picture and according to the main reference of this section, 4 regimes can be encountered throughout the flight:

- A quasi-static, well characterized by the slow increase in longitudinal acceleration more pronounced in the first flight phase. It is caused by loss of fuel mass and, in simply put, a constant thrust that by Newton's second law results in an increase in acceleration;
- A harmonic regime well seen at the end of the second flight stage caused by the POGO effect, PrOpulsion Generated Oscillations that also refers to the jumping toy named pogo as the effect is characterized by high longitudinal vibrations resultant from engine thrust oscillations. The POGO displays a sweep through a frequency range and in a normal flight is suppressed.
- A transient regime, as referred to before comprises therefore transients and shock events, in this case, separation shocks caused by pyrotechnics, Marmon clamps (a separation device), or other separation actuators.
- A random regime encountered at lift-off and transonic flight whose frequencies

can go up to 2000 Hz with varying magnitudes discarding the deterministic treatment of such loads.

2.4.2 Coupled loads Analysis

The coupled loads analysis, although not being performed in the present work due to the fact that this analysis requires a model of the spacecraft which is not present at the moment, is an essential step in spacecraft design. In sum, a prediction of the loads impacting the rocket, as the ones discussed before, is followed by a coupling between the spacecraft and the launch vehicle models. In this way, a simulation can be performed to access the loads at the LV/SC interface. A model of the rocket is connected as representative of reality as possible to a model of the spacecraft, the loads are computed and then load envelopes can be obtained. The analysis recurs to reduction techniques such as the Craig-Bampton method, which reduce the number of equations to be solved, something very useful for these problem scales. From this point on the analyses can be conducted solely on the SC model. In a further point of the design, these analyses may be re-done, this time between the SC and its appendages, to size these components.

2.4.3 Quasi-Static Analysis

Static loads are well-defined in the engineering world and are loads with no dynamic component or no time domain. Its effects on structures can be easily computed by analytical or numerical methods such as the finite element method. In the preliminary design of a spacecraft and its components, the designers consider equivalent static loads obtained from a combination of dynamic and static inputs. These are termed quasi-static loads (QSL) and they represent an envelope of the COG accelerations, therefore specifying the most severe combined accelerations during the mission. QSL are normally given in terms of load factors.

2.4.3.1 Load specification

The QSL values are normally computed by coupled load analysis or are given in the launcher's user manual. For the given case the launch vehicles that are supposed to carry the satellite into orbit are the Vega or the Falcon 9 from which one can retrieve the QSL in the longitudinal and lateral directions. For this project the most severe values will be chosen to maintain a conservative philosophy, therefore the Vega was selected and the QS values are reported below.

Table 2.4: Vega Quasi-Static loads [52]

Load Event		QSL (g) (+ = tension ; - = compression)		
		Longitudinal		Lateral
		Compression	Tension	
1	Lift-off phase	-4.5	+3.0	±0.9
2	Flight with maximum dynamic pressure (Q_{max})	-3.0	N/A	±0.9
3	1st stage flight with maximal acceleration and tail off	-5.0	N/A	±0.7
4	2nd stage ignition and flight, 3rd stage ignition	-5.0	+3.0	±0.7
5	3rd stage maximal acceleration	-7.0 + M (1) / 1000	N/A	±0.2
6	AVUM flight	-1.0	+0.5	±0.7

(1) *M : mass [kg] of the spacecraft*

Some caution should be taken with the use of these loads. Although they are well suited for preliminary sizing, they are normally not high enough to account for the effects of transient loads on secondary and tertiary structures as in the case of appendages. Also, QSL from the user's manual of the launcher may not be adequate to size primary structures when local modes or out-of-phase motion is present. Finally, these loads are applied to the spacecraft COG, not appendages, as a really rough approximation it will be assumed that the accelerations can be applied to the panels. This is correct in a way that these accelerations will be felt by the antennae but they are not the QS loads on the antennae. QS are not real accelerations created by the spacecraft and are rather the maximum accelerations of a combination of static and dynamic events on the antennae.

2.4.3.2 Mass acceleration curves

MACs (mass acceleration curves) are commonly used for the preliminary design of spacecraft hardware and equipment. These are constructed based on data from prior flights and tests, experience, and analysis and they represent an upper acceleration for all components of a specific mass regardless of its position on the structure or the frequencies it is exposed to during the flight. It also clearly displays the relation between mass and acceleration as a component with less mass subjected to a given load at its interface will have a higher acceleration. They also include responses from random and transient events. A mass acceleration curve will be used as a second QS load case in the final model if the Vega quasi-static loads are not conservative and for the given case, assuming an initial mass of 4kg as will be shown later, it is possible to obtain an acceleration of 40g. In the absence of a company-derived one through flight heritage and experience the one in [53] will be used if the Quasi-static input is not conservative enough.

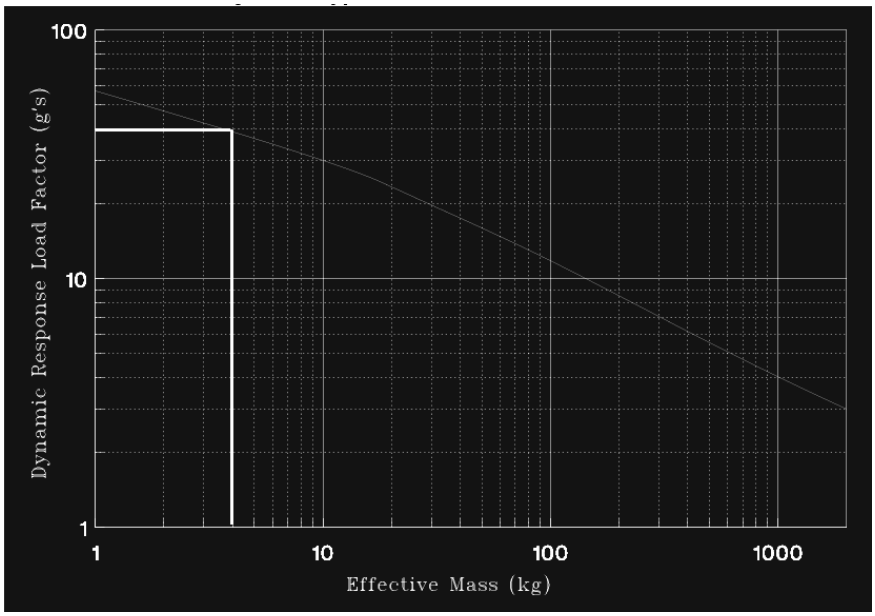

Figure 2.19: Typical mass acceleration curve. Taken from [53]

2.4.4 Modal analysis

Before starting to speak about the dynamic analysis previously discussed, there is a common pre-requisite for both harmonic and random analysis. There are two main ways of solving the equations of motion, either by the "full-method" (ANSYS name for the analysis was adopted) or by modal superposition. The first evolves numerical methods and discretization of the time domain, employing techniques such as the Newmark method, the second was explained in section 2.3.4. Thus before the above analyses, the natural modes of the structure need to be found. The number of modes depends on the frequency range. ANSYS documentation advises using 1.5 times the upper limit of the frequency range as the upper limit for frequency search. That means that in the case of harmonics, the range going up to 100 Hz, modes up to 150 Hz should be retrieved. On the other hand for random excitation with a frequency range up to 2000 Hz, the search range should go as high as 3000 Hz. This procedure was adopted throughout the analyses.

2.4.5 Harmonic Response Analysis

Sinusoidal excitation is a vibration of harmonic nature ranging up to 100 Hz. They can be transmitted to the spacecraft by dynamic coupling. The level of the response is dependent not only on the coupling between the LV/SC but also on the interface. In the low-frequency qualification process, the sine test plays an important role in the global qualification of the spacecraft in the low-frequency regime, qualification of secondary structures to the sine environment, and verification of stiffness requirements.

2.4.5.1 Sine loads

Although some near harmonic loads may be transmitted through the structure, the sine vibration analysis usually performed is not representative of the real loads, rather, it is a sine equivalent input excitation. The loads felt inside the rocket are of transient nature, the input spectrum is used to envelop the complex low-frequency transient loads without the need for a transient analysis [12]. The harmonic input spectrum from the spacecraft can be found in launcher's user manual. As mentioned before the Vega launcher, being the one with the strongest spectrum is therefore the most conservative, and its respective sine environment is shown below.

Table 2.5: Vega sine environment. Taken from [52]

Direction	Frequency Band (Hz)			
	1 – 5	5 – 45	45 – 110	110 – 125
	Sine Amplitude (g)			
Longitudinal	0.4	0.8	1.0	0.2
Lateral	0.4	0.5	0.5	0.2

The issue with this spectrum is that it envelops the low-frequency transient loads felt by the spacecraft, not its appendages. Due to their low mass, higher accelerations will be felt and thus a harder load specification will be present. An example is shown below for appendages below 100 Kg. This will help to overcome the problem of not having a satellite model to perform a coupled loads analysis and retrieve the sine spectrum from there.

Table 2.6: Sine environment for appendages. Taken from [50]

Axis	Frequency (Hz)	Qualification	Acceptance
Out of plane	5 - 20	15 mm	9.9 mm
	20 - 100	24 g	16 g
In plane	5 - 20	9.9 mm	6.6 mm
	20 - 100	16 g	10.7 g
Sweep rate		2 Oct/min 1 sweep up	4 Oct/min 1 sweep up

As advised by the company's supervisors and as referred in [12], to avoid coupling and extreme responses by the component to this input, its first natural frequency should be above 100 Hz.

2.4.6 Random Vibration analysis

Random vibration analysis is responsible for accessing the structural response to nondeterministic excitations, i.e. varying magnitude spectrum with frequencies

under a given range that do not follow any predetermined behavior and are of statistical nature. Examples of sources of these types of loads are, for example, oscillations in the car suspension when moving, or more related to the space field, engine thrust oscillations, aerodynamic buffeting, and sound pressure on payload surfaces.

The definition of a Random process as by [48] is that a phenomenon x is considered random if it does not display periodicity in time nor is repetitive, i.e. no two phenomena at different times are equal. Considering now the autocorrelation of x as defined below in the time domain and in a statistical manner,

$$\begin{aligned} R_{xx} &= \frac{1}{T}\int_0^T x(t)x(t+\tau)dt \\ R_{xx} &= \int_{-\infty}^{+\infty}\int_{-\infty}^{+\infty} x_1 x_2 p(x_1)p(x_2)dx_1 dx_2 \end{aligned} \tag{2.50}$$

where p is a function of the probability of a normal distribution, x_1 and x_2 are values of x at two different times that, multiplied by the probability and integrating over infinity one has an equivalence to a mean value. The autocorrelation is nothing more than the mean of the product of x at two-time instances.

The random input and output are normally represented by a power spectral density or PSD, which is the Fourier transform of the autocorrelation,

$$S_{xx}(\omega) = \int_{-\infty}^{+\infty} R_{xx}(\tau)e^{i\omega t}. \tag{2.51}$$

Taking the inverse Fourier to transform, considering the first equation in Eq. (2.50) and accepting that

$$R_{xx} = \overline{x}^2$$

one can reach the following,

$$\overline{x}^2 = \int_{-\infty}^{+\infty} S_{xx}(\omega)d\omega \tag{2.52}$$

from this, having an engineering perspective, discarding the negative domain of the integral and passing from radians frequency to hertz frequency one can finally obtain:

$$\overline{x}^2 = \int_0^{+\infty} W_{xx}(f)df. \tag{2.53}$$

By taking the square root, one can retrieve the commonly used root-mean-square of the PSD that, if expressed in Gs (standard Earth gravity) corresponds to the well know G_{rms}.

Random vibrations are represented by Power Spectral Density (PSD) plot curves in a log-log scale ranging from 20 to 2000 Hz. The term power is a generic term that may represent displacements and their derivatives as well as forces and stresses. In fact, the PSD represents the energy distribution over the frequency range. An example of a PSD input spectrum, and in fact the one to be used is presented in Figure 2.20.

2.4.6.1 Random vibration loads specification

To perform any analysis one important step is to obtain the loads applied on the structure. The steps to obtain the random vibration loading spectrum are the following:

- Obtain the PSD of the random vibrations transmitted from the LV to the payload through its mountings.
- Analysis for response retrieval. For high frequency, Statistical Energy Analysis (SEA) methods are recommended whereas for random vibration (lower frequencies) FEA is commonly used.
- Enveloping the curves from the previous points to get the accelerations for the component

The loads or accelerations resulting from this process are used at the flight acceptance test level. For qualification and protoflight levels, the test power is increased by 3dB. Just as a note, rigid fixture RVT (random vibration tests) may overtest the component since in the real load environment, mode absorption, also called impedance effects, may occur and the interface may not be as rigid as assumed, as previously discussed. Notching is therefore recommended.

The random vibration input spectrum for units coupled to the spacecraft is normally obtained by either retrieving the response of the spacecraft at the zone of interest when subjected to a random input (usually found in the LV user manual or given to the analysis engineer directly) at its connections to the LV or by computing the random vibration loads generated by an acoustic PSD given in the launcher user manual is the structure to be studied is known to be particularly sensitive to these excitations such as big panel arrays. Both models present some difficulties for the present work. The first would require the satellite model or the loads which are not present. The second would involve higher-end analysis like BEA/FEA coupling or stochastic methods for higher frequencies, and a more detailed model as reported in Section 9 of [50]. Although these 2 methods were not employed, a summary of them can be found in Appendix B.2

There are some alternatives to estimate random excitations on components prior

to obtaining or in the absence of this information. In the reference document, four methods are described:

1. Spann method - Gives a fair estimation of the vibration environment when only having information about the exposed areas and the mass of the structure. In sum calculates a PSD from a random acoustic spectrum then multiplies the pressure PSD by the wetted area and divides by the mass of the structure to obtain an acceleration;
2. Specifications derived from test campaigns data with 95% confidence;
3. The VibroSpec method - need of specialized software;
4. Test/analysis extrapolation method - validate FE model results with test results with lower intensity to then scale to flight test levels and simulate the test

A random vibration specification for units under 50 kg based on a number of empirical curves taken from past experiments was used (point 2). The load specification is shown in Figure 2.7.

Table 2.7: Random vibration specification for units under 50kg. Taken from [50]

Vertical (2)	
Frequency (Hz)	PSD (g^2/Hz), Mass equipment M (kg)
20-100	6dB/octave
100-400	0.05*(M+20)/(M+1)
400-2000	-3dB/octave
Lateral (3)	
Frequency (Hz)	PSD (g^2/Hz), Mass unit M (kg)
20-100	6dB/octave
100-200	0.05*(M+20)/(M+1)
200-2000	-4dB/octave

The estimated mass of the structure is still unknown but from the FEM model, it is possible to estimate it to be around 4 kg. Following Table 2.7 the input PSD was calculated and plotted in Matlab as shown in Figure 2.20.

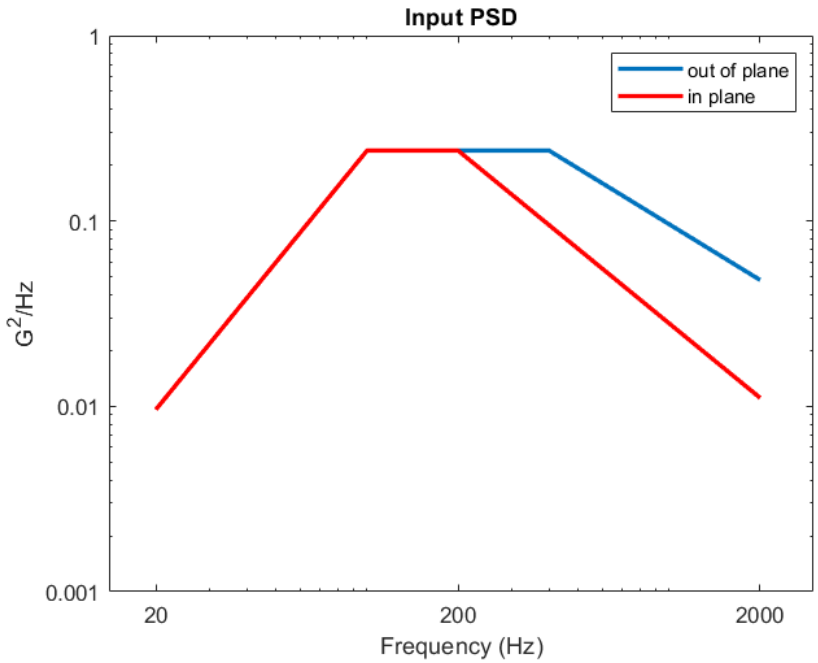

Figure 2.20: Input PSD - Calculated from ESA's Structural Analysis handbook

Now discussing finite element analysis, the main objective of the RVA is to determine the frequency transfer function of the structure $H(f)$ which represents the input load path at the point of interest. The step-by-step procedure to obtain $H(f)$ will now be discussed as it is presented by ESA:

1. Start from the finite element model and perform model checks. The model should represent well the structure in terms of mass and stiffness and, proper loads and BCs should be applied

2. Perform modal analysis and obtain natural frequencies, mode shapes and effective masses

3. Define the damping by modal damping ratio or another method

4. Perform modal analysis on the uncoupled system of equations in generalized coordinates $\{\eta_k\}$

$$\ddot{\eta}_k + 2\xi\dot{\eta}_k + \omega_k^2\eta_k = \frac{\{\phi\}^T}{m_k}(F) \tag{2.54}$$

5. The displacement vector in the frequency domain becomes:

$$\{x\} = \sum_{k=1}^{n} \frac{\{\phi\}\{\phi\}^T}{(\omega_k^2 - \omega^2 + 2i\xi\omega\omega_k)m_k} \cdot (F) \tag{2.55}$$

where (F) is the force vector, ϕ is the mode shape of mode k, ω_k is a natural frequency of the system and ω is the frequency of study, making $\{x\}$ function

of the frequency. If F is a unit force vector then the relation above inside the sum represents the transfer function $H(\omega)$

6. Considering the static case, the above relation can be written as:

$$\{x\} = \sum_{k=1}^{n} \frac{\{\phi\}\{\phi\}^T}{\omega_k^2 m_k} \cdot (F) \tag{2.56}$$

It can be seen that the sum represents the compliance of the system $G(\omega)$.

7. Finally the response PSD can be obtained by:

$$W_{out}(\omega) = |H(\omega)|^2 W_{in} \tag{2.57}$$

2.5 Factors of safety

To add a margin of safety to the analysis and test, factors of safety accounting for uncertainties in the calculations are used. These uncertainties may come from load calculations, load applications in the model, the definition of boundary conditions, project maturity, material properties, and many others. In the present work the factor of safety philosophy presented by ESA in [50] and [54] is used.

The factor of the safety tree to follow is presented in Figure 2.21. The adopted route is the middle one. Starting from the limit loads, by multiplying it by a coefficient A, which will be defined later, one can retrieve the design limit load, which takes into account uncertainties related to the project maturity, the test level, and the accuracy of the model. Then the route bifurcates into design yield load (DYL) and design ultimate load (DUL) with their respective coefficients of safety where these are dependent on whether the load simulation is done by tests or analyses. The coefficient is thus obtained by the product of a set of factors and is defined in Table 2.8. The factors used in space projects are related to a given uncertainty and are the following:

- K_M, model factor - Model maturity and ability to represent reality
- K_{LD}, local design factor - Model local discontinuities
- K_P, project factor - Maturity of the project and its design
- K_A/K_Q test factors - Type of test, acceptance or qualification respectively
- FOSY, Yield design factor of safety - Multiplies with the DLL to obtain the DYL, varies with material and verification (test or analysis) types
- FOSU, Ultimate design factor of safety - Multiplies with the DLL to obtain the DUL, varies with material and verification (test or analysis) types

Values from these factors can be obtained from the standard or from other projects. The values used are shown in Table 2.9 plus the respective coefficients calculated and total safety factors (TSF) in Table 2.10.

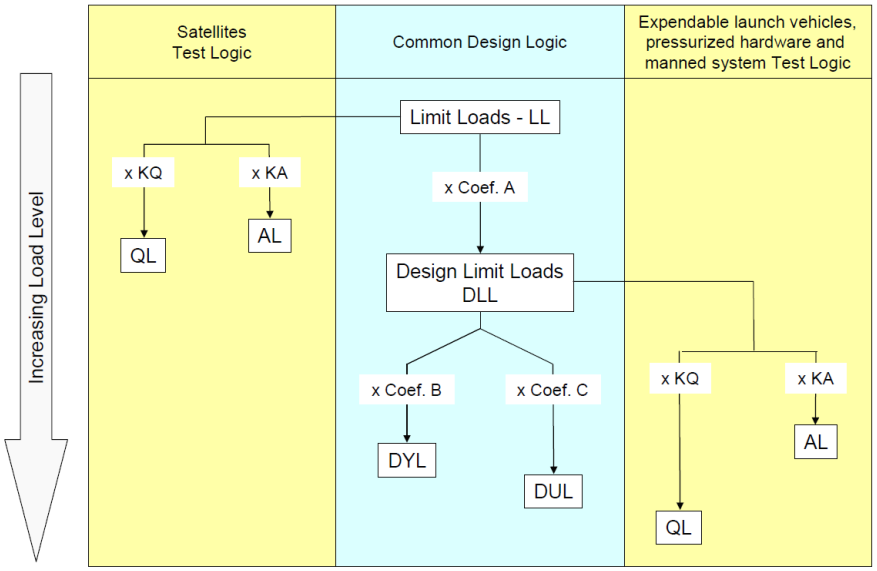

Figure 2.21: Factor of safety tree. Taken from [54]

Table 2.8: Factors of safety coefficients. Taken from [54]

Coefficient	Satellite	Launch vehicles and pressurised hardware	Man-rated systems
Coef A or Design factor	KQ x KP x KM	KP x KM	KP x KM
Coef B	FOSY x KLD	FOSY x KMP x KLD	FOSY x KLD
Coef C	FOSU x KLD	FOSU x KMP x KLD	FOSU x KLD

Table 2.9: Safety factor values. Values taken from [54, 55]

Factor	Value
K_M	1.2
K_P	1.1
K_Q	1.25
K_{LD}	1.2
$FOSY$ (Metal)	1.25
$FOSU$ (Metal)	2
$FOSU$ (FRP)	2

Table 2.10: Calculated coefficients and total safety factors

Coefficient	Value
Coef. A	1.65
Coef. B (Metal)	1.5
Coef. C	2.4
DYL total factor	2.475
DUL total factor	3.96

In this case, coefficient C is common if the material is a metal or a fiber-reinforced polymer like the material of the SAR plates. Coefficient does not apply to FRP material as it does not "yield", the ultimate stress corresponds to the failure of the laminate.

Finally, the margin of safety can be calculated by:

$$MOS = \frac{\sigma_{allowable}}{Total factor \cdot \sigma_{LL}} - 1. \tag{2.58}$$

If the margin of safety is positive then the structure can sustain the loads.

2.6 Materials

The selection of materials is paramount to guarantee that the structure's life and strength are enough to sustain the mission. Their impact doesn't restrain itself to mechanical properties, it affects costs (even more in space applications), manufacturing, and design choices.

More than 120 000 different materials can be used for aerospace structure construction. Although the variety is encouraging, the presence of the majority of key properties in a single material is rare and thus the number of effective materials is greatly reduced. Important properties to be present in aerospace materials essential to aircraft include their physical properties, mechanical properties, chemical properties (corrosion, oxidation, outgassing), thermal properties, and electrical properties. Having this said, aerospace materials must be light, have good rigidity, be strong, be damage tolerant, and be durable [56].

The main materials used in such applications are aluminum alloys, titanium alloys, steels, and composites. Other materials can be found in more specific applications. A comparison between them is presented in the Table below.

Table 2.11: Comparison of aerospace materials based on most important design features. Taken from [56]

Property	Aluminium	Titanium	Magnesium	High-strength steel	Nickel superalloy	Carbon fibre composite
Cost	Cheap	Expensive	Medium	Medium	Expensive	Expensive
Weight (density)	Light	Medium	Very light	Heavy	Heavy	Very light
Stiffness (elastic modulus)	Low/medium	Medium	Low	Very high	Medium	High
Strength (yield stress)	Medium	Medium/high	Low	Very high	Medium	High
Fracture toughness	Medium	High	Low/medium	Low/medium	Medium	Low
Fatigue	Low/medium	High	Low	Medium/high	Medium	High
Corrosion resistance	Medium	High	Low	Low/medium	High	Very high
High-temperature creep strength	Low	Medium	Low	High	Very high	Low
Ease of recycling	High	Medium	Medium	High	Medium	Very low

The main materials to be used in this work will mainly be aluminum alloys for the main structure and a PCB-like material which is a composite material as will be explained onwards.

2.6.1 Metallic materials

Aluminum alloys have a long aerospace heritage of over 40 years, the main alloying families used are the 2xxx, 6xxx, and 7xxx. All belong to the age hardenable alloys group changing only the main alloying element and their respective properties. Copper in the 2000 series, Magnesium and Silicon in the 6000s, and Zinc in the 7000s. Aluminum-Lithium alloys are also interesting since the addition of lithium to the alloy composition leads to a decrease in density and an increase in strength, [57]. The attractiveness of aluminum alloys comes from their low cost, lightweight, heat treatable to fairly medium-to-high level strengths, ease of fabrication, high specific stiffness and strength, ductility, fracture toughness and fatigue resistance, and good control of properties. Disadvantages include low modulus of elasticity, loss of properties at elevated temperatures (above around 150°C), susceptibility to stress corrosion cracking, difficulty in welding of age hardenable alloys, and corrosion when in contact with carbon fiber [56, 58]. The properties of possible aluminum alloys are found below.

Table 2.12: Aluminum alloy properties. Obtained from [59–62]

Property	AA 2024-T3	AA 7075-T6	AA 6061-T6	AA 6082 - T6
E [GPa]	72.5	71.0	68.3	72
ν [-]	0.33	0.33	0.33	0.33
YTS [MPa]	289.6	468.8	241.3	240-300
UTS [MPa]	434.4	537.8	289.6	280-330

A density of 2700 $kg \cdot m^{-3}$ is considered. The first three are commonly used aluminum alloys, while the last one is an alloy the company uses, therefore having priority over the others. It is a medium-strength alloy, the strongest in the 6000

family due to the addition of large amounts of manganese that controls the grain structure resulting in a stronger alloy. It also displays excellent corrosion resistance, which is important in space applications [60].

2.6.2 SAR plates material

The SAR antennae material is the RO4003C from Rogers Corporation, it is a hydrocarbon ceramic laminate made mainly out of FR-4 Glass fiber, a fire-resistant (FR) grass fiber laminate usually present in printed circuit boards (PCBs). Outgassing properties are good and space grade, standard testing revealed a mass loss of only 0.06% of which one-third was water [63]. The material was considered orthotropic. Orthotropic materials have 9 independent material properties, 3 Young moduli E_x, E_y, E_z, 3 Poisson's ratios $\nu_{xy}, \nu_{yz}, \nu_{zx}$ and 3 shear moduli G_{xy}, G_{yz}, G_{zx}. Few properties can be found in the supplier's Datasheet [63].

As will be seen later the material was defined as orthotropic in ANSYS Workbench, thus the Young modulus in X and Y, the only material properties reported in the datasheet, were not enough. Due to the lack of material properties, some research was performed to try to obtain more of these properties from the plate's main components, thus assumptions were made. The first assumption was to use an older material database for the same material to get the Young's Modulus in Z (out-of-plane direction), the assumption relies on the fact that reported material properties are different for the same material, possibly indicating that material upgrades were done through the years. The second assumption was that, in the absence of all Poisson's ratios and shear moduli, the properties of its main constituent, FR-4, were used. Material properties used can be found in the 1080 FR-4 laminate table from [64]. Poisson's ratios are taken from [65]. Although the latter gives all orthotropic material properties a great disparity of values was found between the article and since [64] gives values of a type of FR-4 used in the SAR plates as reported by the manufacturer, the other elastic properties were not considered.

A sensitivity study was performed on each material property, based on the paper containing the material properties where each value was changed and the difference in results observed. This is supported by the fact that material properties are taken from different references. In [64], an experimental campaign is undergone to obtain the natural frequencies in free edge configuration and properties of laminated FR-4 90X120 mm plates. The model was rebuilt in ANSYS using the same material properties and dimensions. The comparison between the obtained modes and the modes on the paper is shown below.

Table 2.13: Article SAR plate mode comparison with constructed FEM model

Article [64]	ANSYS	Relative Difference [%]
139.13	138.74	0.28
258.83	262.29	1.34
373.03	385.8	3.42
467.07	465.55	0.33
539.02	539.74	0.13
714.06	734.6	2.88
774.07	785.74	1.51
823.08	842.52	2.36

As can be seen, the frequencies match well so the sensitivity study was performed. After varying each material property by a given amount and if necessary more to check for differences it was found that the plate, as well as the ones to be used in this work's model, showed almost no difference when changing out of plane properties, revealing a plane orthotropic behavior. Concerning in-plane properties, E_x and E_y were not changed since they come from the manufacturer data sheet, the Poisson's ratio did not affect the frequency much after changing the initial value of 0.11 to 0.2 and 0.33. The major difference was found in the shear modulus G_{xy} that when changing its initial values from 2.46 GPa to 5 GPa, a relative difference of almost 40% was found leading to 50Hz increase in first natural frequency. Having this said in future works, good material properties should be asked from the manufacturer to avoid big analysis errors. The final material properties of the SAR plates are shown below.

Table 2.14: SAR plate's RO4003C material properties

E_x [GPa]	E_y [GPa]	E_z [GPa]	ν_{xy} [-]	ν_{yz} [-]	ν_{zx} [-]	G_{xy} [GPa]	G_{yz} [GPa]	G_{zx} [GPa]
19.65	19.45	5.8	0.11	0.39	0.39	2.46	1.6	1.8

Chapter 3

Geometry design

To accomplish the objective of having a deployable mechanism for the opening of SAR antenna panels in space, CAD models were built using Solidworks to better grasp the form and elements included in its structure and also have a 3D view of the model to check for problems that would happen in reality like spacing, contact zones, and travel limits. In the context of this thesis, it was proposed that such models would be built to aid the company in the design of a future deployable for an in-orbit demonstrator. The present chapter will present the design of two mechanisms. Along with the geometric concepts will be the underlying design ideas and considerations taken. Finally, both designs will be weighted with the company's interest to choose one to use in the structural analysis.

3.1 Inspiration, considerations, and requirements

The mechanism to be designed is, as referred to before, a deployable mechanism capable of opening at least four panels. The larger the aperture the better for the team, as it is able to obtain higher-resolution images. Therefore the objective is to maximize the number of plates, while at the same time keeping the weight to a minimum. The requirements for the mechanisms are presented below:

- Low mass - a specific threshold was not defined but rather the satellite mass budget will take into account the needed weight of the array. So although a limit is not present, the objective is to minimize the mass
- Space restriction - the mechanism will be inside a 400×400×400 [mm] box
- Larger aperture possible considering space and mass restrictions
- Ability to return to the stowed position - retractable

- First deployed natural frequency >1 Hz
- Flatness
- First stowed natural frequency above 100 Hz (only defined later in the structural analysis)
- Low number of possible failure points
- Strive for simplicity in the mechanism to keep the number of parts and weight to a minimum
- Synchronized deployment - Due to the limits in space it would be advantageous to have the deployment following a straight trajectory out of the satellite's interior

As presented in the literature review, the techniques for deployment are many, each with its pros and cons for a given application. The two main foundations behind the concepts presented here onward were those of motorization and synchronization. The former is encouraged by the need for the mechanism to alternate between stowed and deployed positions. The latter is due to space restrictions since, as will be shown, the panels have dimensions of 300×300, thus leaving only 50mm on each side for oscillations in the movements in its free deployment. The two conceived solutions were then, a pantographic mechanism and an elastic hinge-driven, motor-controlled, closed cable loop synchronized mechanism.

3.2 Model 1 - Pantograph

The pantographic mechanism is a well know mechanism present in people's everyday life and may be better known to people from its use in gates, wall mounted small mirrors, but its origins come from drawing as it can scale a drawing by placing a pen on the tip and on the middle of the mechanism as depicted in the figure 3.1. Due to its kinematics the motion in the middle is half of that on its tip, for a normal pantograph.

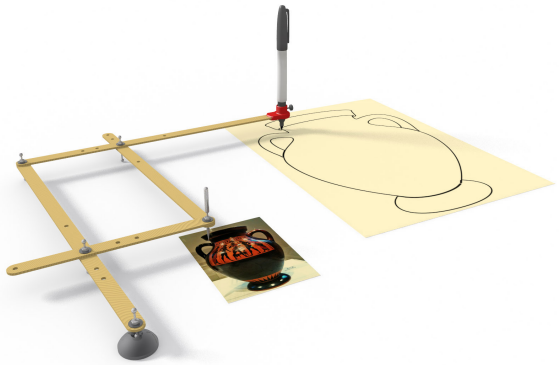

Figure 3.1: Pantograph mechanism example

The benefits of the mechanism are its simplicity and inherent synchronization. It is composed of two cross bars that rotate relative to each other at the center and, by coupling a repeated array of such cross-like elements one can propagate the opening and closure of the bars resulting in an ascending and descending motion. One panel will be coupled to one set of opposing bars, repeating the process upwards. The movement is guided at the lowest bars, one remains fixed while the other is pushed forwards or backward by a lead screw connected to a traveling nut-like piece. In Figure 3.2 one can see the stowed configuration of the mechanism.

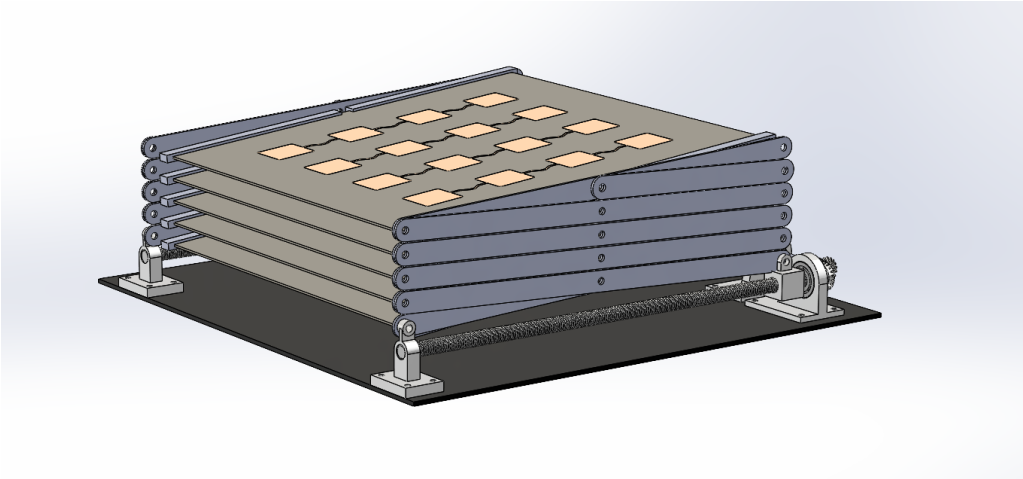

Figure 3.2: Pantograph mechanism stowed

Near the bottom plate, two supports on each side will allow the drive screw to rotate and push the slider of Figure 3.4. The SAR panels are secured to the lateral bar by being pushed into some slots carved on the bars. Speaking of such slots, they are slightly inclined relative to the bars. This allows simplifying the design, since at the end of the travel the pieces may touch together not allowing for a perfect extension of the mechanism, while still guaranteeing the plenitude of the panels. Also, as reported in [32], leaving a small angle between the bars at full deployment leads to an increase in first natural frequency, even founding a 7.5× increase for a 5°.

The mechanism synchronization is guaranteed by a gear assembly, Figure 3.3. The motor sits below the panels, and if space is not enough the whole structure can be positioned slightly higher and the motor sitting at a lower level. The motor is coupled to a main gear that transmits the motion to the main axle. This motion is transferred to the lead screws, in a synchronous way, by the 90° bevel gear that allows for this right-corner transmission. The gears' assembly can be seen below for a better understanding.

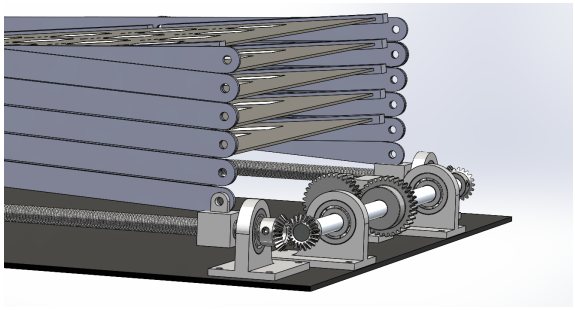

Figure 3.3: Gearing and synchronizing axle

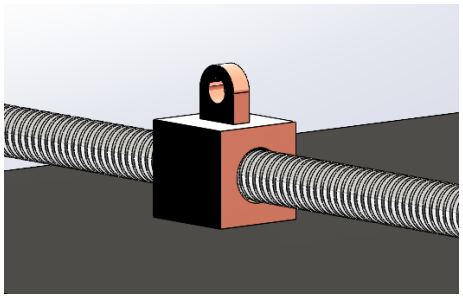

Figure 3.4: Travelling nut

In figure 3.5, one can see how the mechanism does the deployment, showing how the movement of the bottom bars drives the rest, with all the panels opening at the same rate. Under it, in figure 3.6, is a picture showing how the mechanism looks when fully deployed showing how the panels retain their plenitude in the array while the bars are at an angle.

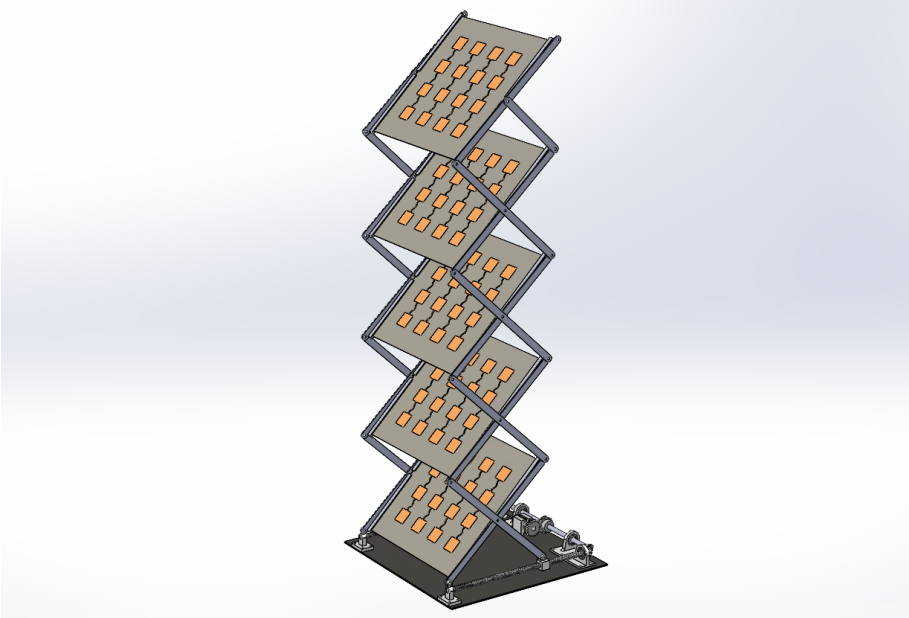

Figure 3.5: Pantograph mechanism travelling

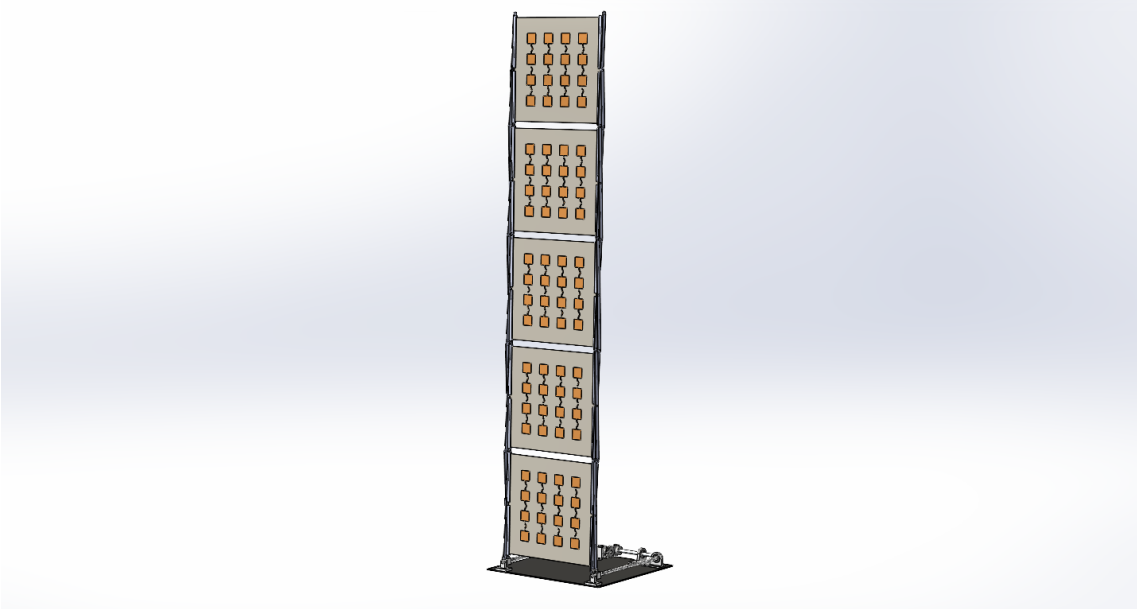

Figure 3.6: Pantograph mechanism deployed

3.2.1 Discussion

Some final considerations were drawn about the presented mechanism. It presents a simple solution, without many moving pieces near, with self-synchronization, excellent deployment control, retractable and light. Apart from its positive side, it may cause some serious problems. After some discussion with the experienced engineering team at the company, the mechanism's major problem is related to how well it reacts to temperature differences. The plates are connected to the bars through

small areas and they are not made to conduct heat, plus, even if some coating is introduced the risk of warping is high. Since there is a high number of mechanical linkages connected to each other, if some have a higher thermal expansion than others the mechanism will probably not be able to deploy.

3.3 Model 2 - Closed cable loop

The second model is based on a commonly used principle of deployment: stored elastic energy. The idea in the model was to connect the panels to some lateral bars to add rigidity and increase the deployed first natural frequency. Then hinges would connect the lateral beams, equipped with torsion springs to drive the deployment and latches to lock the panels in place at the end of the movement. The closed cable loop idea exposed in Section 2.2.1 transfers the excess torque from hinge to hinge synchronizing the movement. By connecting a base pulley to one connected to the root or connecting a cable to the panels' tip, the deployment movement can be controlled using an electric motor acting as an eddy current damper or applying a resisting pulling force. For the use of the motor as an eddy current damper, in [46] it recommends using a small gearbox attached to the motor, which is commercially available, to increase the damping effect.

The design of the model started from rough sketches, increasing detail over time. Although not a final design or a final product, with all the needed detail, it represents well the wanted mechanism and is presented hereafter. In the model, a base is shown to represent the connection to the satellite. An electric motor box where the motor would be mounted contains large enough holes to avoid it turning into a pressure vessel during ascendance. The motor is connected to the base of the rotation of the panel through a timing belt. The edge of the lower panel can rotate around an axis parallel to the base. The rest of the panels are connected by hinges as described before. The pulleys are connected to the lateral bars and their axis is aligned with the hinges ones. Connecting the pulleys are steel ropes (not represented) that should have some type of tension-regulator device to account for the thermal expansion of the cable, the use of springs is recommended in [27]. With sliding surfaces, it was advised by the company to use different materials in sliding surfaces or promote lubrication between parts, to avoid cold welding.

The stowed configuration is shown in 3.7. The light color elements connected to the bars are spacers to guarantee contact between panels.

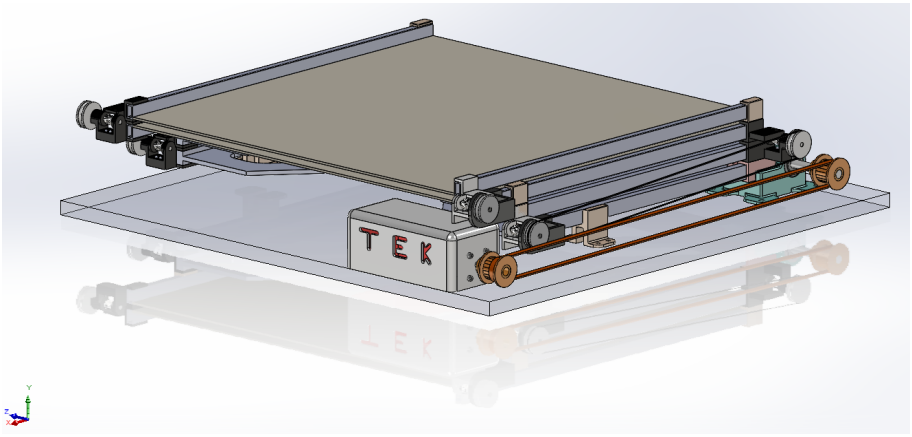

Figure 3.7: CCL mechanism stowed

Following its stowed configuration Figures 3.8 and 3.9 show its travel and its deployed configuration respectively.

Figure 3.8: CCL mechanism travelling

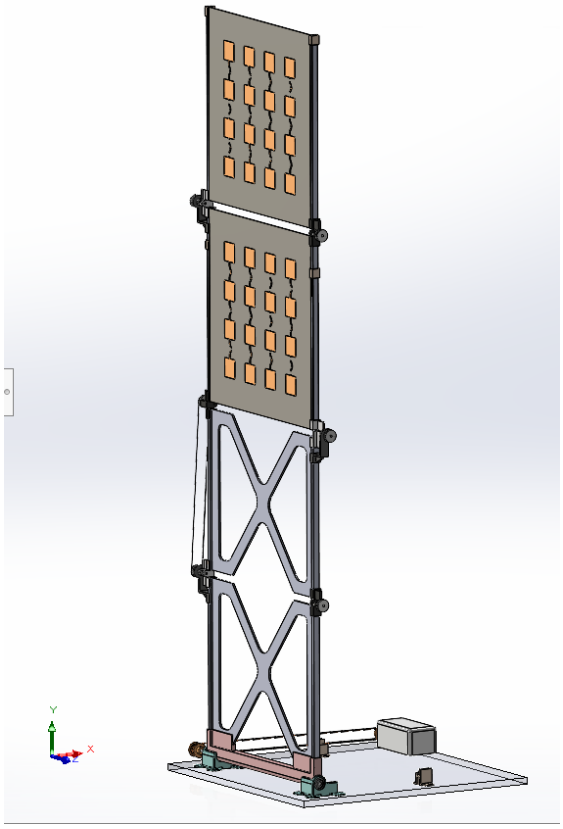

Figure 3.9: CCL mechanism deployed

The panels' flatness at the end of the motion is guaranteed by locking hinges that, in this case, should free the rotation if enough force is applied. One cable is used to represent how the hinges are connected. The pattern would repeat without having a closed loop at the two sides of the panel, for understanding. Plus the two "X" like plates are there to support and overcome the 400 mm in height between the base and the end of the satellite so the SAR panels have visibility to the exterior.

3.3.1 Updated model

After some preliminary analysis of the structure and thermal considerations about the SAR plates' thermal properties already discussed in the other model, the design was slightly updated to increase first-stowed natural frequency, increase thermal conduction and eliminate redundant elements.

The panels have now an aluminum substrate (plate that is behind the panel), to increase the panel's first natural frequency and conduct heat, and the aluminum plate on the lower section was removed as they were not adding much to the deployed natural frequency, were adding weight and were causing the first stowed natural frequency to be below 100 Hz.

Stowed and deployed configurations can be found hereafter.

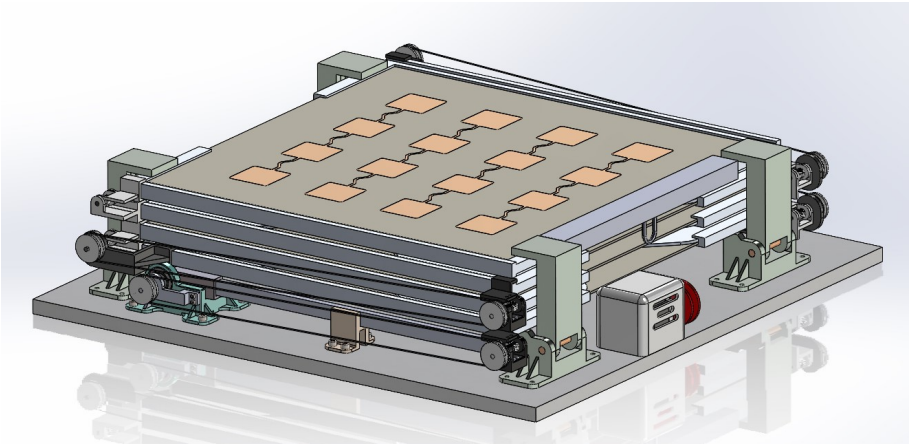

Figure 3.10: Model 2 Stowed configuration - Updated

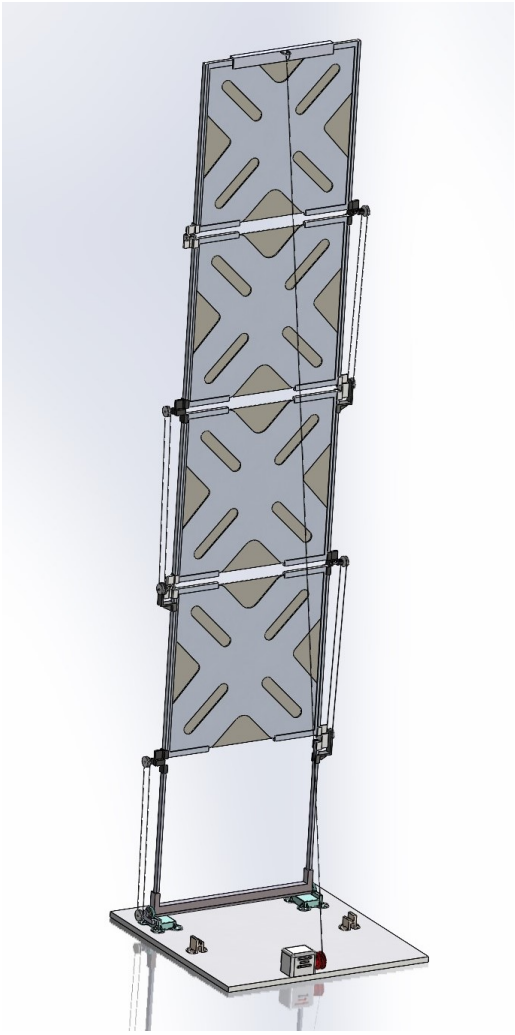

Figure 3.11: Model 2 Deployed configuration (back view) - Updated

As an end note, it is important to refer that the last presented model and the last

structural analysis model are not the same. This section's models are not shown in the structural analysis, because the final analysis is an upgrade of the mechanism shown here. This one, went through iterations to arrive at the model seen at the end of the next chapter since it was noticed that for achieving good mechanical properties, a relatively thick plate would be needed on the back of the panels. Its successor recurs to fin-like structures to add rigidity while maintaining or reducing the weight and also the model in this section doesn't allow to have full contact between the plates, a structural advantage explored in the final model. There was just no opportunity nor enough time to represent the analysis final model in CAD software.

3.3.2 Discussion

As in the last model, a brief discussion of this mechanism is here taken. The mechanism should allow for the same compaction ratio as in the previous model and is lighter in principle since the pantograph model would also need reinforcement behind the panels as these cannot handle the vibrations on their own. It has fewer major parts since there are fewer bars, and pins at rotation points, and from logic should not be prone to thermal-induced problems, with the only change being putting a substrate or a coating in the SAR panels to increase heat conduction. Some issues are still raised by it, mainly regarding the entanglement of the cables and avoiding major slipping.

Because of the presented decrease in failure points, and the overcome of the thermal problem, this model was chosen for structural analysis and iterations. There is though a similarity between the models, and if a future decision tends to go back to the other model and regards its advantages as the better ones, some findings of the structural analysis are interchangeable.

Chapter 4

Structural analysis

In the present section, the structural analysis of the model will be carried out. For the current stage of the project, the analyses here performed have the intent not to be detailed simulations of a final structure with all its parameters defined, but rather the simulation of a coarse representation of a structure to be detailed in the future, aiding on its sizing to try to, in a preliminary stage, reduce its mass while making sure it is capable of handling the requirements and flight conditions. The structure chosen in the previous chapter is here remodeled so it is adequate for a simple FE analysis and Quasi-Static, Sine sweep, modal and random analysis are performed on the structure to check for its behavior.

4.1 Finite element model

4.1.1 Model

After the design of the possible configurations for the mechanism, a finite element model was constructed. A simple model was built from 1D beam elements and shell elements in the ANSYS software which was compared to a more detailed one to mimic the latter's behavior as closely as possible. The procedure to obtain the model is described hereafter.

The geometry designed in Solidworks was uploaded to the ANSYS SpaceClaim software for geometric treatment before proceeding to ANSYS Mechanical where the model is meshed and prepared for the solver. In SpaceClaim, the pulleys were removed as well as the cables as this is for preliminary design purposes and evaluation of the structure's dynamic behavior, thus these elements were considered not significant to the overall behavior of the structure. The hinges axles and other bracelet-like pieces around the beams were also removed to save on the number of el-

ements since there is a limitation in the current version of the software and they were not necessary for the analysis at such a preliminary level. With this, one model was constructed retaining its hinges to represent more accurately the structure. Another model as described above was designed simply by using beam and shell elements, afterwards, some revolute joint elements (these are elements in ANSYS that connect the DOFs of two regions only allowing rotation in the local Z axis, which can be defined) were used to mimic the behavior of the physical hinges. The two models are displayed in figures 4.1 and 4.2.

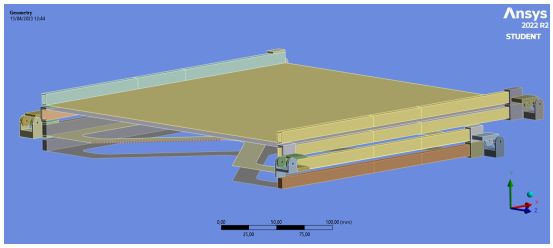

Figure 4.1: Model of mechanism retaining the hinges

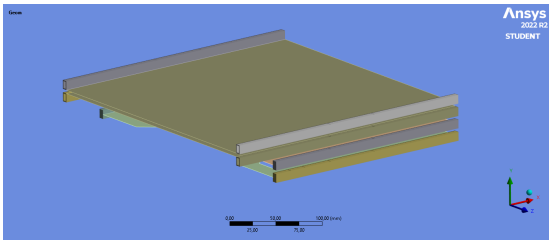

Figure 4.2: Model of mechanism simplified, hinges represent by joint elements

The models were then exported to ANSYS Mechanical for the definition of boundary conditions, connections, and meshing. The meshes for both models are presented below.

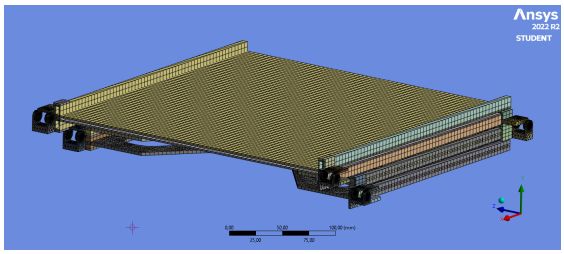

Figure 4.3: Detailed model mesh

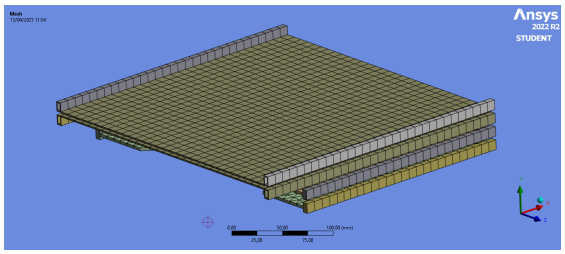

Figure 4.4: Simple model mesh

The model having the hinges represented uses solid second-order tetrahedral elements for the beams and hinges, and shell elements for the panels and yokes. The choice of shell elements for the plates is appropriate since the plate has two dimensions much larger than its thickness. The use of second-order tetrahedral elements is automatically chosen by ANSYS and is in fact standard practice since the degree of accuracy of first-order tetra elements (unless they are perfectly shaped) is not as good as the second-order version [66]. In the simplified model, beam elements and shell elements were used instead along with joint elements in ANSYS. A mesh composed of only triangular elements was chosen for the yoke panels as they are the ones that better adapt to the geometry of the panels to avoid element distortion.

The defined boundary conditions in the simplified model are here exposed. A fix of all degrees of freedom except rotation in Z at the base connection points (The ones on the vertices of the bottom beam for the simplified model or the bottom axel that allows rotation between the first bars and the base where the mechanism is mounted); A constraint on the Y and Z translational DOFs and all rotations to simulate the opposite end support of Figure 4.5; Finally, a translational DOF constraint at the lateral highlighted region in Figure 4.6 to simulate the hold-down mechanism of the panels which, although not being represented at this staged can be seen in figure 4.20. Ultimately it was changed to setting the DOFs to zero at those points, with the following justification: The blocking of translational DOFs was performed in the detailed model, although not represented. Instead of a line as in the figure 4.6, the lateral face at the same region was all fixed. This latter definition of the BCs had the peculiarity that, by fixing the translational degrees of freedom at a face the rotations are also blocked. One can think of it like this: if a node is surrounded by other nodes all around and all the translational DOFs are blocked, if the nodes try to rotate around a given axis that passes through a line of nodes, they cannot do so because the nodes, away from that line cannot translate, creating a "resisting moment" if one can call it. In the case of defining the lateral supporting bars as 1D elements, the rotation along an axis colinear with the elements is not blocked, influencing the restriction and modes of the structure. This was found while iterating and motivated a change in the simpler model from fixed displacement to fixing all DOFs. In reality, the clamps don't allow for significant translations or rotations, thus this is the most accurate representation possible of the mechanism.

In the case of the detailed model, similar definitions of BCs were performed with the only difference being the use of revolute joint elements on the holes of the hinges.

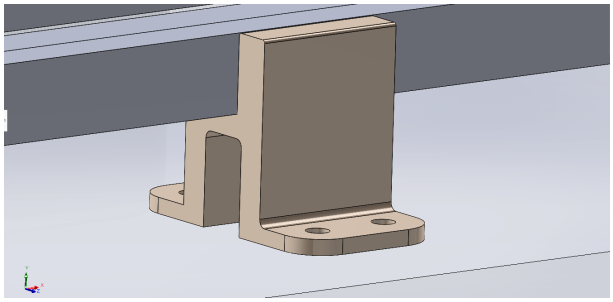

Figure 4.5: Opposite end base support

In the above figure, the support connecting the base and the lower beams is represented. These supports were created to support these beams on the opposite end of the rotational base support.

At this point, this was the definition of the boundary conditions. Later the base connections and hold-down mechanisms will be represented in a simplified way to act as the base where loads will be applied.

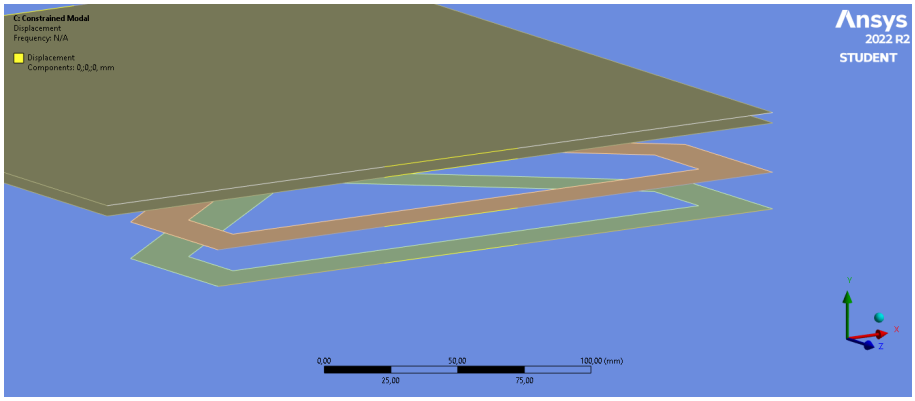

Figure 4.6: Hold down mechanism representative BCs - simple model

In terms of connections, in the detailed model, revolute joint elements were used to restrain the hinges allowing only its rotation around their axle. In the simple model the same revolute joint was used but this time on the vertex of the line bodies representing the supporting beams.

With the boundary conditions set, a modal analysis was performed in both models in order to validate the simpler model in an alternative way since no similar examples were found in the literature and there was no possibility of building the physical model. In Appendix A.1, a table in Excel giving calculated values is displayed to check the correlation between the two models. The relative error was calculated for each modal frequency and an error above 5% turns the conditional formatting in Excel to red meaning it is not acceptable, where green is for values sitting below 5%. Below, Table 4.1 shows the comparison between the first 10 modes and their relative error.

As can be seen, the two compare well as the majority of all retrieved modes have a relative error below 5% and so the simpler model will be used from now on as it allows for simpler changes and much less computational cost.

4.1.2 Model Checks

It is good practice to perform some checks on the model before starting further analysis. These allow to catch errors in the model, an example is that when performing a modal analysis an under-constrained model will move in unrealistic ways or move only one component independently. In [67], ESA lists usual checks performed in the model to see if the model is ready or has any problems that need to be addressed. The checks ran were:

Table 4.1: Modal frequency comparison between detailed and simple models

Detailed model	Simple model	Relative error
59.80	58.91	0.0150
60.61	59.97	0.0107
63.19	62.46	0.0116
64.60	64.33	0.0042
99.50	98.76	0.0074
100.05	99.48	0.0057
115.79	119.84	0.0350
139.02	132.49	0.0470
162.74	160.71	0.0125
164.70	162.30	0.0146

1. Geometry checks
2. Topology checks
3. Mesh convergence
4. Stress-free thermo-elastic check
5. Reaction force
6. Rigid body modes

4.1.2.1 Geometry and topology checks

Regarding the first point, the objective is to check for unconnected nodes and coincident elements that are not present in the model. The topology check is related to the mesh and element shape. Warping of shell elements, interior shell, and solid element angles, aspect ratio should be within the acceptable range negotiated with the customer, a mesh convergence should be performed and proper element orientation defined. For the first point little to no information is provided in the standards and since there is no real talk with the customer for this project at this stage, some limits found in the literature were established. According to [66] the limits for these quantities are displayed in table 4.2.

Table 4.2: Topology constraints for different element types

Element type	Warp angle [°]	Interior angle [°]	Aspect ratio
Quad	< 10	$45 - 120$	< 5
Tri	< 10	$20 - 120$	< 5
Tetra	n.a.	< 30	$1 - 5$

In the mesh tree item in ANSYS Mechanical, it is possible to do all these checks and retrieve values. The worst element values are reported in Table 4.3. As of this point, there are no Tetrahedron elements in the model, but there will be in the future and the same analysis will be performed.

Table 4.3: Topology constraints check values by element type

Element type	Warp angle [◦]	Interior angle [deg]	Aspect ratio
Quad	1.48×10^{-6}	86.53-93.64	1.319
Tri	n.a.	35.08-85.77	1.717

The elements were all oriented properly as ANSYS allows for an element orientation in the geometry section of the model tree and the respective orientations are shown in Figures 4.7 and 4.8. As can be seen, there was an effort to align the three local axes with the global one. Although not a direct correspondence axis-wise it is direction-wise. The local was kept as such to not alter the material property definition, as in the case of the SAR plates the orthotropic material properties are direction dependent.

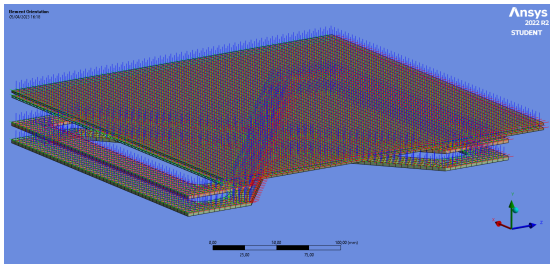

Figure 4.7: Shell element orientations

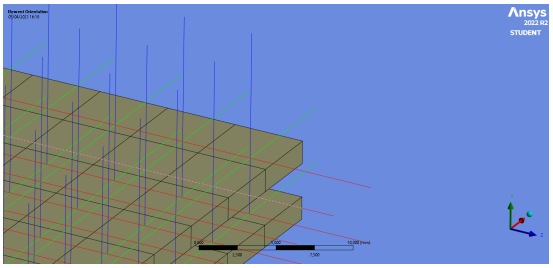

Figure 4.8: Shell elements orientations - closer look

The important consideration is to leave the X and Y axis in the plane of the plate since the two major young moduli are assigned in these directions.

4.1.2.2 Mesh convergence

Following element orientation a mesh convergence was performed. This will allow for achieving accurate and mesh-independent results and at the same time save on computational effort. In the present case, a mesh convergence was performed for a quasi-static case and for a modal case as all of the analyses to be performed are dependent on the results from these two analyses. Besides the different loading conditions, quadratic and linear element convergence will be compared for element choice on the basis of accuracy and computational cost.

The results of the convergence are displayed in the graphs below. The procedure to obtain such a graph was to start with a very coarse mesh and try to double

the element size at each step. Then a standard gravity acceleration is applied to each axis and the maximum deformations are retrieved. The choice of load type comes from the fact that the Quasi-Static analysis is acceleration-based, so the intention was, although with a different magnitude, to use the same load type for convergence. The total displacement at each iteration was recorded. Then the relative error between the last and the actual step is computed and once it is below 5%, as stated in Chapter 8 of [66], the mesh will be assumed to have converged. The convergence was performed for elements, linear, and quadratic to check on differences in accuracy and number of iterations to convergence. Both the deflection and error for both element orders were plotted in Matlab. The first-order element convergence is shown in Figures 4.9 and 4.10, referring to the deflection convergence and the relative error between iterations respectively.

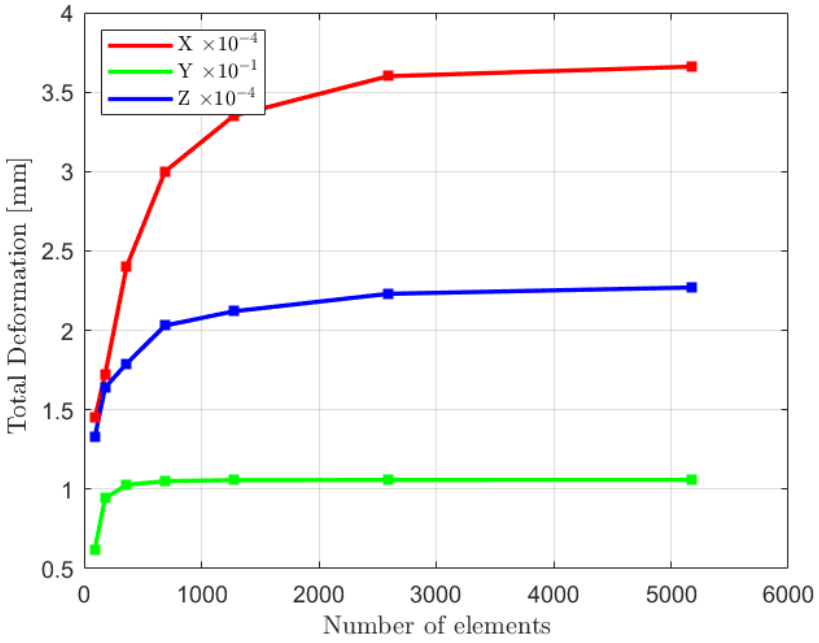

Figure 4.9: Quasi-static linear elements convergence

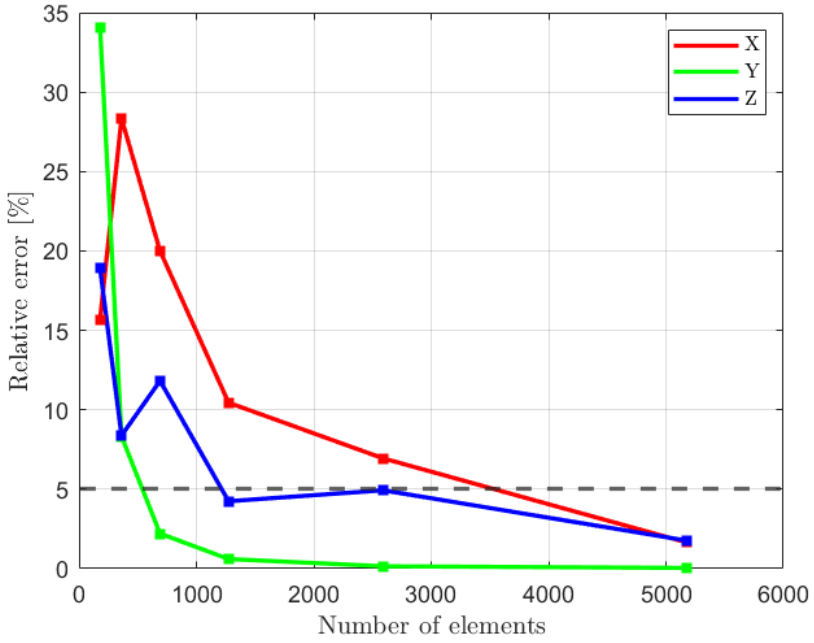

Figure 4.10: Quasi-static linear elements convergence relative error

The second-order element convergence is presented below where Figures 4.11 and 4.12 are respectively the mesh convergence plot for quadratic elements and the relative error for each iteration, to check its quickness to fall below the threshold.

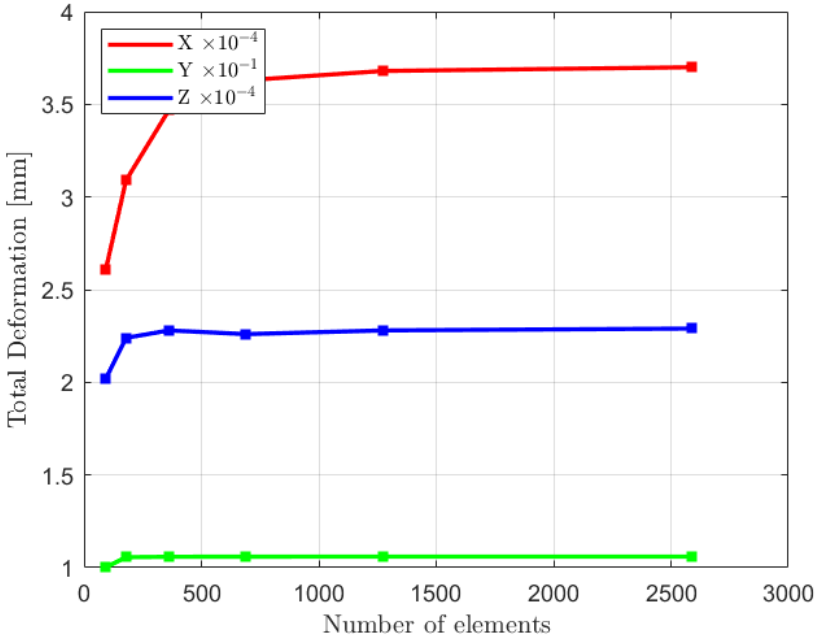

Figure 4.11: Quasi-static quadratic elements convergence

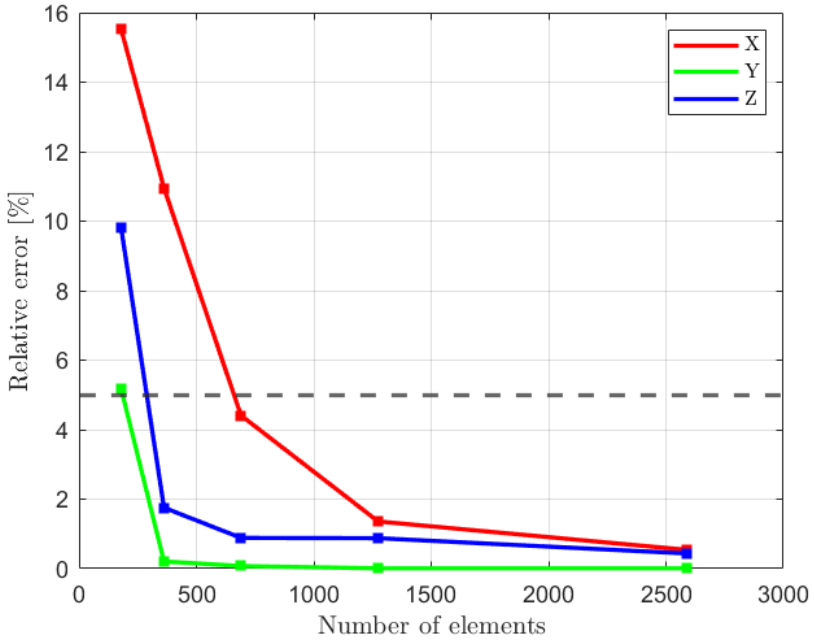

Figure 4.12: Quasi-static quadratic elements convergence - relative error

The final mesh was settled in at least 10 mm (a bit more than the first element size that respects the relative error threshold, 12.5mm corresponding to the point of around 700 elements) of quadratic elements for use in the quasi-static load analysis as the quadratic elements displayed a clear advantage over the linear ones since they reached convergence sooner. In comparison, while the linear elements needed 7 iterations to converge, the quadratic ones needed only 4.

The same procedure was also performed in this case in a modal analysis to check the convergence of the modal frequencies up to 2000 Hz. Excel was used to treat the amount of data retrieved from ANSYS and calculate the relative errors. The modal analysis will be the basis of the sine and random vibration analysis and so it will be the mesh density found in this procedure that will be used afterwards. Results are found hereafter starting with the convergence for linear elements and then showing the one referring to quadratic elements.

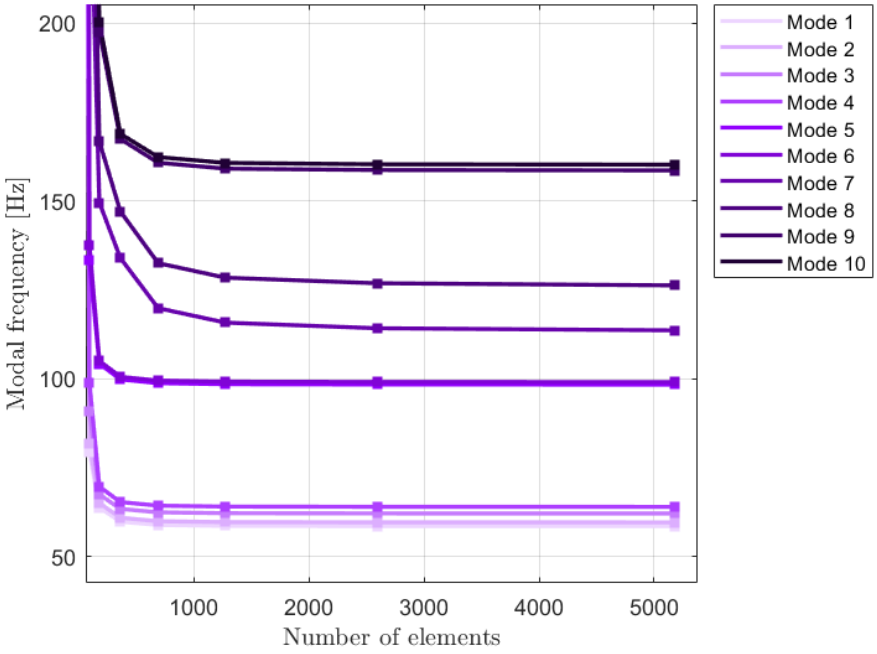

Figure 4.13: Modal convergence - Linear elements

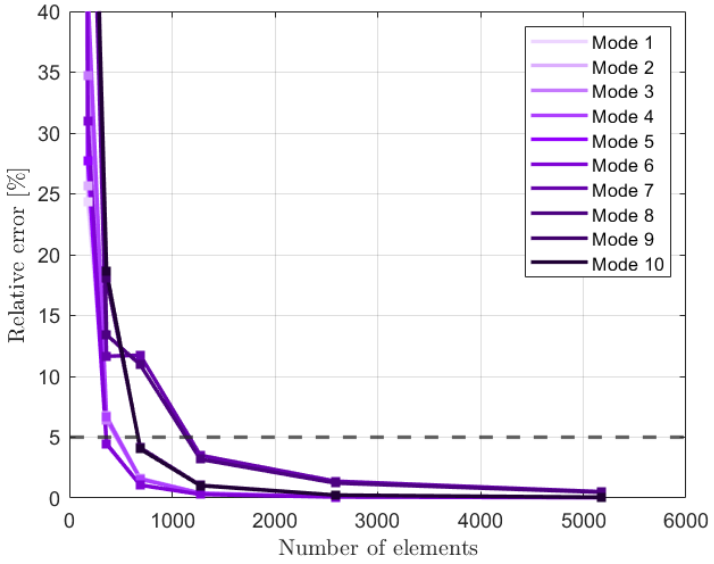

Figure 4.14: Modal convergence relative error - Linear elements

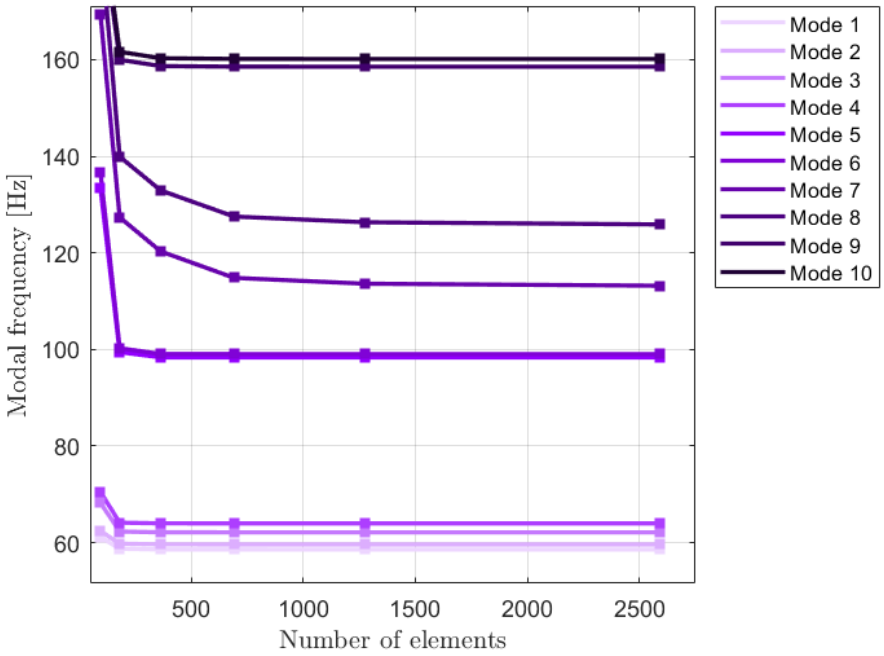

Figure 4.15: Modal convergence - Quadratic elements

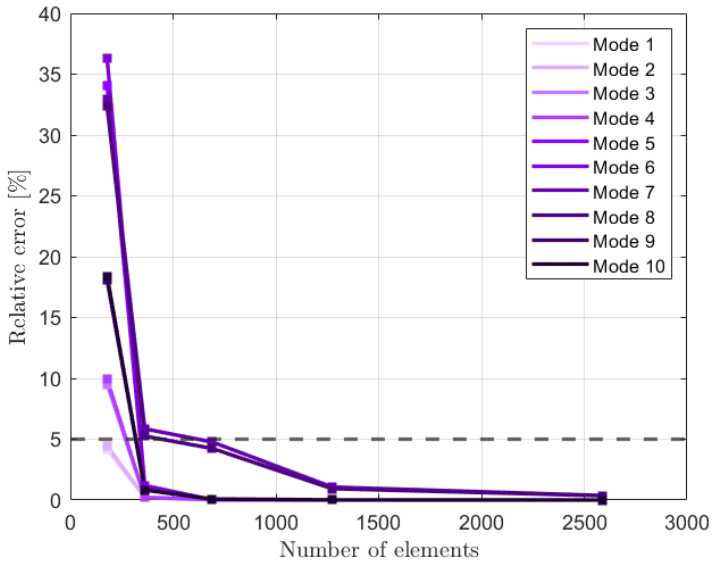

Figure 4.16: Modal convergence relative error - Linear elements

The main conclusions taken from the modal mesh convergence are the following: Once again the quadratic mesh displayed increased accuracy and reduced iterations to convergence; In the case of the quadratic mesh, a mesh of at least 12.5 mm already displays good convergence results up to a high frequency but, for the case of a random vibration analysis where the frequency range goes up to 2000 Hz and ANSYS recommends using at least 1.5 times that value in the analysis, a mesh of at

least 6 mm size displays more accurate results even for those high frequencies. The previous sentence is supported by calculations of relative errors of modes up to 3000 Hz which, for quadratic convergence, can be consulted in Appendix A.2. Therefore, for harmonic analysis, a mesh of 10 mm will be used whereas for random vibration a 5 mm mesh is more appropriate.

4.1.2.3 Thermo-elastic check

A thermal check was performed on the model to check that, if the model is constructed with an isotropic material and subjected to an increase in temperature, no stresses nor rotations exceed a value agreed with the customer. For the given case the values present in the standard will be used. According to [50] an aluminum alloy should be used as dummy material, a ΔT of 100 K imposed and as boundary conditions, any statically determined one. The Von Mises stress should be below 0.01 MPa and the maximum rotation less than 10^{-7} rad. For the present analysis, the aluminum alloy used in the lateral bars is going to be the dummy isotropic material. The initial temperature of the mechanical analysis in ANSYS is set by default to 22°C so a temperature boundary condition of 122°C is applied to the whole model. In regards to boundary conditions, a fully-hinged (block translations in X, Y, and Z) support was applied to the closest lower corner of the model, and roller supports (one displacement free) on three other edges, one on the right is free along X and, one on the left is free along Z and one in the top closest corner free along Y, were applied, therefore letting the model expand and slide freely. Hereafter the deformation relative to the initial conditions the Von-Mises stress value in the whole body and a table with the rotations are presented.

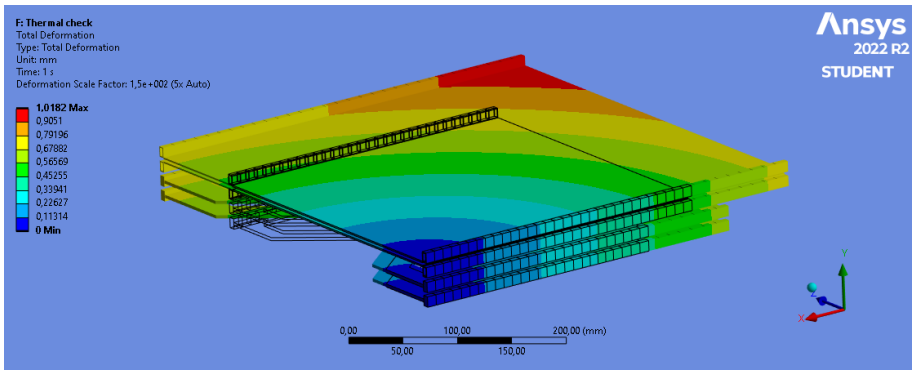

Figure 4.17: Deformation due to temperature variation in thermal FE check

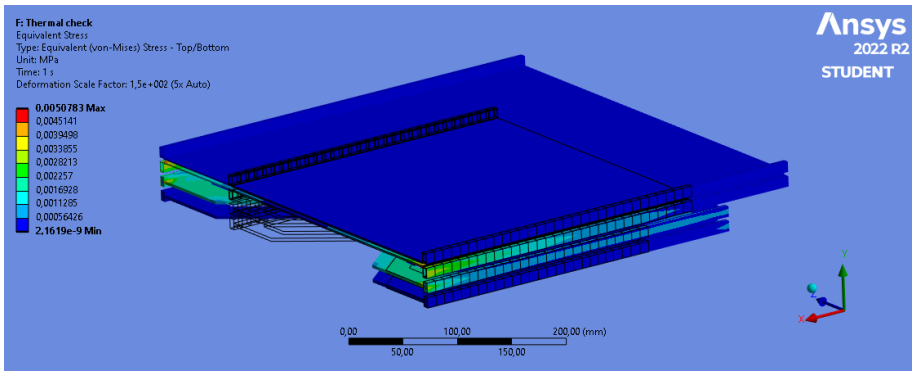

Figure 4.18: Von Mises stress for the thermal FE check

Table 4.4: VM Stress and rotations along x,y and z due to free thermal expansion

VM stress	Rot x	Rot y	Rot z
5.08×10^{-3}	5.28×10^{-7}	6.21×10^{-8}	5.26×10^{-7}
< 0.01	$< 10^{-7}$	$< 10^{-7}$	$< 10^{-7}$
✓	×	✓	×

As can be seen, two rotation values were not under the threshold but in terms of physical quantities the values are negligible and are on the order of magnitude of the threshold thus it is assumed that there is no problem with the model.

4.1.2.4 Reaction force check

A force reaction check was also performed. it consists of applying a given load to the structure and checking if the reaction on the boundary conditions has the same magnitude. This test was performed by applying a unit force to the model and checking the reactions. Figure 4.19 illustrates this act. The reaction forces were retrieved at all boundary conditions and summed. The results are presented in Table 4.8.

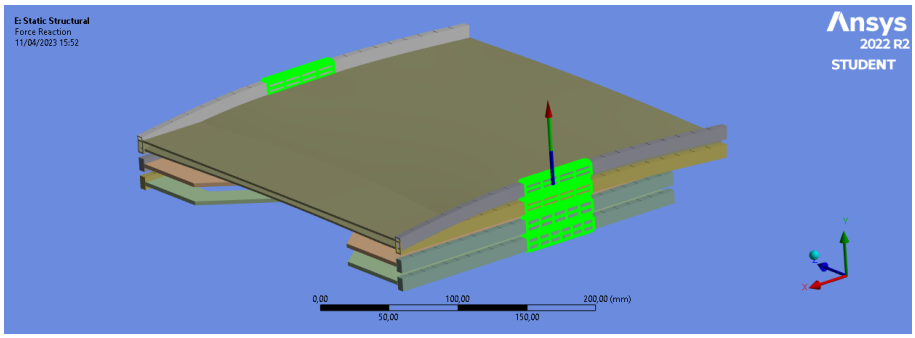

Figure 4.19: Reaction load check illustration

Boundary condition	$\mathbf{R}_x$ [N]	$\mathbf{R}_y$ [N]	$\mathbf{R}_z$ [N]
BC1	0	1.00040	-3.10×10^{-5}
BC2	5.18×10^{-12}	6.96×10^{-6}	3.15×10^{-6}
BC3	0	-3.73×10^{-4}	2.78×10^{-5}
$\sum$	5.18×10^{-12}	1.000034	2×10^{-10}

Table 4.5: Reaction load check values

When summing the value of all the boundary conditions it can be seen that the values are almost equal to 1, meaning that the reaction force calculation is being well performed.

4.1.2.5 Rigid body mode magnitude check

Finally, a normally performed test to the model is the rigid body mode one. The procedure is to retrieve the first 6 rigid body modes and the first elastic mode. The ratio between the highest rigid body mode and the first elastic mode should be below a certain value discussed with the customer. A normal value of this ratio as reported in [67] is $\chi < 10^{-4}$. Another constraint is that all the rigid body modes should be below $\delta = 0.005$. All the previously referred modes plus the calculated ratio are reported in the table below. The rigid body modes are reported in Appendix A.3.

Table 4.6: Modal frequencies

Mode	Frequency [Hz]
RBM1	0
RBM2	0
RBM3	0
RBM4	4.464×10^{-4}
RBM5	4.700×10^{-4}
RBM6	1.178×10^{-3}
EM1	30.960
χ	3.805×10^{-5}

4.1.3 Updated model

After the model checks, several quasi-static and harmonic analyses were performed but after evaluation from the company's side, it was agreed that the boundary conditions should not be applied in such a way. Instead, a simplified model of the clamps and the base connection should be represented in the model, and the boundary conditions set on the screw holes that connect them to the base. It is an

important step since in the case of harmonic and random analysis, a base excitation is defined and this piece should act as a base. The updated model is presented in figure 4.20. It is important to refer that only two panels were designed as at this stage it was only necessary to understand the behavior of the structure and the number of panels was still not defined.

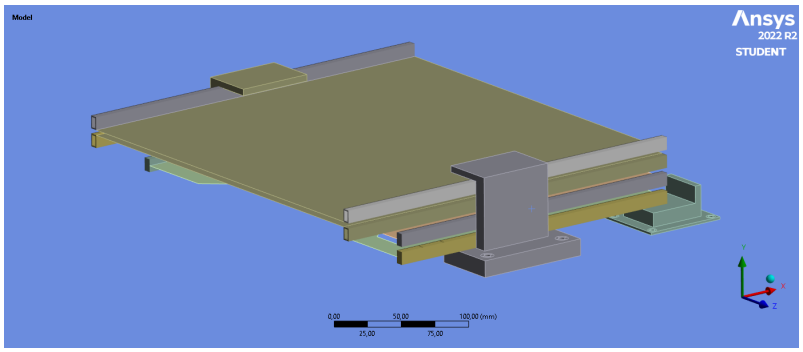

Figure 4.20: First model, hold down clamps represented

Some of the checks were redone on this updated model. The thermal check was not included because the way the connections were settled does not create a statically determined condition essential for that type of analysis. The mesh convergence was also not included because it was already performed in the regions of interest, a detailed representation of stresses and displacements is not necessary for the supports, and the mesh was created as large as possible in those areas as will be described in the next section. Table 4.7 gives the values corresponding to each check for the updated model

Element type	Warp angle [°]	Interior/Edge angle [°]	Aspect ratio
Quad	1.48×10^{-6}	86.53-93.64	1.319
Tri	n.a.	35.08-85.77	1.717
Tetra	n.a.	166.46	15.695

Table 4.7: Topology constraints check values by element type

Quad and Tri elements remain within limits since no major modifications were made to them. In the case of the tetrahedron element, the maximum corner angle and maximum aspect ratio were retrieved. Although it may seem that the mesh is very badly shaped, it is not the case. There are some elements that turned out with very bad quality since there was an effort of keeping the overall number of nodes to a minimum while refining a bit the region around the holes. As previously mentioned, the supports are not very relevant for stress analysis but the hole will be because of the boundary conditions and the future bolt analysis. The transition between the

big mesh in the upper region of the supports to the fine mesh in the holes is not smooth and creates these badly shaped elements as can be seen in figure 4.21.

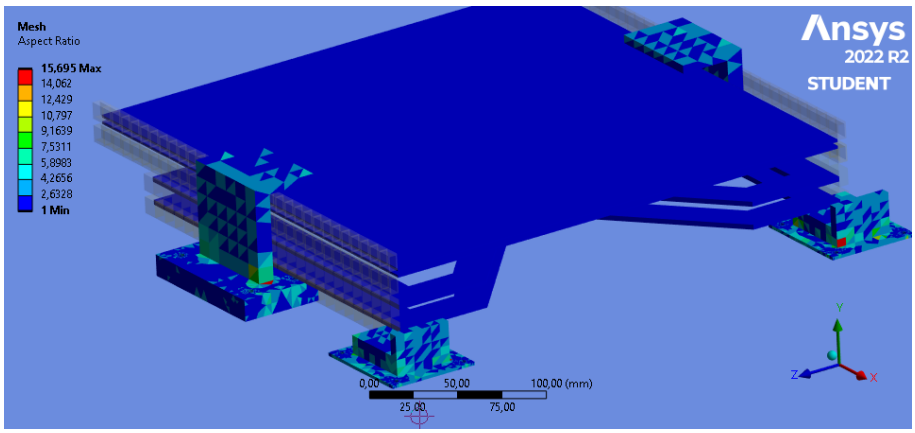

Figure 4.21: Aspect ratio of the elements on the updated model

The reaction forces are practically equal to the applied load (1 N in the negative Y direction), therefor the model is good in this matter.

Boundary condition	$\mathbf{R}_x$ **[N]**	$\mathbf{R}_y$ **[N]**	$\mathbf{R}_z$ **[N]**
$\sum$	6.7×10^{-6}	1	6.4×10^{-6}

Table 4.8: Reaction load check values

Finally, the modes check also gave good results thus the next step is to perform the analysis. Rigid body modes will no longer be displayed to not elongate the present work.

Table 4.9: Rigid body mode check - first model

Mode	**Frequency [Hz]**
RBM1	0
RBM2	0
RBM3	9.756×10^{-4}
RBM4	1.648×10^{-3}
RBM5	1.822×10^{-3}
RBM6	3.940×10^{-3}
EM1	59.492
χ	6.625×10^{-5}

4.2 Analysis

After preparing and verifying the model, the needed analyses were performed. These include quasi-static, modal, harmonic, and random vibration analysis. For

each, ANSYS inputs and considerations are detailed, the analysis is then run and the results are presented. These results will help with the sizing of the overall structure. Finally, the model will be sketched in the deployed configuration to evaluate its natural frequencies.

4.2.1 Quasi-static analysis

Since there is no model of the spacecraft at this phase and a coupled loads analysis between the SC and the panels becomes impossible, it was assumed that the acceleration felt by the antennas is the same as at the center of gravity (COG) of the SC. Having this said the accelerations reported in Figure 2.4 of the literature review for the Vega rocket will be applied to the model. This approach is not very conservative. The quasi-static accelerations result from the maximum accelerations encountered from a coupled loads analysis between the satellite and the deployable structure. Even though this is true the study was carried out with these values in the absence of other values. The envelope reported in Vega's launch vehicle user manual [52] will be used. Twelve points were marked to help to identify them as seen in figure 4.22.

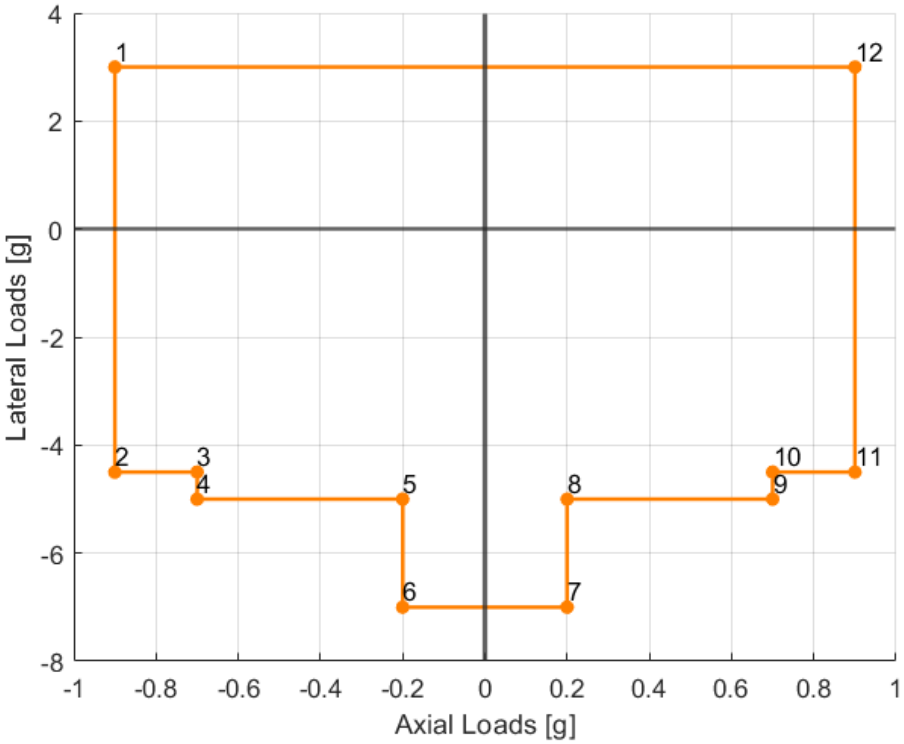

Figure 4.22: Matlab plot of Vega's quasi-static loads envelope

In total, 3 axis combinations were analyzed considering the 12 points, Y/X Y/Z, and Y/-X as there is a symmetry in the XY plane, thus employing that applying

loads in the Z positive or negative direction will lead to symmetric results. Mesh-wise, taking into account the convergence performed previously the mesh will be composed of second-order elements with a global mesh size of 10 mm.

The simulation was run for all the combinations discussed above by attributing a set in ANSYS to each point in the envelope and running it all at once to save time. The deformed shape for one point in the envelope of the Y/X axis combination is shown in Figure 4.23. The other deformed shapes are very similar for any other point (only with deformation magnitude and direction changes) or any other axis combinations since the influence of an X or Z acceleration in the deformed shape is negligible. The results were stored in an Excel sheet but for simplicity, only the maximum (in absolute value) values encountered at each axis combination will be presented.

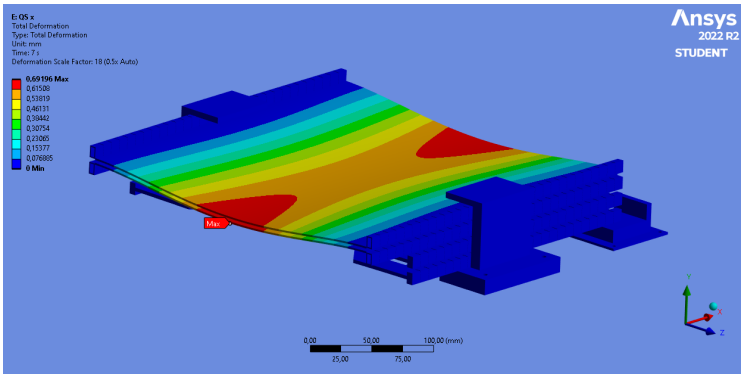

Figure 4.23: Quasi-static deformation Y/X

The maximum values for stresses and deformations are reported hereafter. Since the SAR plates were defined as an orthotropic material the maximum absolute stress value in X and Y was retrieved in the absence of more allowables to calculate other, more accurate failure criteria. In the Z, since the plate is thin the stresses were disregarded. The maximum absolute bending stress was also retrieved to compare with the tabulated ultimate values.

Table 4.10: Deformation and stress values quasi-static load case - initial model

Load case	Total deformation [mm]	VM beams [Mpa]	$S_{max,abs}X$ [Mpa]	$S_{max,abs}Y$ [Mpa]
Y/X	0.692	4.810	4.038	1.036
Y/Z	0.692	4.811	4.040	1.035
Y/-X	0.692	4.810	4.038	1.036

At this point, the next step would be to calculate the margins of safety. While performing the quasi-static analysis a harmonic analysis was also performed which

revealed a structural failure as will be detailed later. For this reason, the margins of safety will only be presented after model iterations.

4.2.2 Modal analysis

The analyses that will be held afterward are based on modal superposition to save on computational time, therefor the modal analysis is the basis for them. A mesh convergence was previously performed showing a clear advantage in the use of second-order elements and a global mesh size of at least 12.5 mm for the range of harmonic analysis. Having this present, a mesh of 10 mm of global size was used and the modes were retrieved. For simplicity, only the first 10 frequencies and the shape of the first mode will be shown. The pictures of the modes can be found in Appendix A.4. The values here shown are obtained considering the supports and connections to the base.

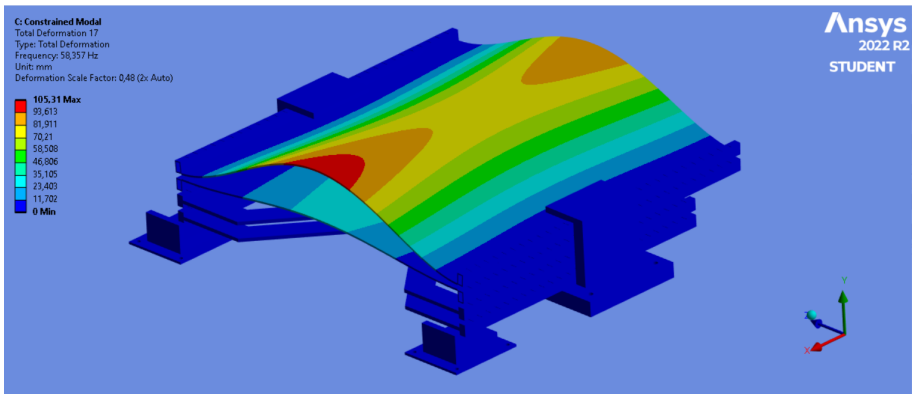

Figure 4.24: First mode - first model

Table 4.11: First 10 natural frequencies of vibration - first model

Mode	Frequency [Hz]
1	58.357
2	59.598
3	62.069
4	63.908
5	98.324
6	99.015
7	113.92
8	137.11
9	157.63
10	159.94

As was spotted, the modes are greatly represented on the plates, the lateral beams do not contribute much to the vibration deflection-wise although increasing the natural frequencies of the model by adding stiffness.

4.2.3 Harmonic analysis

The harmonic analysis was performed in the model with the loads prescribed in Figure 2.6. The frequency domain was thus subdivided into two intervals, one from 5 Hz to 20 Hz and another from 20 to 100 Hz as in the spectrum. The type of excitation used in ANSYS was the base excitation option, which allows the input of a harmonic spectrum in the boundary conditions of the model. In this way, the real-world behavior of the structure is better simulated since in reality its connection to the spacecraft, moves and accelerates with the spacecraft itself (assuming rigid connection behavior).

The critical deformation to store is the one in Y since the plates are much more flexible and are less restricted when compared to the support beams while being free to vibrate vertically. The frequency response of the structure was also retrieved and will be displayed for each axis.

First, the deformed shape of the most critical condition is presented in Figure 4.25. This condition corresponds to a harmonic load of 24g in the Y direction of the global coordinate system, particularly at the resonance with the first mode where maximum relative deformation goes past 70 mm at the two top plates. This is clearly undesirable and the plate has long failed for the assumed parameters and material properties. This shows a need to reinforce the plate in a way to mitigate such response and increase the first resonant frequency.

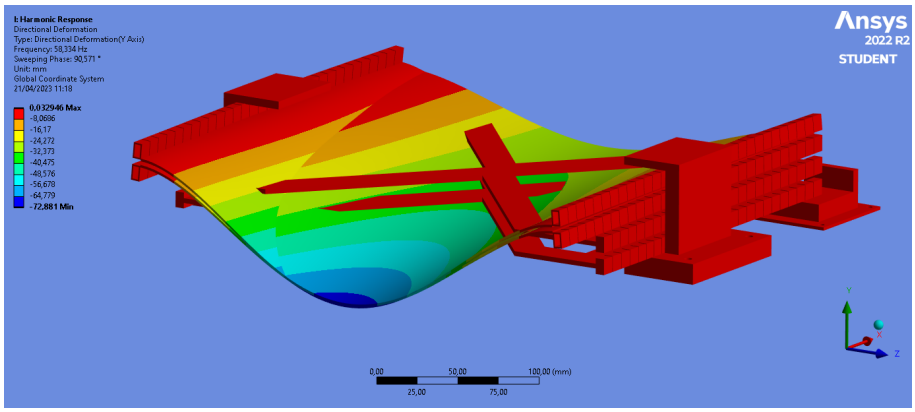

Figure 4.25: Deformed shape at response critical point (True scale) - sine sweep

The frequency response in the Y direction, as it was found to be the critical one for all the cases deformation-wise, the loadings in the 3 axes in the 5-20 Hz frequency range is depicted below:

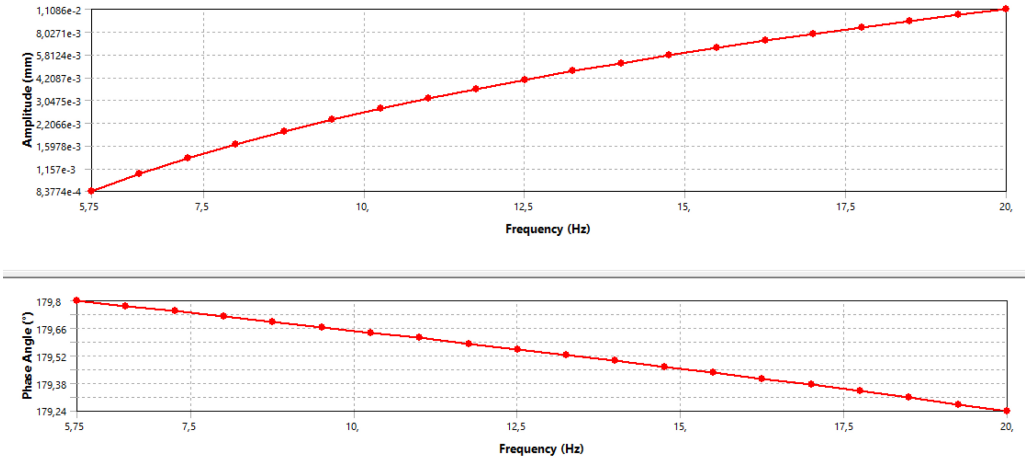

Figure 4.26: 5-20 Hz structure frequency response - X axis

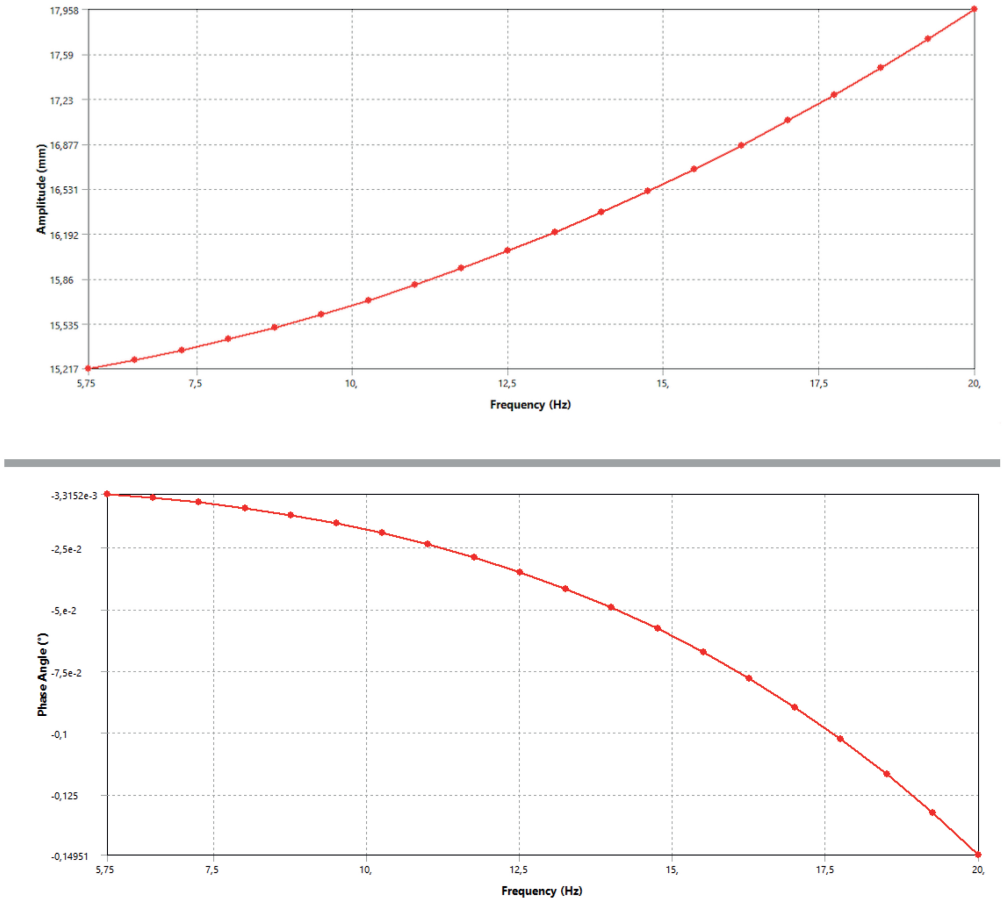

Figure 4.27: 5-20 Hz structure frequency response - Y axis

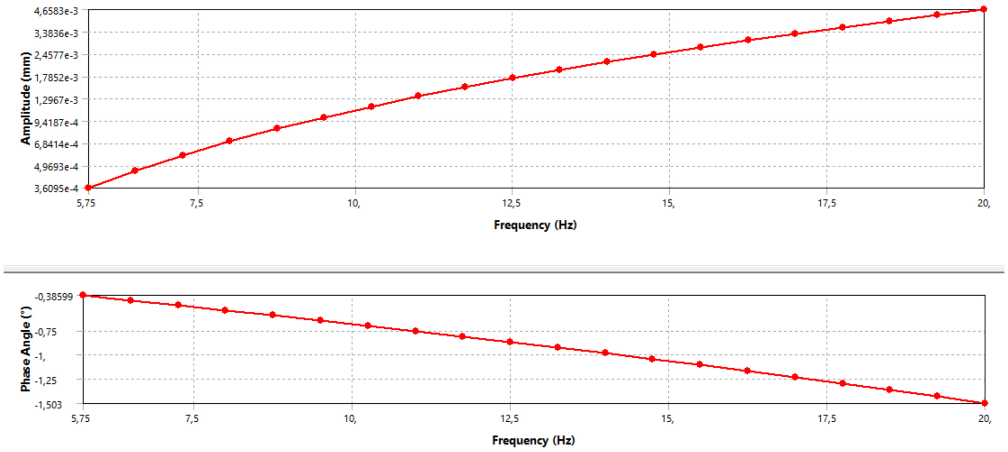

Figure 4.28: 5-20 Hz structure frequency response - Z axis

As can be seen, since the model has no natural frequencies in the excitation range it does not amplify the input spectrum. There is no visible transition in phase nor in amplitude, except for the Y-axis case where some rise towards the first natural frequency is already seen. On the other hand, it is expected that in the next range, there will be some amplification as some natural frequencies fall in between this range. In the 20-100 Hz range, the responses in the Y (out of plane direction) over the frequency are:

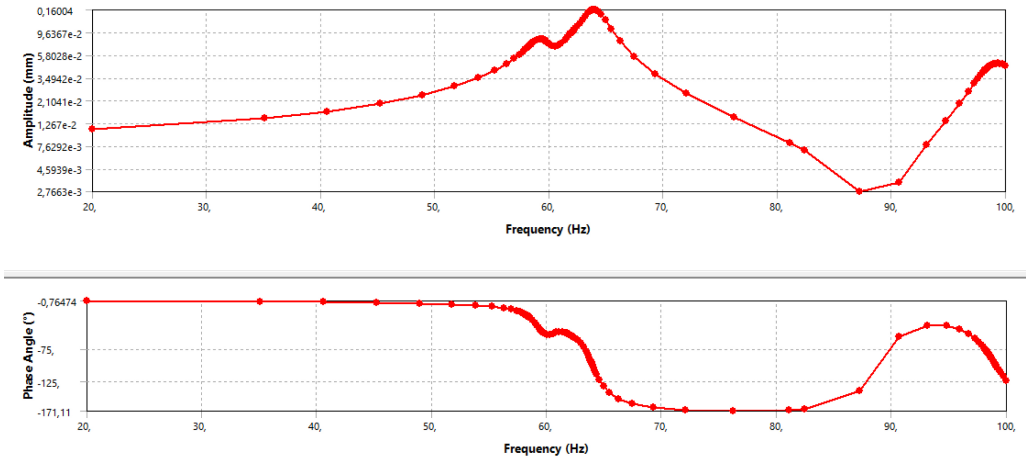

Figure 4.29: 20-100 Hz structure frequency response - X axis

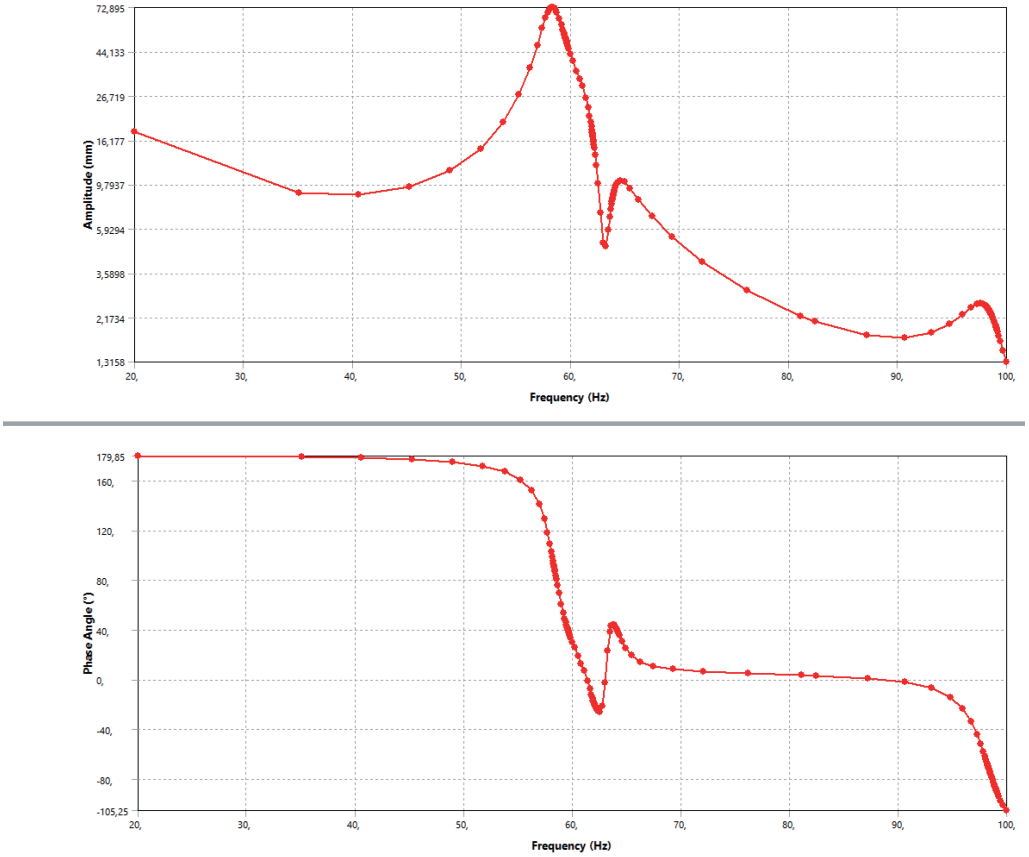

Figure 4.30: 20-100 Hz structure frequency response - Y axis

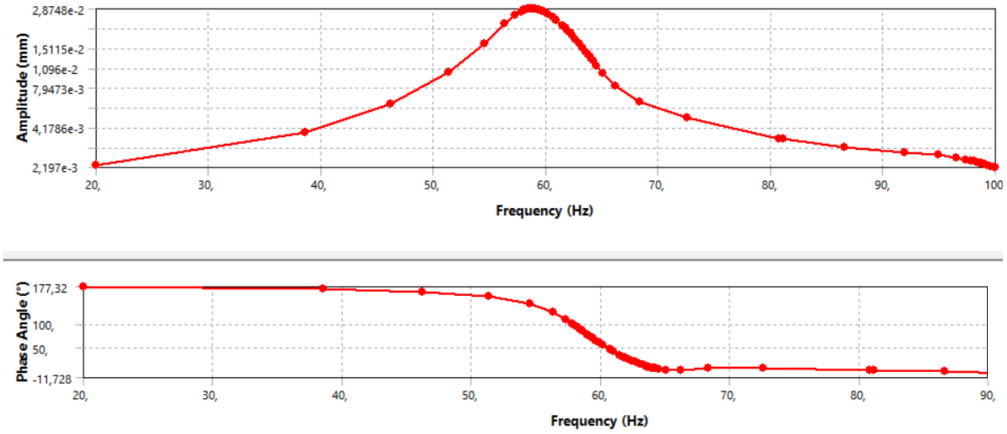

Figure 4.31: 20-100 Hz structure frequency response - Z axis

In the present range, the responses to the excitation in the X and Z directions although there is some amplification in some frequency ranges the overall response of the structure can be neglected and is not important for critical studies. The issue arises from the excitation in the Y direction. The amplification is strong and, by obtaining the frequency and phase of maximum response by a frequency response

analysis provided by ANSYS Mechanical, it is possible to retrieve the directional deformation at that point of interest. The results show a relative displacement of roughly 70 mm (see figure 4.30) between the overall structure and the top panels. This type of behavior has long led to the failure of the upper panels as is discussed hereafter. The next step is then to reinforce the panels in a way to increase the natural frequencies of the structure.

Afterward, the margins of safety will be calculated for a structure with better reinforcement and for all the cases. At this point, there is no point in performing such calculations as the plates have failed. It is easy to prove this by taking the critical point on the frequency response previously referred to and retrieving the equivalent stress results from ANSYS, well displayed in the picture below.

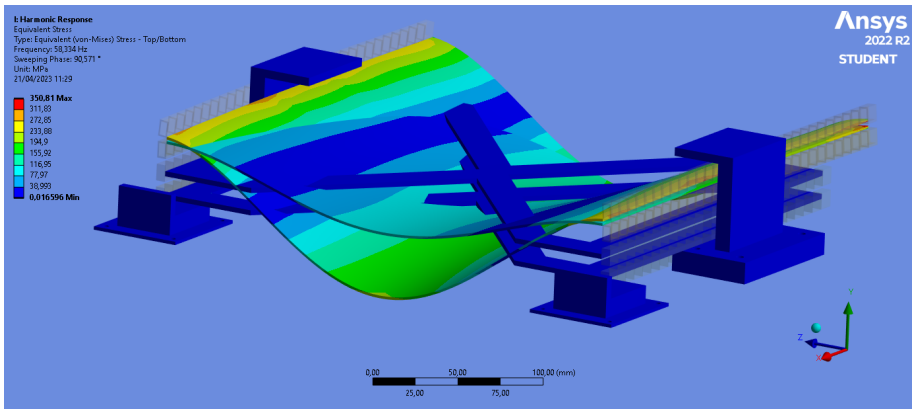

Figure 4.32: Equivalent stress at the plates for critical resonance

Here it can be seen that the maximum stress values, even discarding artificial stress concentration points are well above the strength of the material.

4.2.4 Deployed configuration modal analysis

The final objective of the mission for the equipment detailed in this thesis is to deploy. In the deployed configuration the antennae will connect together to form a long and slender rectangle whose final length should be around 1.2 meters or more (extra length from the supporting structure) corresponding to four SAR panels. Due to its big length-to-width ratio and low thickness, the structure will have in theory a low first natural frequency. As a requisite from the company's side, the deployed structure should have a first natural frequency higher than 1 Hz.

The model was designed in the ANSYS Design Modeler interface by creating line and surface bodies and patterning it in one direction. Each set of panels plus two beams are connected to the other two (except for the tip one) by using fixed joints making the assumption that the hinges when latching create a stiff connection

between the panels, although in reality there is always some gap in the latches which is neglected at this stage. At the root, fixed support was used to simulate, in a simplified way, the connection to the satellite.

The starting point for the iteration procedure was to start with the design dimensions for the beam's cross-section and then change it in a way that satisfies the requirements. The final configuration is shown in Figure 4.33 yielding a final first natural frequency of 1.9 Hz. The beams' cross section was maintained constant along the length as it was found to be enough to satisfy the requirement and maintain simplicity. Even though it was enough it was found while iterating that having a smaller cross-section at the tip and thicker at the root increased the natural frequency. This finding could be helpful in the future, for now, the design was maintained as shown. Another finding was that for a single array of panels extending in one direction, the first natural frequency is proportional to $\frac{1}{l^2}$ where l is the length of the array. This latter one is interesting as it allows for an estimate based on the number of panels. Although this relationship was only found when using the same beam cross section in all the panels, small variations should occur.

Just as a final note, as can be seen, the aluminum "yokes", the cross-like shape on the first beams was removed. Two findings while iterating motivated this change. The first was that even after reinforcing the upper panels (shown later), this structure was still resonating below 100 Hz. One option would be to increase the thickness or area of that part. The second finding, which was its small influence on the deployed first natural frequency as it is a bending mode with a rotation axis parallel to the plane, discarded this option since it was unnecessary and would only lead to a mass increase.

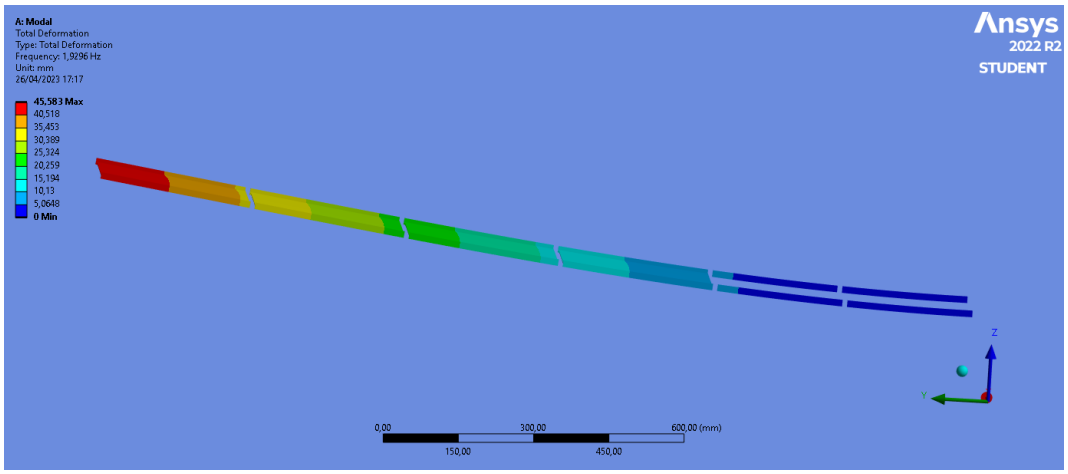

Figure 4.33: Final deployed configuration

4.2.5 Sine sweep - second iteration

There was an effort to reinforce as best as possible the panels to achieve a higher first natural frequency while keeping the mass at a low value. After discussion with the company's side, a requirement was defined, so the first natural frequency is above 100 Hz to be out of the sine spectrum range as is standard practice. Two main changes to the structure were pondered. The first consisted of instead of supporting the plates only by lateral beam, inserting an aluminum supporting structure in the other two edges to create a frame-like reinforcement and simulate an all-around fixed support plate. The second one was to add two small stiffeners and connect them to the plate at 100 mm and 200 mm from one of the sides perpendicular to the ones supported by the main beams. The position of the supporting elements can be understood clearer by seeing Figure 4.34.

First, the idea was to create a section where the plate could be inserted in a tight slot by applying force. In this way, screws are avoided since the plates cannot be drilled. Beam elements are created on each free edge in ANSYS by drawing a line body on the plate edge in SpaceClaim with a C cross-section easily created in the Mechanical environment. The space between the horizontal parts of the C is the plate thickness representing the slot where the plate is inserted.

After applying the proper beam orientations and offsets to mimic their real position, the modal analysis was rerun to check the first natural frequencies.

The frequencies increased but there is still some in the frequency range of the sine sweep spectrum. The response to this harmonic excitation was then retrieved. Although the deformation has substantially decreased it was still unacceptable and the stresses were still high.

The second model was then built with small stiffeners running across the back of the SAR plates for extra support. Two more plates were added after the deployed modal analysis and the lower aluminum cross-like plates were removed. Fixed boundary conditions were applied to the holes' inner walls and the model is now supported only in the clamps and the rotation connection to the base piece discarding the small beam support of figure 4.5. The model is shown in figure 4.34.

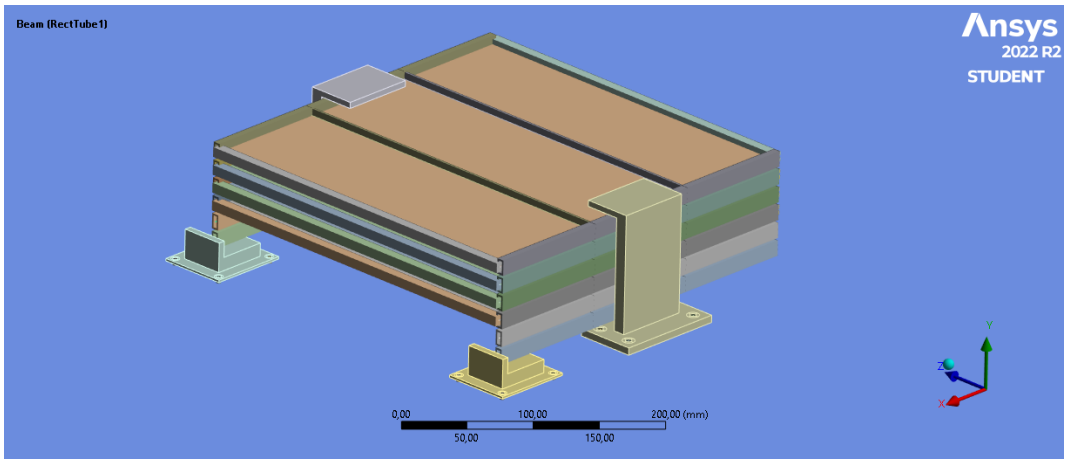

Figure 4.34: Stiffener reinforced model (Second model)

The first mode shape and first natural frequency were increased as expected and are shown below. The frequencies are now out of the sine sweep range and thus the sine loads will not resonate with the structure.

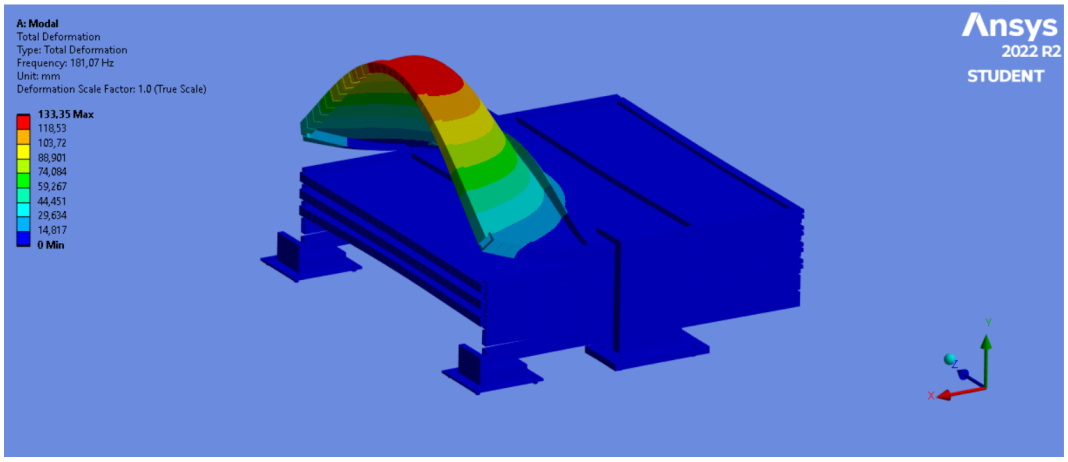

Figure 4.35: Maximum deformation second reinforced model (exaggerated)

Table 4.12: First 10 natural frequency of reinforce model

Mode	Frequency [Hz]
1	181.07
2	206.94
3	214.38
4	217.02
5	218.95
6	222.77
7	230.64
8	244.24
9	253.86
10	261.57

A harmonic analysis was run and the results can be seen below for the excitation in Y, which was the critical one. As expected the model did not resonate with the input spectrum and the model is now safe in this regard.

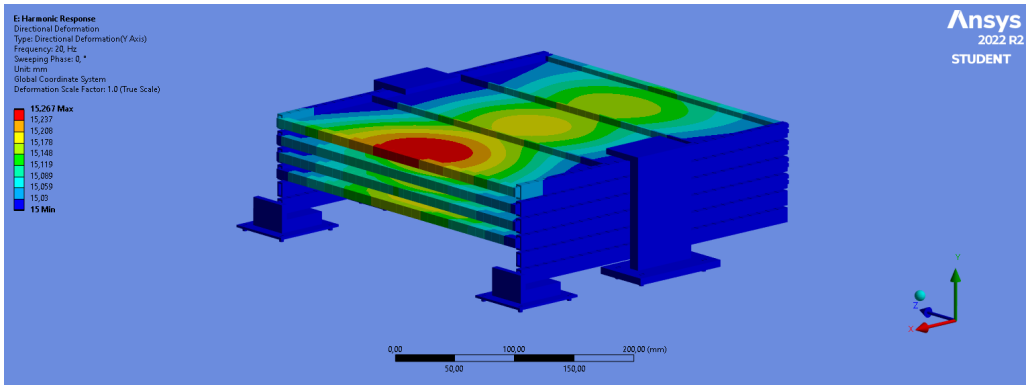

Figure 4.36: Deformed shape at second reinforced model critical point

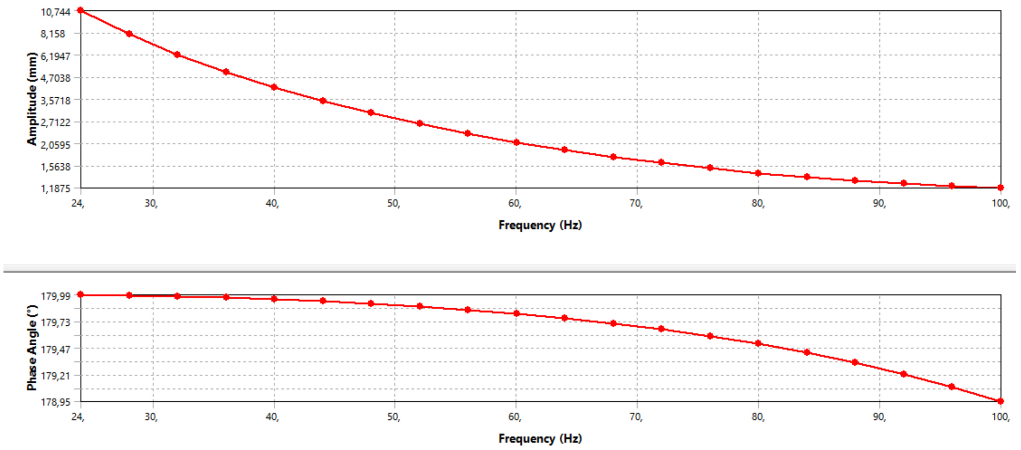

Figure 4.37: Frequency response of the second reinforced model

The response plot at the maximum displacement point shows no resonance in this region as wanted. The displacements are now much smaller.

The Von Mises stress on the aluminum pieces and normal stresses in the x and y local directions on the plates were retrieved. Below one can find two tables with the most important values to retain from the simulation.

Table 4.13: Sine sweep deformation values [mm]

Axis	relative Y deform.
X (5-20 Hz)	1.501×10^{-3}
X (20-100 Hz)	1.507×10^{-3}
Y (5-20 Hz)	0.267
Y (20-100 Hz)	0.266
Z (5-20 Hz)	1.509×10^{-3}
Z (20-100 Hz)	1.515×10^{-3}

Table 4.14: Sine sweep Stress values [MPa]

Axis	VM beams	$S_{11,max}$	$S_{11,min}$	$S_{22,max}$	$S_{22,min}$
X (5-20 Hz)	0.138	1.67×10^{-2}	-1.76×10^{-3}	8.56×10^{-3}	-8.97×10^{-4}
X (20-100 Hz)	0.175	2.04×10^{-2}	-1.68×10^{-2}	1.03×10^{-2}	-8.57×10^{-3}
Y (5-20 Hz)	20.992	1.907	-0.156	1.246	-9.85×10^{-2}
Y (20-100 Hz)	28.303	2.574	-1.905	1.641	-1.242
Z (5-20 Hz)	8.38×10^{-2}	3.47×10^{-2}	-2.86×10^{-3}	2.68×10^{-2}	-2.21×10^{-3}
Z (20-100 Hz)	8.99×10^{-2}	3.71×10^{-2}	-3.48×10^{-2}	2.87×10^{-2}	-2.68×10^{-2}

4.2.6 Quasi-static analysis second iteration

With the reinforced model settled to resist the sine equivalent dynamics, the quasi-static analysis is now performed on the new model. From this simulation, the stresses, displacements, and reaction forces are computed. The maximum displacement found for all combinations is displayed in figure 4.38.

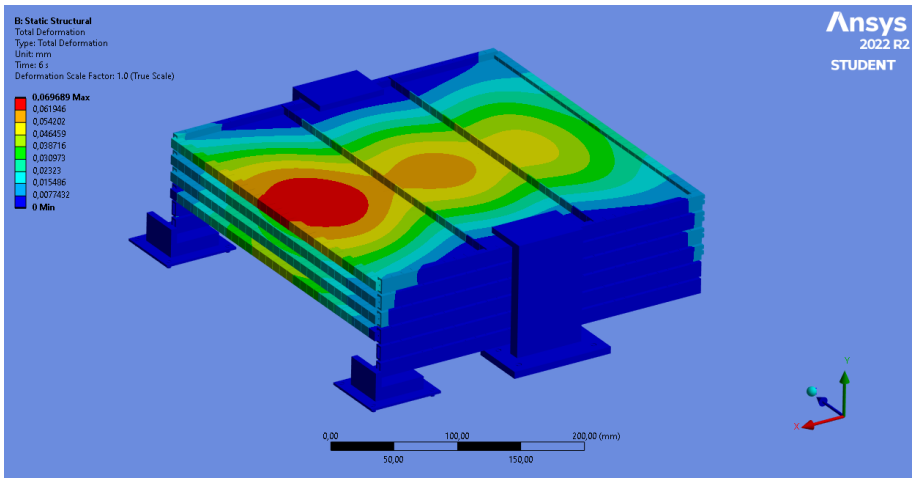

Figure 4.38: Maximum displacement for stiffener model in QS analysis

The maximum stress values for each combination of axis loads are reported in table 4.15 below followed by the ANSYS results for each maximum in each situation.

Table 4.15: Quasi-Static values summary

	Total deform. [mm]	VM beams [Mpa]	$S_{11_{max,abs}}$ [Mpa]	$S_{22_{max,abs}}$ [Mpa]	$S_{bend_{max,abs}}$ [Mpa]
Y/X	0.0697	6.1153	0.4194	0.4806	0.3734
Y/Z	0.0697	6.1423	0.4188	0.4780	0.3736
Y/-X	0.0697	6.1433	0.4187	0.4771	0.3734

4.2.7 Random response analysis

The response to a random excitation by the model designed is here presented. The frequency response spectrum in the X, Y, and Z directions are shown in Figures 4.39 to 4.41. The maximum displacement is presented in Figure 4.42. In fact, a tedious process of iterations was undergone experimenting with different cross sections for the panels' reinforcements and between 2 different aluminum alloys the 6082 and the 7075 until the final configuration was reached. Regarding the beams' cross sections, the iteration cycle was made using cross-sections defined in ANSYS like "Hat"(Omega), "L", "T", "Rectangular tube", and "Rectangular section", which are not commercially available. Then the design was settled using commercially available AA 6062 and AA 7075 cross sections needing only to be cut and assembled.

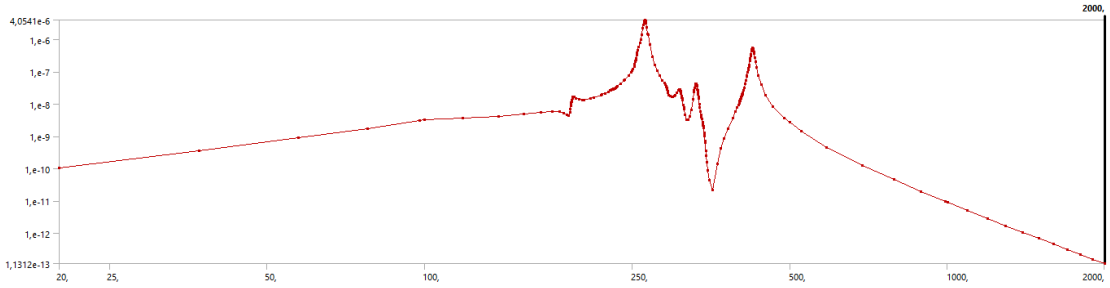

Figure 4.39: Response PSD at the point of maximum displacement - X

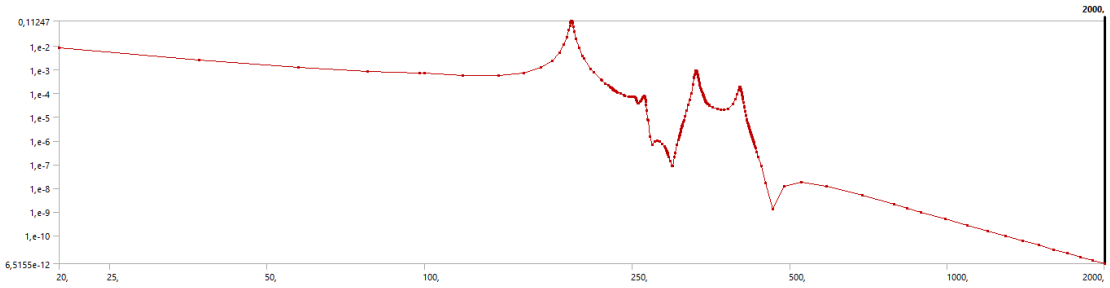

Figure 4.40: Response PSD at the point of maximum displacement - Y

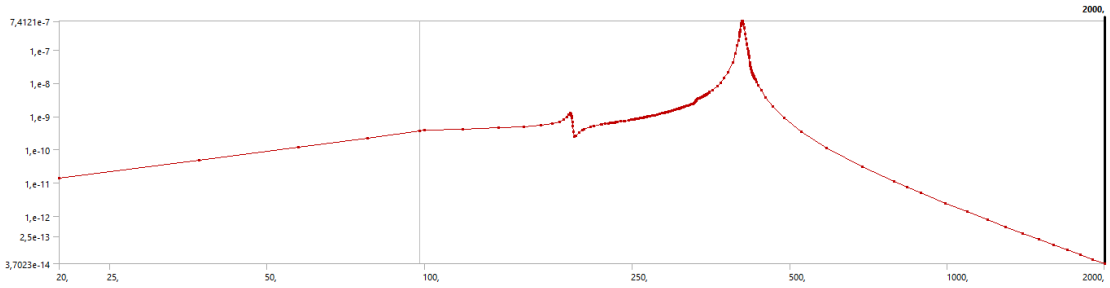

Figure 4.41: Response PSD at the point of maximum displacement - Z

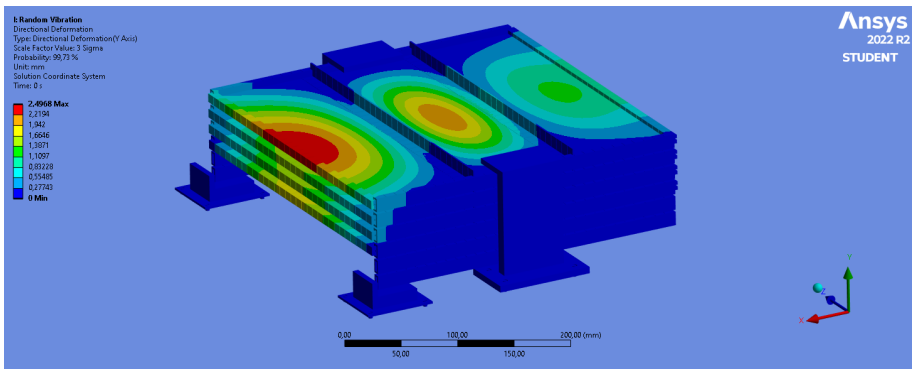

Figure 4.42: Maximum displacement 3σ value

Finally, as in the previous sections, table 4.16 presents a summary of the maximum results from the analysis. All the results are presented in 3σ values, therefore,

corresponding to the least expected occurrences or it will not occur 99.7% of the time, but the use of these values is standard practice in conservative analysis.

Table 4.16: Random analysis maximum values

	Max Y deform. [mm]	Max axis deform. [mm]	S_X [MPa]	S_Y [MPa]	S_{beams} 6062 [MPa]	S_{beams} 7075 [MPa]
X	0.005	0.012	0.315	0.140	0.956	1.278
Y	2.497	2.496	33.805	17.178	80.411	115.340
Z	0.031	0.001	0.233	0.177	0.539	0.281

4.2.8 Margins of safety preliminary model

In the present section, the margins of safety for the models shown previously are presented. They were calculated in Excel for the maximum values of each type of analysis using the safety factor of section 2.5. The calculated margins of safety are presented below.

Quasi-static margins of safety:

Table 4.17: Quasi-Static margins of safety

Loading condition	Yield Aluminum	Ultimate Aluminum	S_X Plates	S_Y Plates
Y/X	15.85	11.39	82.70	51.54
Y/Z	15.77	11.33	82.81	51.83
Y/-X	15.77	11.33	82.83	51.93

Sine-sweep margins of safety:

Table 4.18: Sine sweep margins of safety

Loading Axis	Yield Aluminum	Ultimate Aluminum	S_X Plates	S_Y Plates
X (5-20)	747.55	549.40	2097.46	2950.68
X (20-100)	585.27	430.08	1723.87	2445.95
Y (5-20)	3.91	2.61	17.40	19.27
Y (20-100)	2.64	1.68	12.64	14.39
Z (5-20)	1228.33	902.92	1009.89	942.49
Z (20-100)	1145.08	841.71	945.12	880.45

Random vibration margins of safety:

Table 4.19: Random margins of safety

Loading	Yield		Ultimate			
Axis	AA 6082	AA 7075	AA 6062	AA 7075	Plate X	Plate Y
X	106.81	145.08	110.30	180.02	78.28	102.56
Y	0.28	0.62	0.04	0.47	-0.06	0.15
Z	190.24	663.91	149.91	141.41	139.62	470.34

From the Y-axis input loading, a failure of the plate was seen for max stress in the X direction. This and other motives explained at the beginning of the next section motivated changes in the model

4.2.9 Final model

From the previous model, some considerations were taken and some aspects of the model were discussed. First, the way the model was built would lead to manufacturing and assembly problems. This is due to the fact that the plates needed reinforcement, and small beams, commercially available were used, but that poses the problem of how to connect the beams to the main frame and the plates which should not be perforated, at least in the middle region. Then there is the problem of conducting heat, with such a surface exposed, and not great conductivity properties, the composite SAR plates would need some material behind to conduct the heat.

Due to the previously discussed facts an improved design was built. The new design would start from an aluminum plate which is machined to the desired shape. In this case, a square with the depth of the SAR plate is created on one of the sides, and small squares are removed on the other side to create a grid of aluminum behind for weight-saving and structural support, see below.

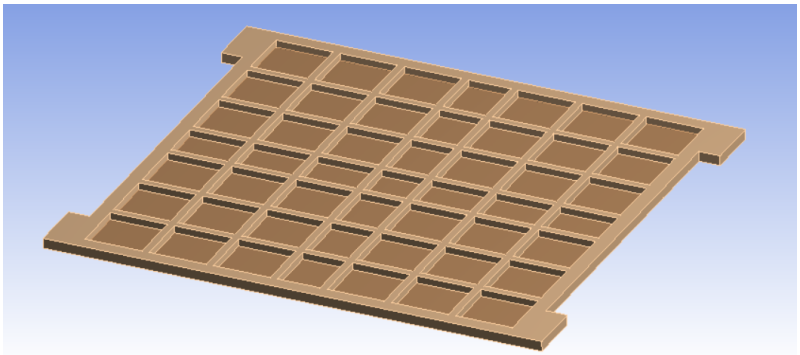

Figure 4.43: Supporting grid - FEM

Between the grid and the cut depth previously referred to, there is a thin aluminum layer left for heat conduction. The new model is shown below.

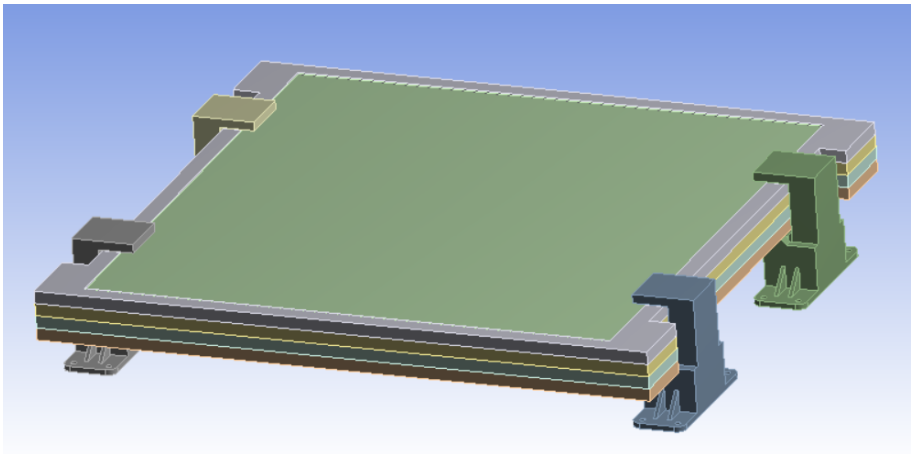

Figure 4.44: Final model

The previous analyses were performed on the new model, now analyzing only loadings in the out-of-plane axis which showed to be the critical one. The plates are connected together by revolute joints as before, bonded contact is defined between the supports and the plates, and frictional contact is defined between the areas of the plate that are contacting each other. Based on [68], a frictional coefficient for the aluminum-aluminum interfaced was chosen to be 1.03. In the case-case of the quasi-static analysis, the frictional contact led to the non-convergence of the analysis. The contact was changed to bonded for simplification purposes, assuming the relative plate sliding is negligible.

Each analysis result is presented hereafter. Quasi-static maximum deformation can be found in figure 4.45. As will be seen later in comparison to the maximum stress achieved in other analyses, these fall below, therefore they are not representative of the maximum acceleration achieved by the model, even when using the MAC curve values.

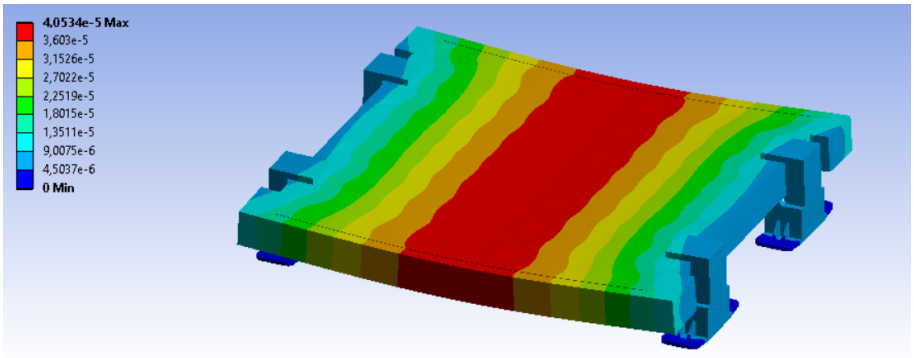

Figure 4.45: Quasi-static Deformation - Final Model

The harmonic or sine-sweep analysis revealed no resonance as expected since the first natural frequency is out of the input spectrum frequency range. It was found during iterations that, if the first natural frequency is close to the upper limit of the input frequency range, 100 Hz in this case, then some application is seen around that frequency value, which can be detrimental to the structure therefore, the further away the better. Results can be found below.

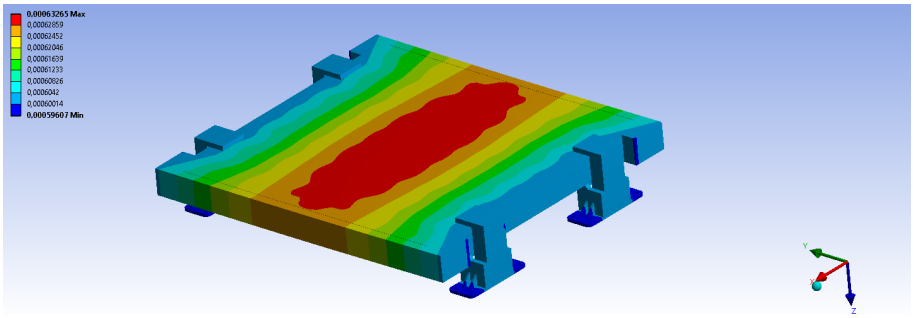

Figure 4.46: Harmonic analysis maximum deformation - Final Model

Random analysis was once again the critical one stress-wise. The acceleration and displacement PSD and maximum deformation are reported below.

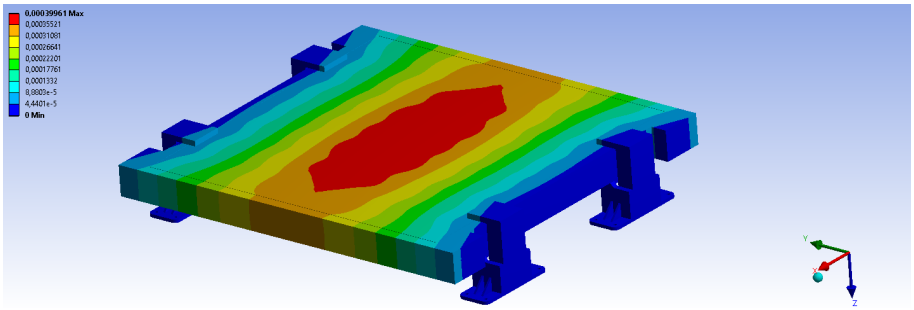

Figure 4.47: RVA 3σ deformation - Final model

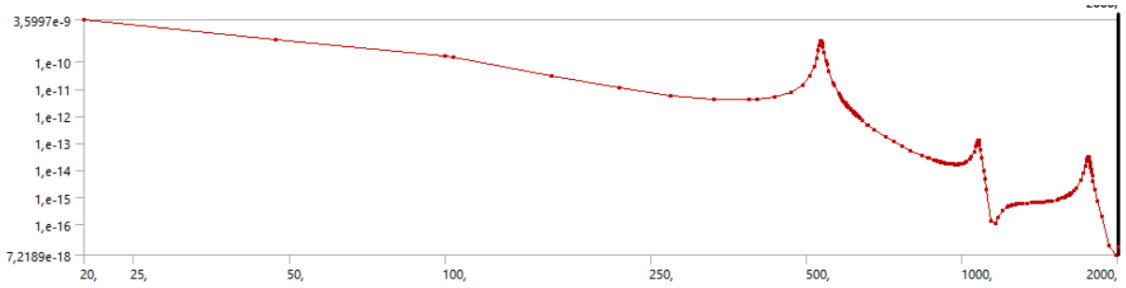

Figure 4.48: RVA Deformation PSD

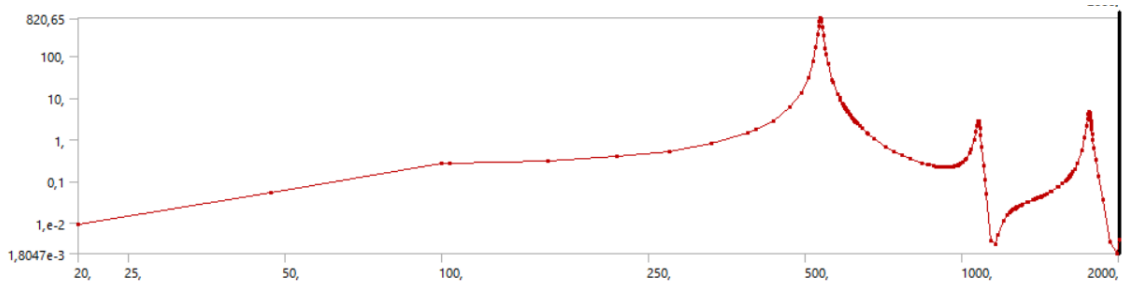

Figure 4.49: RVA Acceleration PSD

Regarding the acceleration PSD, we see a big spike around the first natural frequency, where a 0.24 g^2/Hz generates around 800 g^2/Hz, this is due to the fact that low damping is used and the first natural frequency is very high. If we look at Mile's equation, an approximation to calculate spikes in PSDs, which is:

$$PSD_{out,peak} = 3 \cdot \sqrt{\frac{\pi}{2} f_n Q \cdot (PSD_{in})}$$

where 3 is for 3σ values, f_n is the natural frequency of interest, Q represents the damping and PSD_{in} in the input PSD at the region of interest. One can see that the higher the frequency, the higher the peak. This is an approximation that considers that the majority of effective masses are concentrated in one main mode which is not the case, therefor using the equation to calculate the value of the peak will not work, it was just for the sake of understanding. The value of G_rms is around 120g explaining why the quasi-static acceleration of 40g is not critical.

In this particular analysis, and later found to be common to the others, stress singularities arose from contact boundaries and sharp edges. With the increase in mesh density, the stresses at that region kept increasing without reaching a plateau, a sign of stress concentrations. These areas increase the maximum stress level found in the analyses and one of them is shown below, while the others occur at the places indicated below in the panels' bottom view.

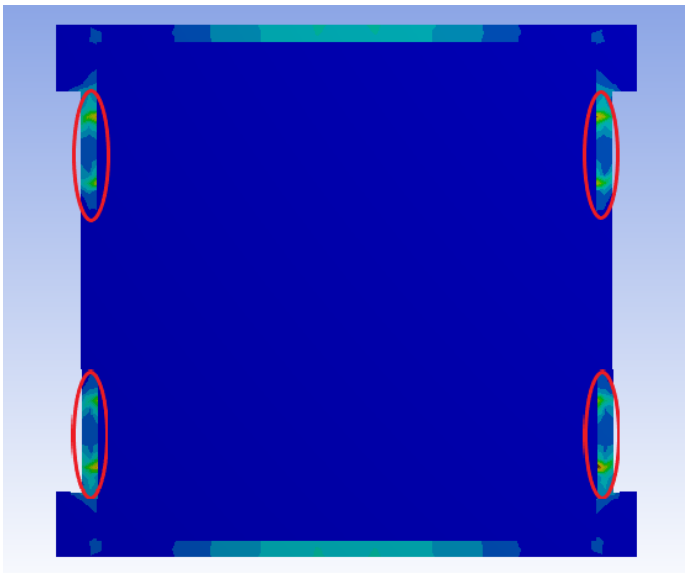

Figure 4.50: Regions of stress concentration

After analyzing the model it was found that the areas of stress concentrations were negligible when compared to the model's overall dimension. To check this it is possible to discard stress levels above a certain value and see the remaining volume. In the case of the random analysis, displaying a max stress of 95 MPa with 5 mm elements, by defining the threshold to around 75 MPa (limit stress of the aluminum when accounting for the safety factors) one can see the amount of removed elements around areas below.

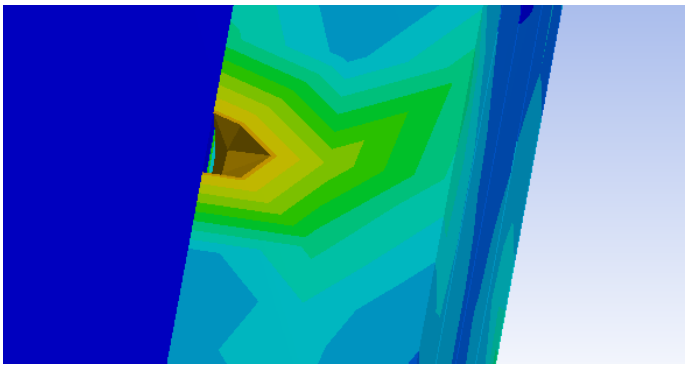

Figure 4.51: Removed elements from stress concentration at MOS = 0

Regarding the other analyses, the maximum value was maintained for the MOS since it is not critical. It is common practice to do the analysis away from the stress singularities. An analysis of the structure, discarding the stress concentrations would increase the MOS thus as will be seen the structure still has a margin to improve and reduce the mass.

4.2.10 Margins of safety final model

Finally, as before, the margins of safety were calculated. Prior to that the maximum results for every analysis will be presented, this time considering only loads in the out-of-plane direction.

Table 4.20: Final model values of stress and deformation

Analysis	Max Y deform. [mm]	S_X [Mpa]	S_Y [Mpa]	Aluminum [Mpa]
QS - 40g	0.0405	1.622	0.863	15.4
Sine 5-20 Hz	0.257	2.272	1.494	27
Sine 20-100 Hz	0.03658	0.81815	0.6398	8.172
Random	0.3996	8.9209	7.6973	24.665

From the previous values, the margins of safety can now be calculated.

Table 4.21: MOS, Yield, and Ultimate for Aluminum Plate X and Plate Y

Analysis	Yield (Aluminum)	Ultimate (Aluminum)	(Plates S_X)	(Plates S_Y)
QS - 40g	5.69	20.64	28.26	3.92
Sine 5-20 Hz	2.82	1.81	14.45	15.90
Sine 20-100 Hz	11.61	8.27	41.90	38.47
Random	3.18	2.93	2.28	2.07

4.2.11 Final model discussion

The results from the last model were satisfactory. The objective was to create a structure that would handle the loads and this was accomplished with some margin for improvement. The use of fin-like structures on the back of the panels leads to an increase in the rigidity of the substrate but also, was an easier-to-create design from an assembly/manufacturing standpoint since the plate just needs to be machined without major complications, very different from the previous model where the stiffeners and frame could pose some difficulties and increase the number of parts. The thickness of aluminum left between the SAR plates and the fins will help with heat conduction. In terms of possible improvements, further analyses should be pursued to evaluate the optimum thickness of the fins and boarders to save on weight while still maintaining structural rigidity. This should be possible because the final model's lowest margin of safety was 2.07, while most designs strive to have a MOS close to zero avoiding unnecessary mass. This type of work was not performed on this Thesis for two main reasons, one was time restrictions and the other because

of the uncertainty in the input loads and SAR material properties. With proper loads, properties, and a validated model, this iteration work can be done to achieve optimum configuration. Finally, again due to time restrictions, the simulation of the final model's deployed configuration, more specifically its modal analyses was not possible, but from the first model, it is possible to estimate that its first natural frequency is above 1 Hz since the difference in mass of the two models is not so big and in this new model, if the cable is used on the tip of the plates to control the deployment and is tensioned after latching of the panels it also increases the deployed mechanisms first natural frequency.

Chapter 5

Conclusions and future work

To conclude the work here presented, a final review of the major subjects and findings of each chapter will help to have a retrospective and understand better the sequence of this research.

The work started by giving the reader the motives behind this work and how it will benefit the company. As was said Tekever wants to demonstrate their technology in space and so proposed the present work to design mechanisms capable of being rigid and sustaining launch load while stowed to the open into an array of SAR panels for image capturing. Other requisites from an operation standpoint were for the mechanism to be retractable and lightweight. All these requirements, as well as the structural ones, that will be mentioned afterward, are part of the thought process throughout the design and influence most of the design decisions. Then it was important to introduce the reader to the space environments and how they can impact the structure. These issues, like the presence of atomic oxygen attack, vacuum and subsequent outgassing of certain substances from the material, radiation, and thermal cycling influenced not only the material choice but the structure and mechanism itself. The selection of materials that could resist these effects or at least sustain operations for the intended time was paramount highlighting the selection of usual aerospace aluminum alloys that enabled the structure to be lightweight while reasonably strong. It is convenient to expose here the possibility of in the future using composite or sandwich materials. The use of sandwich material for the panel's substrate is common use in solar panels and would be an interesting opportunity to research in the future for major weight savings. This section is followed by a review of the types of analyses that are common, that in fact mimic or envelop the loads experienced during ascendance within the rocket and are the foundation of structural analyses. The reader is exposed to the concepts, considerations, and mathematics behind the analyses as well as load specifications for the present project. These loads

were obtained from ESA's handbook on structural analyses and given from other projects, which is good for preliminary sizing but is not sufficient for detailed design. Future specifications for this specific project should be obtained by the company or calculated once the satellite model is in existence.

After some base knowledge of the assumptions to be present prior to the design and some established requirements, the design of the mechanisms was executed. The design involved a great number of ideas, iterations, and trade-offs. The usual design of deployable panels involves some mechanisms that when deployed, lock in positions and stays that way throughout the mission, but the proposed mechanisms had to be retractable and synchronous. This posed several problems that discarded many of the initial ideas but, supported by the company's colleagues and supervisor, two designs were conceived which represent proposals to satisfy all the requirements. The pantograph and the closed cable loop mechanisms guarantee synchronization, inherent in the case of the pantograph and obtained by close loop cable in the case of the second mechanism, can be controlled by the motor, and are both retractable. After a comparison of the two the closed cable loop was chosen as it was lighter and did not suffer as much from thermal issues. A prototype should be cheap to manufacture and testing is advised since not only for validation of posterior finite element analyses but also to guarantee proper deployment minimizing failure possibility, with special attention to cable slipping and undertension.

Having chosen the mechanism to proceed in the design sequence, structural analyses helped to improve the mechanism's overall design. Starting with a crude design that posed some manufacturing and assembly issues and that could not sustain the input spectrum of loads, an improvement and iterative process was started which culminated in a final design capable of sustaining the loads and much easier to manufacture and assemble turning out to be very satisfactory. Due to time restrictions and lack of a specific load for the project, the design was left oversized and has now to go through validation and iterations with proper load cases to achieve the final model optimized for the mission. To do so, a reduction in the plate's thickness is proposed as it is more than enough for these loads which should already be conservative. The grid design on the back allows having a lighter plate while maintaining proper rigidity, and it is recommended to keep the plate on top of each other with no gap and make use of the advantage it gives rigidity-wise. In the end, although there was more that was wanted to be added to the research, it turned out to be satisfactory, creating a ground base for future work and hopefully helping the company achieve the feat of launching a Portuguese satellite into space.

As for future work and to guarantee a well-defined mechanism one should take a step back and input proper SAR plate material properties obtained from the supplier and have proper loading conditions. After acquiring these, a simple prototype

should be built to validate the finite element analysis particularly because of the applied boundary conditions and damping. The final model should now go through an iterative process to save on mass, reduction of plate thickness is a possibility that should be investigated. A different analysis from the one presented in this document that should be tested is bolt analyses, this will help size the screws and their respective applied torque or pretension, which is paramount for securing all in place during the flight. After having a structure that resists flight loads the deployed configuration should be investigated and reinforced if needed to guarantee the requirements' first natural frequency. This should pose no problem since a mass reduction will lead to an increase in natural frequency in this case. Afterward, a motion simulation should be performed to access deployment-rated and size motorization and torsional springs. The prototype deployment should be compared to the previous simulation and possible tuning and failure areas identification is paramount to have a proper real-world working mechanism. As can be seen, a lot of work is involved to conceive such a structure but this work should serve to help give guidelines on the work to come.

Appendix A

Structural analysis additional information and material

A.1 Comparison between first simplified and detailed model

The natural frequency comparison between the two models presented previously in this thesis is displayed below.

Detailed model	Simple model	Relative error
59.80	58.91	0.0150
60.61	59.97	0.0107
63.19	62.46	0.0116
64.60	64.33	0.0042
99.50	98.76	0.0074
100.05	99.48	0.0057
115.79	119.84	0.0350
139.02	132.49	0.0470
162.74	160.71	0.0125
164.70	162.30	0.0146
168.49	168.51	0.0001
171.90	172.32	0.0024
195.83	195.15	0.0035
195.94	195.28	0.0034
202.82	201.55	0.0063
204.77	204.04	0.0036
247.34	266.95	0.0793
282.50	281.08	0.0050
283.15	281.78	0.0048
303.61	307.26	0.0120
312.56	309.33	0.0103
321.20	330.57	0.0292
325.48	332.80	0.0225
332.75	336.47	0.0112
345.74	347.72	0.0057
354.82	355.29	0.0013
354.94	355.40	0.0013
363.54	364.24	0.0019
367.82	368.97	0.0031
383.27	382.37	0.0023
396.87	407.65	0.0272
406.65	425.09	0.0453
422.89	425.25	0.0056
425.68	432.48	0.0160
425.79	434.63	0.0208
432.83	471.90	0.0903
438.92	485.81	0.1068
469.22	491.08	0.0466
479.18	510.07	0.0645
483.65	526.27	0.0881

Figure A.1: Detailed vs simple model mode comparison

A.2 Modal convergence - first model

The first model mesh convergence for modal analysis using second elements is displayed in this section. The relative error is calculated between iterations. Here it can be noticed that more modes appear as the number of elements increases, as would be expected, therefore the comparison between iterations is not exact until a certain point where no more modes appear but it is still a good way to grasp the convergence.

100	50	Rel.error	25	Rel.error	12.5	Rel.error	6	Rel.error	3	Rel.error
61.168	58.734	4.14%	58.602	0.23%	58.584	0.03%	58.58	0.01%	58.58	0.00%
62.436	59.778	4.45%	59.652	0.21%	59.635	0.03%	59.632	0.01%	59.631	0.00%
68.216	62.295	9.50%	62.15	0.23%	62.128	0.04%	62.123	0.01%	62.122	0.00%
70.495	64.13	9.93%	64.005	0.20%	63.986	0.03%	63.981	0.01%	63.98	0.00%
133.34	99.447	34.08%	98.353	1.11%	98.335	0.02%	98.333	0.00%	98.332	0.00%
136.63	100.25	36.29%	99.066	1.20%	99.044	0.02%	99.04	0.00%	99.039	0.00%
169.34	127.34	32.98%	120.3	5.85%	114.82	4.77%	113.61	1.07%	113.19	0.37%
185.2	139.9	32.38%	132.92	5.25%	127.51	4.24%	126.33	0.93%	125.88	0.36%
188.9	159.97	18.08%	158.66	0.83%	158.54	0.08%	158.52	0.01%	158.52	0.00%
191.37	161.62	18.41%	160.29	0.83%	160.15	0.09%	160.13	0.01%	160.13	0.00%
195.92	167.56	16.93%	166.2	0.82%	166.09	0.07%	166.07	0.01%	166.06	0.01%
202.81	171.4	18.33%	170.02	0.81%	169.9	0.07%	169.88	0.01%	169.88	0.00%
234.24	200.33	16.93%	193.5	3.53%	193.35	0.08%	193.34	0.01%	193.34	0.00%
237.93	200.55	18.64%	193.63	3.57%	193.48	0.08%	193.47	0.01%	193.47	0.00%
293.62	203.92	43.99%	199.27	2.33%	199.15	0.06%	199.14	0.01%	199.14	0.00%
300.26	206.78	45.21%	201.7	2.52%	201.57	0.06%	201.56	0.00%	201.56	0.00%
311.77	280.57	11.12%	268.6	4.46%	259.47	3.52%	258.19	0.50%	257.71	0.19%
401.17	306.44	30.91%	278.15	10.17%	277.72	0.15%	277.7	0.01%	277.7	0.00%
417.78	307.57	35.83%	278.84	10.30%	278.4	0.16%	278.38	0.01%	278.38	0.00%
441.76	307.66	43.59%	300.93	2.24%	300.37	0.19%	300.3	0.02%	300.29	0.00%
445.1	309.49	43.82%	302.64	2.26%	302.05	0.20%	301.98	0.02%	301.97	0.00%
467.68	331.47	41.09%	323.2	2.56%	321.25	0.61%	319.79	0.46%	319.14	0.20%
489.12	336.54	45.34%	328.03	2.59%	323.4	1.43%	322.86	0.17%	322.75	0.03%
498.19	356.49	39.75%	333.46	6.91%	327.49	1.82%	327.41	0.02%	327.4	0.00%
503.62	368.99	36.49%	348.9	5.76%	333.79	4.53%	330.94	0.86%	329.88	0.32%
532.88	370.19	43.95%	349.03	6.06%	348.19	0.24%	348.15	0.01%	348.15	0.00%
630.99	372.17	69.54%	349.32	6.54%	348.31	0.29%	348.27	0.01%	348.27	0.00%
689.72	372.65	85.09%	355.96	4.69%	355.32	0.18%	355.28	0.01%	355.27	0.00%
694.29	377.14	84.09%	360.58	4.59%	359.88	0.19%	359.83	0.01%	359.82	0.00%
712.71	413.69	72.28%	383.42	7.89%	366.12	4.73%	362.7	0.94%	361.33	0.38%
763.19	444.11	71.85%	408.55	8.70%	389.63	4.86%	386.	0.94%	384.54	0.38%
801.48	477.56	67.83%	418.38	14.15%	417.03	0.32%	416.98	0.01%	416.98	0.00%
816.02	486.75	67.65%	418.53	16.30%	417.18	0.32%	417.13	0.01%	417.12	0.00%
836.22	489.68	70.77%	424.41	15.38%	423.12	0.30%	423.07	0.01%	423.06	0.00%
894.27	491.06	82.11%	426.5	15.14%	425.13	0.32%	425.06	0.02%	425.06	0.00%
901.45	493.72	82.58%	460.33	7.25%	458.84	0.32%	458.65	0.04%	458.62	0.01%
964.54	496.71	94.19%	472.37	5.15%	470.64	0.37%	470.42	0.05%	470.01	0.09%
1005.9	517.67	94.31%	488.46	5.98%	473.72	3.11%	470.96	0.59%	470.38	0.12%
1045.3	558.64	87.12%	510.67	9.39%	488.3	4.58%	483.95	0.90%	482.22	0.36%
1094.7	574.32	90.61%	525.83	9.22%	521.62	0.81%	520.97	0.12%	520.79	0.03%
1142.7	589.47	93.85%	539.06	9.35%	536.53	0.47%	536.34	0.04%	536.33	0.00%
1154.2	609.03	89.51%	548.13	11.11%	545.04	0.57%	544.95	0.02%	544.94	0.00%
1192.9	619.03	92.70%	548.87	12.78%	545.74	0.57%	545.65	0.02%	545.64	0.00%

Figure A.2: Convergence relative error calculation - first model quadratic elements (continues next page)

		#DIV/0!	2118.4	######	1977.	7.15%	1969.7	0.37%	1969.3	0.02%
		#DIV/0!	2173.	######	1982.8	9.59%	1976.2	0.33%	1975.7	0.03%
		#DIV/0!	2173.3	######	1991.3	9.14%	1983.8	0.38%	1982.2	0.08%
		#DIV/0!	2180.3	######	2008.3	8.56%	1990.8	0.88%	1986.8	0.20%
		#DIV/0!	2180.7	######	2053.5	6.19%	2046.	0.37%	2045.6	0.02%
		#DIV/0!	2185.1	######	2053.5	6.41%	2046.	0.37%	2045.6	0.02%
		#DIV/0!	2189.5	######	2054.1	6.59%	2047.8	0.31%	2047.5	0.01%
		#DIV/0!	2191.1	######	2062.2	6.25%	2055.3	0.34%	2054.9	0.02%
		#DIV/0!	2201.6	######	2091.3	5.27%	2089.1	0.11%	2084.1	0.24%
		#DIV/0!	2201.9	######	2104.3	4.64%	2089.9	0.69%	2088.2	0.08%
		#DIV/0!	2237.9	######	2114.9	5.82%	2094.2	0.99%	2089.2	0.24%
		#DIV/0!	2301.9	######	2171.9	5.99%	2164.	0.37%	2163.6	0.02%
		#DIV/0!	2343.4	######	2171.9	7.90%	2164.	0.37%	2163.6	0.02%
		#DIV/0!	2380.2	######	2184.5	8.96%	2177.3	0.33%	2176.9	0.02%
		#DIV/0!	2384.	######	2187.2	9.00%	2179.9	0.33%	2179.5	0.02%
		#DIV/0!	2398.8	######	2188.	9.63%	2181.8	0.28%	2181.6	0.01%
		#DIV/0!	2399.1	######	2188.	9.65%	2181.9	0.28%	2181.6	0.01%
		#DIV/0!	2424.5	######	2195.2	10.45%	2189.3	0.27%	2189.1	0.01%
		#DIV/0!	2451.9	######	2195.4	11.68%	2189.5	0.27%	2189.3	0.01%
		#DIV/0!	2452.7	######	2240.6	9.47%	2215.9	1.11%	2208.7	0.33%
		#DIV/0!	2455.3	######	2257.4	8.77%	2248.6	0.39%	2245.7	0.13%
		#DIV/0!	2485.7	######	2301.	8.03%	2289.9	0.48%	2289.2	0.03%
					2307.6		2296.8	0.47%	2296.2	0.03%
					2309.3		2298.6	0.47%	2297.9	0.03%
					2326.7		2313.3	0.58%	2309.1	0.18%
					2339.9		2330.9	0.39%	2324.7	0.27%
					2340.		2331.1	0.38%	2330.6	0.02%
					2347.8		2331.7	0.69%	2330.7	0.04%
					2356.8		2348.6	0.35%	2348.2	0.02%
					2358.1		2349.9	0.35%	2349.5	0.02%
					2410.3		2396.7	0.57%	2395.9	0.03%
					2410.3		2396.7	0.57%	2395.9	0.03%
					2413.9		2401.2	0.53%	2400.5	0.03%
					2424.5		2411.3	0.55%	2402.5	0.37%
					2445.9		2415.4	1.26%	2410.5	0.20%
					2450.9		2433.2	0.73%	2425.	0.34%
					2450.9		2437.1	0.57%	2432.4	0.19%
					2452.		2437.1	0.61%	2436.3	0.03%
					2458.7		2438.	0.85%	2436.3	0.07%
					2471.3		2445.4	1.06%	2440.1	0.22%
					2472.2		2449.	0.95%	2445.1	0.16%
					2480.6		2469.7	0.44%	2469.	0.03%
					2490.2		2481.3	0.36%	2481.	0.01%
					2490.2		2481.3	0.36%	2481.	0.01%

Figure A.3: Convergence relative error calculation - first model quadratic elements

A.3 Rigid body modes - first model

The rigid body modes retrieved from the first model which frequencies are used in the rigid body modes check are displayed. The first elastic mode can be consulted in the next section.

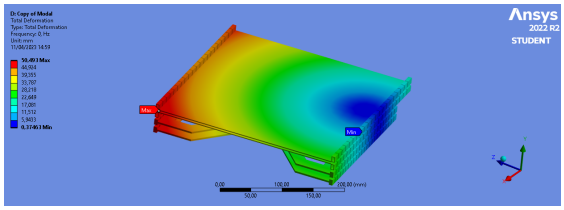

Figure A.4: RBM 1

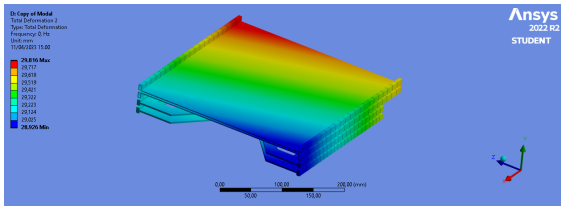

Figure A.5: RBM 2

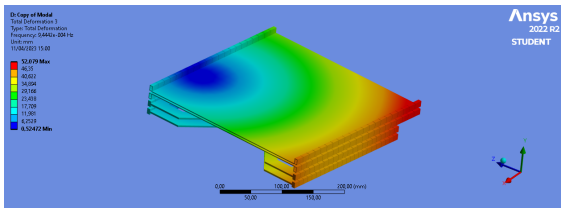

Figure A.6: RBM 3

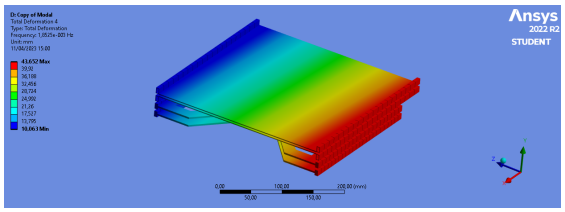

Figure A.7: RBM 4

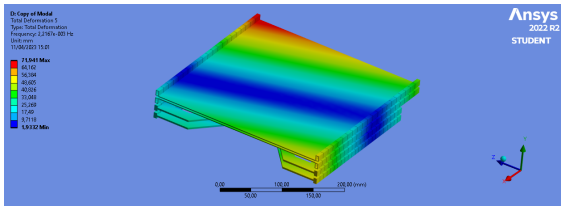

Figure A.8: RBM 5

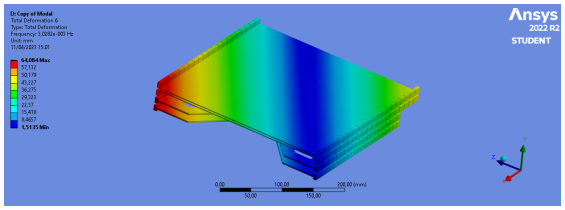

Figure A.9: RBM 6

A.4 First model - First ten modes

Here are the representations of the first ten natural modes of the first model to better understand the behavior of the structure.

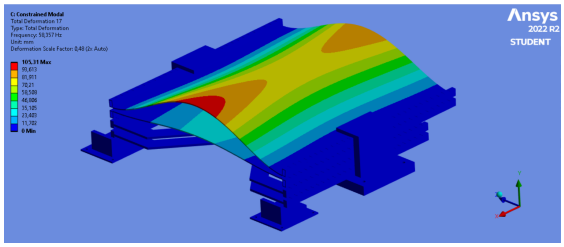

Figure A.10: Mode 1

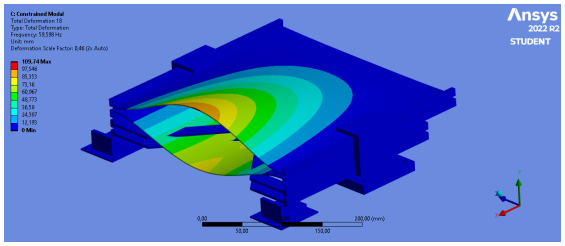

Figure A.11: Mode 2

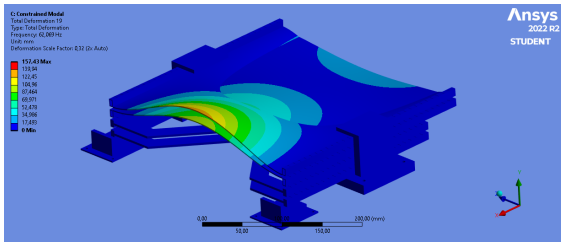

Figure A.12: Mode 3

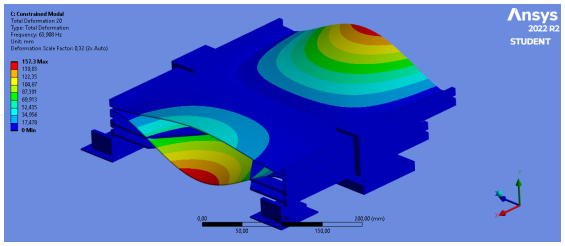

Figure A.13: Mode 4

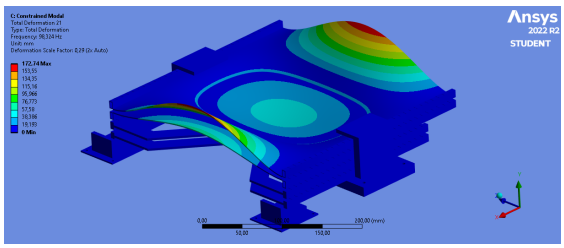

Figure A.14: Mode 5

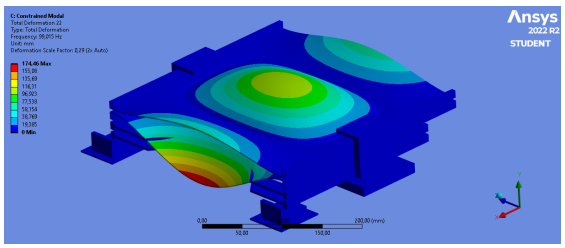

Figure A.15: Mode 6

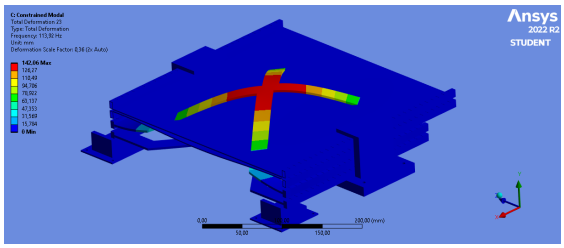

Figure A.16: Mode 7

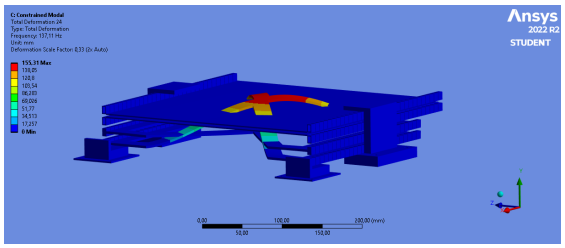

Figure A.17: Mode 8

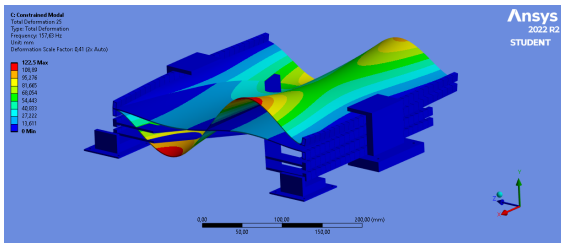

Figure A.18: Mode 9

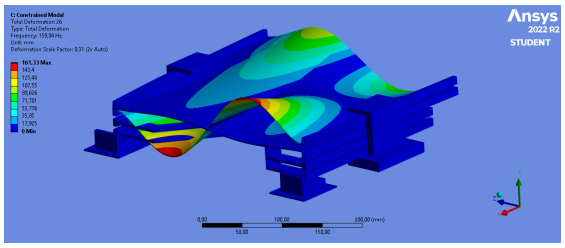

Figure A.19: Mode 10

A.5 Second model - first ten modes

Below one can see the first ten modes of the reinforced second model. It is possible to see the influence of the stiffeners on the panel's behavior and on the increase in natural frequencies.

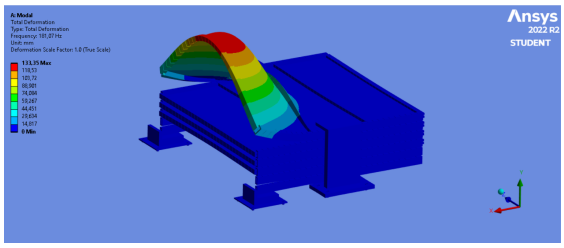

Figure A.20: Mode 1

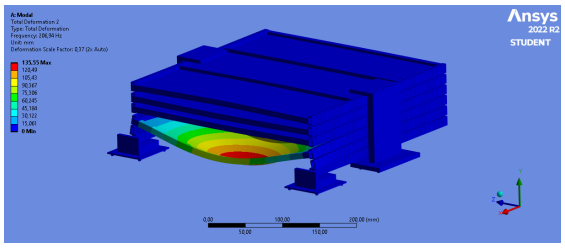

Figure A.21: Mode 2

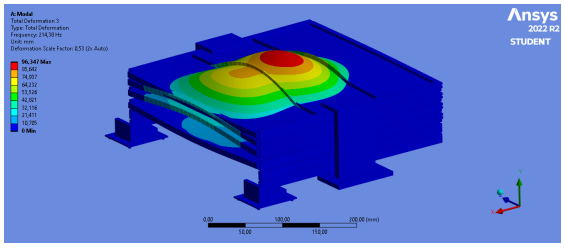

Figure A.22: Mode 3

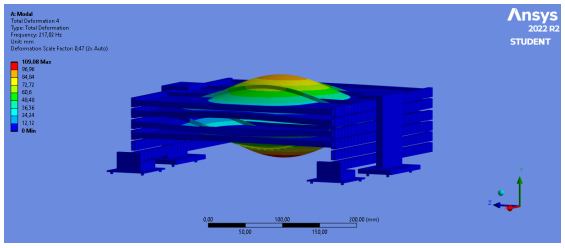

Figure A.23: Mode 4

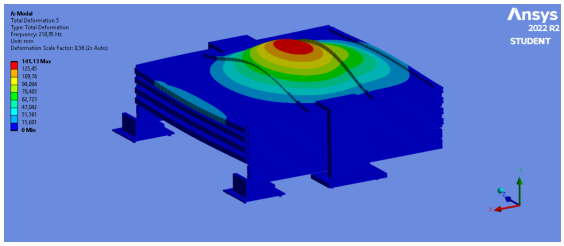

Figure A.24: Mode 5

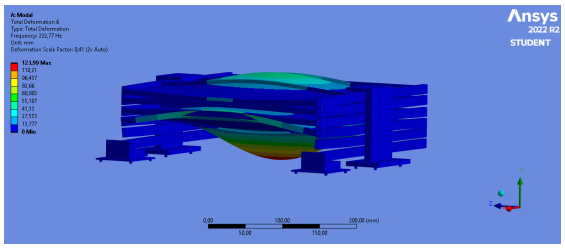

Figure A.25: Mode 6

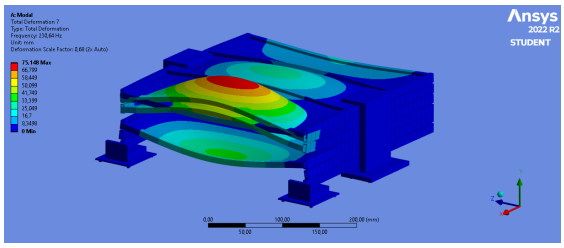

Figure A.26: Mode 7

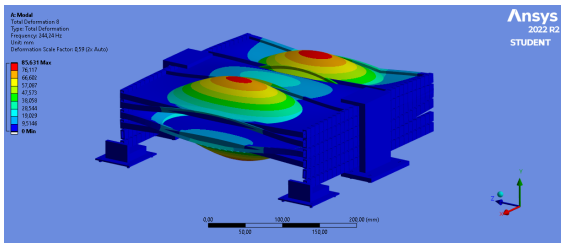

Figure A.27: Mode 8

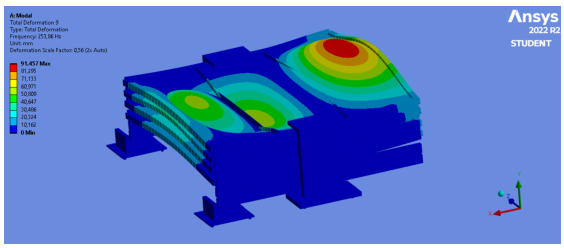

Figure A.28: Mode 9

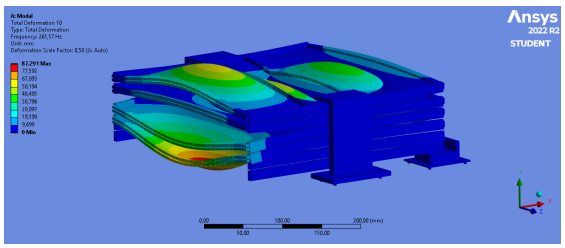

Figure A.29: Mode 10

A.6 Final model - first ten modes

The first ten modes of the final model are here presented. The increase in frequency is easily noticeable. It is also perceivable that the panels are now so rigid that the modes also include the supports. With the refinement of the model removing some mass, this should not happen, otherwise, the supports may need an increase in rigidity.

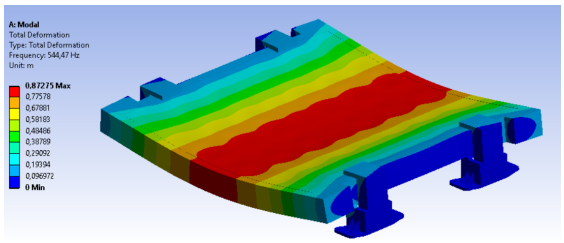

Figure A.30: Mode 1

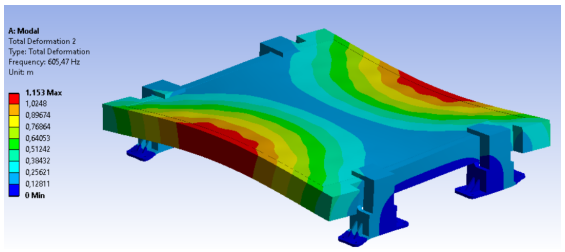

Figure A.31: Mode 2

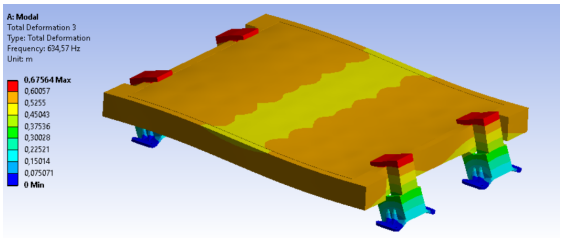

Figure A.32: Mode 3

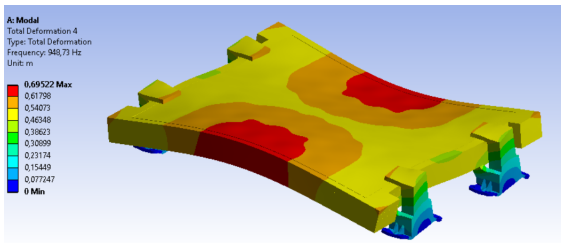

Figure A.33: Mode 4

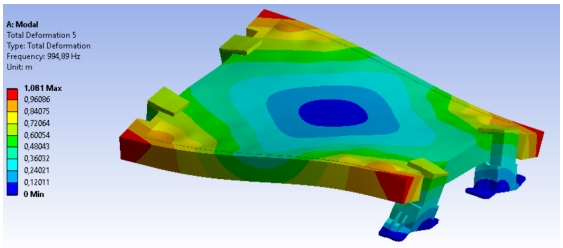

Figure A.34: Mode 5

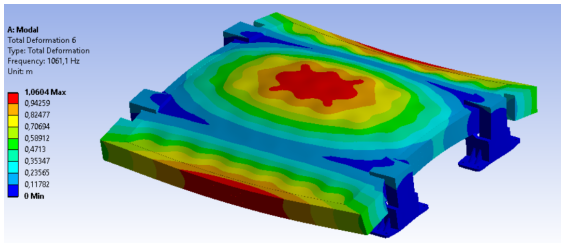

Figure A.35: Mode 6

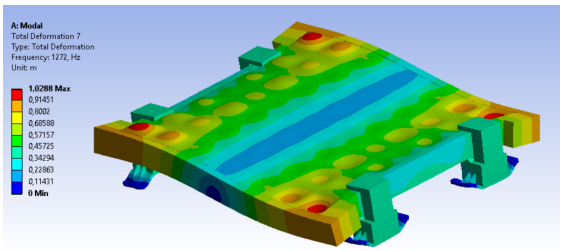

Figure A.36: Mode 7

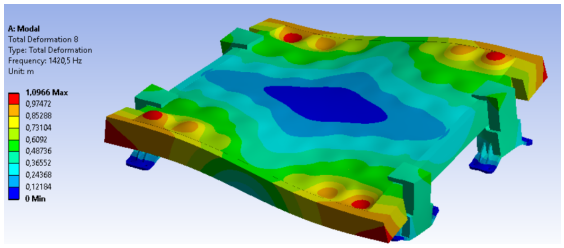

Figure A.37: Mode 8

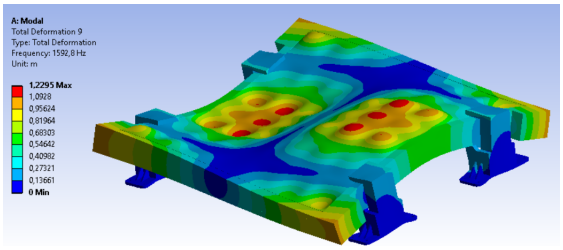

Figure A.38: Mode 9

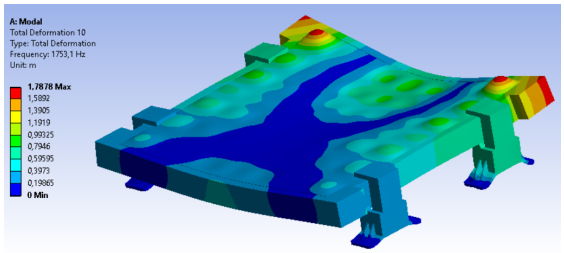

Figure A.39: Mode 10

A.6. Final model - first ten modes

Appendix B

Literature review additional information

B.1 Environmental effects

Atomic oxygen weight loss properties of metal and the outgassing rate of polymers used in space applications are here presented to grasp which materials are best or worst suited for this field.

Sample	Tray (°C)	Δm (mg, ±0.02)	Δm (mg/cm², ±0.03)	α_i (±0.01)	α_f (±0.01)	ε_i (±0.01)	ε_f (±0.01)
Copper	60	−0.03	−0.042	0.49	0.56	0.01	0.03
	120	−0.07	−0.098	0.47	0.52	0.02	0.03
Gold	120	+0.01	+0.014	0.19	0.18	0.02	0.02
Nickel	60	−0.05	−0.071	0.33	0.34	0.02	0.02
	120	−0.05	−0.071	0.33	0.31	0.02	0.02
Niobium	60	−0.05	−0.071	0.33	0.34	0.03	0.03
		−0.03	−0.042	0.33	0.34	0.03	0.03
Silver	120	+0.23	+0.323	0.11	0.80	0.01	0.46
Tantalum	60	−0.05	−0.071	0.38	0.39	0.03	0.02
	120	−0.01	−0.014	0.38	0.37	0.03	0.02
Tungsten	60	−0.15	−0.210	0.46	0.48	0.02	0.02
	120	−0.02	−0.028	0.46	0.46	0.02	0.02
	200	−0.04	−0.051	0.46	0.55	0.02	0.01
Vanadium	60	−0.42	−0.589	0.68	0.70	0.06	0.05
	120	−0.04	−0.051	0.64	0.66	0.06	0.06
Aluminum/ Lithium	60	−0.51	−0.155	0.15	0.14	0.05	0.05
	120	−0.53	−0.162	0.15	0.14	0.05	0.05
Weldalite (Passive)		−0.15	−0.090	0.13	0.15	0.05	0.05
		−0.17	−0.102	0.13	0.13	0.06	0.05

α=absorptance, ε=emittance, ε_i=initial, ε_f=flight,

Table B.1: Atomic oxygen weight loss for metals. Taken from [15]

Sample	STS–5	STS 41–G	LDEF	STS–46	PPPL	MSFC
Halar (bulk)		1.0–2.0	2.1	2.0–2.5	3.0–3.4	0.014–0.034
Lexan®		1.3–3.6		3.6–4.0		
PEEK (bulk)		4.7	2.3	2.0–4.0		
Tefzel		0.20		≈1.0	2.8–3.0	0.11–0.12
Kapton® HN		3.3		3.3–4.3		
Kapton® H	3.0			3.5–3.9		
Black Kapton®				2.1–2.7	3.4	
TFE	<0.05		0.20	0.049–0.080		
FEP	<0.05	3.1–2.4	0.35	0.082–0.082	5.9–6.6	0.023

Table B.2: Polymer atomic oxygen rating based on space missions for commonly used polymers (Higher meaning better suited). Taken from [15]

B.2 Boundary element and Statistical Energy analysis

Different from random vibrations, vibroacoustic analysis deals with loads generated by acoustic excitation of the structure, its objectives being the assessment of the strength and life of structures particularly sensitive to the acoustic environment and to predict random vibration (RV) environments for spacecraft components. Sensitive excited structures can transmit RVs to the rest of the spacecraft. To perform these analyses two common methods are employed, mixed Boundary element/Finite element analysis and Statistical Energy analysis.

Boundary Element Method (BEM) differs from the FEM. While the former takes BCs into account in an exact manner and solves the governing differential equations approximately, the BEM is the opposite, it solves the differential equations exactly but approximates the boundary conditions. It uses Green's formulation and only applies the elements at the boundary but the resultant matrices are not banded like in the finite element method after assembly, we have instead a full matrix entailing a greater computational effort. Thus there are benefits in performing a hybrid analysis, employing the FEM in the structure and the BEM at the boundary. Since the BEM only discretizes the wetted surface, it uses way fewer elements than the FEM for the same purpose, which would need to discretize the whole acoustic space, and simulating an "infinite" acoustic space would be computationally impossible.

The general formulation for the pressure field at the boundary is given by the following integral:

$$\rho\omega^2 w(x,y) = -\frac{1}{4\pi}\int\int_{surf} \Delta p(\xi,\eta,k)\frac{\partial}{\partial z}\frac{e^{jkR}}{R}d\xi d\eta \tag{B.1}$$

In this formulation an acoustic plane wave can be simulated having R taking a

big value (remote source), as a rule of thumb [50] recommends that for a structure of dimension in the order of a meter, a R of at least 1km is recommended. To approximate a diffuse field (same energy in all directions) "n" sources may be superposed.

Below a depiction of the steps of the method can be seen.

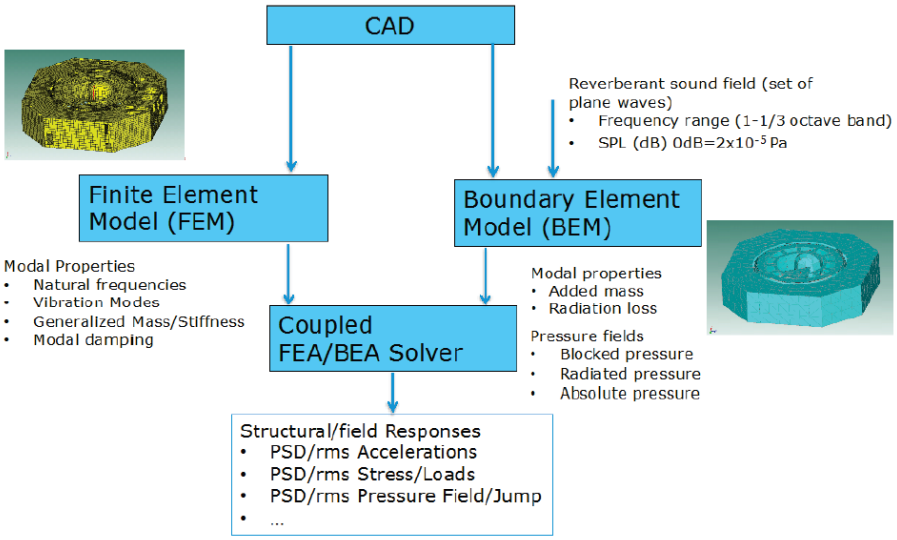

Figure B.1: A flow chart on BE/FE coupled analysis

When the frequency range increases Statistical Energy Analysis (SEA) is best suited for this type of environment. It starts by recognizing that the energy transferred between two bodies subjected to uncorrelated random excitation is proportional to the difference in energy between the two. The method is based on calculating the power between components by analyzing the low-detail subsystem. The latter is the fundamental element of SEA and is a group of similar energy storage blocks $< E_i >$

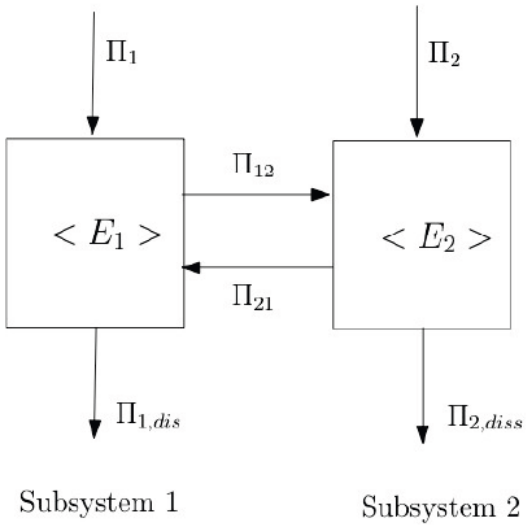

Figure B.2: A two sub-system statistical analysis representation

In the above, Π_i is the input power to the subsystem i, Π_{ij} is the transmitted energy from i to j and $\Pi_{i,diss}$ is the dissipated energy by damping. These referred quantities are expressed in the below equilibrium equations.

$$\begin{aligned} \Pi_1 &= \omega\eta_1 < E_1 > +\omega\eta_{12}n_1 \left[\frac{< E_1 >}{n_1} - \frac{< E_2 >}{n_2}\right] \\ \Pi_2 &= \omega\eta_2 < E_2 > +\omega\eta_{21}n_2 \left[\frac{< E_2 >}{n_2} - \frac{< E_1 >}{n_1}\right] \end{aligned} \tag{B.2}$$

References

[1] Ellerbeck S. The space economy is booming. what benefits can it bring to earth? 2022. URL: https://www.weforum.org/agenda/2022/10/space-economy-industry-benefits/.

[2] Brukardt R. How will the space economy change the world? 2022. URL: https://www.mckinsey.com/industries/aerospace-and-defense/our-insights/how-will-the-space-economy-change-the-world.

[3] Signé L, Dooley H. How space exploration is fueling the fourth industrial revolution. 2023. URL: https://www.brookings.edu/blog/techtank/2023/03/28/how-space-exploration-is-fueling-the-fourth-industrial-revolution/.

[4] Ferrão F. Innov8rs. "espaço precisa de um ecossistema de inovação forte". 2023. URL: https://www.dinheirovivo.pt/iniciativas/innov8rs-espaco-precisa-de-um-ecossistema-de-inovacao-forte-16286157.html.

[5] Lee N, Pellegrino S. Packaging and deployment strategies for synthetic aperture radar membrane antenna arrays. 2014.

[6] Leipold M. Large sar membrane antennas with lightweight deployable booms. 2005. URL: https://www.researchgate.net/publication/224987516.

[7] Martin L. Synthetic aperture radar: "round the clock reconaissance". 2020. URL: https://www.lockheedmartin.com/en-us/news/features/history/sar.html.

[8] Engineering E, Wiki TH. Synthetic aperture radar. 2009. URL: https://ethw.org/Synthetic_Aperture_Radar.

[9] ETHW . Seasat I. 2009. URL: https://eospso.nasa.gov/missions/seasat-1.

[10] ESA . Low earth orbit. 2020. URL: https://www.esa.int/ESA_Multimedia/Images/2020/03/Low_Earth_orbit; accessed on 02 20, 2023.

References

[11] Dever JA. Low earth orbital atomic oxygen and ultraviolet radiation effect on polymers. 1991.

[12] Fortescue PW, Stark JPW, Swinerd G. Spacecraft systems engineering. 2011. ISBN 9780470750124.

[13] Finckenor MM, de Groh KK. A researcher's guide to: Space environmental effects. 2020.

[14] Grossman E, Gouzman I. Space environment effects on polymers in low earth orbit. 2003. doi:10.1016/S0168-583X(03)00640-2.

[15] Doofing D, Finckenor AMM. Material selection guidelines to limit atomic oxygen effects on spacecraft surfaces. 1999. URL: www.sti.nasa.gov.

[16] Sebestyen G, Fujikawa S, Galassi N, Chuchra A. Low Earth Orbit Satellite Design. 2018. URL: http://www.springer.com/series/6575.

[17] Jiao Z, Jiang L, Sun J, Huang J, Zhu Y. Outgassing environment of spacecraft: An overview. 2019. doi:10.1088/1757-899X/611/1/012071.

[18] Chiggiato P. Materials and properties iv - outgassing. 2017.

[19] Moshey E. A compilation of outgassing data on vacuum materials. 1982.

[20] Teichman LA, Stein BA. Nasa/sdio space environmental effects on materials workshop. 1988.

[21] Kiper G, Söylemez E. Deployable space structures. ISBN 9781424436286; 2009, p. 131–8. doi:10.1109/RAST.2009.5158183.

[22] Roberts EW. Space tribology: Its role in spacecraft mechanisms. 2012. doi:10.1088/0022-3727/45/50/503001.

[23] Kellermeier H, Roth M, Schneider K. The retractable ultra-lightweight (ulp) solar array for retrievable space platforms. 1984. doi:10.1108/eb035933.

[24] Brough Z, Paolini C. Advanced deployable/retractable solar panel system for satellite applications. 2015.

[25] Kam JD. Retractable advanced rigid array for solar space power. 1988.

[26] Vorlicek PL, Gore JV, Plescia CT. Design and analysis considerations for deployment mechanisms in a space environment. 1982.

[27] Shapiro W, Murray F, Howarth R, Fusaro R. Space mechanisms lessons learned volume ii literature review study. 1995.

[28] ESA . Dawn spacecraft. 2018. URL: https://solarsystem.nasa.gov/missions/dawn/technology/spacecraft/; accessed on 02 21, 2023.

[29] Straubel M, Hillebrandt M. Evaluation of different architectural concepts for huge deployable solar arrays for electric propelled space crafts. 2016. URL: https://www.researchgate.net/publication/312216793.

[30] Wang Y, Liang T, Congi Q, Liu R, Yang H. Satellite sar antenna deployable structure design and kinematic analysis. vol. 126. Atlantis Press; 2015,doi:10.2991/icismme-15.2015.204.

[31] A new deployment concept for a space based sar antenna. 2003.

[32] Wachholz JJ, Murphy DM. Scarlet I: Mechanization solutions for deployable concentrator optics integrated with rigid array technology. 1996.

[33] Fernandes P. Topology optimization of high-strain capable damage tolerant composite structures. 2022.

[34] Jeong JW, Yoo YI, Shin DK, Lim JH, Kim KW, Lee JJ. A novel tape spring hinge mechanism for quasi-static deployment of a satellite deployable using shape memory alloy. Review of Scientific Instruments 2014;85(2). URL: https://doi.org/10.1063/1.4862470. doi:10.1063/1.4862470; 025001.

[35] Puig L, Barton A, Rando N. A review on large deployable structures for astrophysics missions. Acta Astronautica 2010;67:12–26. doi:10.1016/j.actaastro.2010.02.021.

[36] Belvin WK, Straubel M, Wilkie WK, Zander ME, Fernandez JM, Hillebrandt MF. Advanced deployable structural systems for small satellites. 2016.

[37] Li Z, Han J, Zhang Y, Lu R, Yang Y. Research on forming and mechanical properties for one dimensional linear deployable boom stacer of spacecraft. 2023. doi:10.1016/j.mtcomm.2023.105444.

[38] Lin JK, Knoll CF, Willey CE. Shape memory rigidizable inflatable (ri) structures for large space systems applications. 2006. doi:10.2514/6.2006-1896.

[39] Lang RJ, Tolman KA, Crampton EB, Magleby SP, Howell LL. A review of thickness-accommodation techniques in origami-inspired engineering. 2018. doi:10.1115/1.4039314.

[40] Zirbel SA, Lang RJ, Thomson MW, Sigel DA, Walkemeyer PE, Trease BP, et al. Accommodating thickness in origami-based deployable arrays. Journal of Mechanical Design, Transactions of the ASME 2013;135. doi:10.1115/1.4025372.

[41] Miura K. Method of packing and deployment of large membranes in space. 1985.

[42] Landau E. Solar power, origami-style. 2014. URL: https://www.nasa.gov/jpl/news/origami-style-solar-power-20140814.

[43] Luo M, Zhu ZH, Xu Q, Wang Y, Luo W. Vibration suppression of large deployable space structures based on viscous damping. 2021.

[44] Pan Q, He T, Xiao D, Liu X. Design and damping analysis of a new eddy current damper for aerospace applications. Latin American Journal of Solids and Structures 2016;13:1997–2011. doi:10.1590/1679-78252272.

[45] Sodano HA, Bae JS. Eddy current damping in structures. 2004. doi:10.1177/0583102404048517.

[46] Ali-Akbari HR. Design-of-a-satellite-solar-panel-deployment-mechanism-using-the-brushed-dc-motor-as-rotational-speed-damper. 2018. URL: https://www.researchgate.net/publication/324068106.

[47] Ueura K, Slatter R. Development of the harmonic drive gear for space applications. 1999.

[48] Girard A, Roy N. Structural dynamics in industry. ISTE; 2008. ISBN 9781848210042.

[49] Rodrigues JD. Apontamentos de Vibrações Mecânicas. 2021.

[50] ESA . Space engineering Spacecraft mechanical loads analysis handbook. 2013.

[51] Reddy J. An Introduction to the Finite Element Method. 3 ed.; McGraw-Hill Education; 2005.

[52] Arianespace . Vega User's Manual Issue 04. 2014.

[53] NASA . Practice no. PD-ED-1211 - combination methods for deriving structural design loads considering vibro-acoustic, etc., responses. 2008.

[54] ESA-ESCET . Space engineering structural factors of safety for spaceflight hardware. 2019.

[55] Jayakumar S. Design and analysis of launch locks for juice sub-millimeter wave instrument. 2014.

[56] Mouritz AP. Introduction to Aerospace materials. Woodhead Publishing; 2012. ISBN 9781845695323.

[57] Agency ES. ECSS-E-HB-32-20 Structural materials handbook - Part 5: New advanced materials, advanced metallic materials, general design aspects and

load transfer and design of joints. ESA Requirements and Standards Division; 2011.

[58] Eswara N, Wanhill PRJH. Aerospace Materials and Material Technologies Volume 1: Aerospace materials. 2017. URL: http://www.springer.com/series/15453.

[59] DepartmentofDefenseUSA . Metallic Materials and Elements for Aerospace Vehicle Structures / MIL-HDBK-5J. Department of Defense - United States of America; 2003. ISBN 6094854004.

[60] Aalco . 6082 - T6-T651 plate. 2022. URL: https://www.aalco.co.uk/datasheets/Aluminium-Alloy_6082-T6~T651_148.ashx.

[61] Azom . Aluminium alloys - aluminium 6082 properties, fabrication and applications. 2023. URL: https://www.azom.com/article.aspx?ArticleID=2813.

[62] YiehAluminum . AA6062 - aluminum plate data sheet. 2022. URL: https://aluminum.yieh.com/en/aluminum-6000-series.

[63] RogersCorporation . RO4000 laminates RO4003C and RO4350B - data sheet. 2023. URL: https://www.rogerscorp.com/advanced-electronics-solutions/ro4000-series-laminates/ro4003c-laminates.

[64] Hutapea P, Grenestedt JL. Effect of temperature on elastic properties of woven-glass epoxy composites for printed circuit board applications. 2003.

[65] LaminatedPlastics . FR-4 technical data sheet. 2023.

[66] Madier D. Practical finite element analysis for mechanical engineers. First ed.; 2020. ISBN 9781999047504.

[67] ESA . Ecss-e-st-32-03c space engineering structural finite element models. 2008.

[68] Company S. Coefficient of friction reference chart. 2022. URL: https://www.schneider-company.com/coefficient-of-friction-reference-chart/s.